

Copyright
by
Nishamathi Kumaraswamy
2014

**The Thesis Committee for Nishamathi Kumaraswamy
Certifies that this is the approved version of the following thesis:**

Characterization of Biaxial Mechanical Properties of Rubber and Skin

**APPROVED BY
SUPERVISING COMMITTEE:**

Supervisor:

Mia K. Markey

Co-Supervisor:

Krishnaswamy Ravi-chandar

Characterization of Biaxial Mechanical Properties of Rubber and Skin

by

Nishamathi Kumaraswamy, B.E.

Thesis

Presented to the Faculty of the Graduate School of

The University of Texas at Austin

in Partial Fulfillment

of the Requirements

for the Degree of

Master of Science in Engineering

The University of Texas at Austin

May 2014

Dedication

To my husband Pradeep
and
children Ashok and Kalki

Acknowledgements

I would like to thank my advisor Dr. Mia Markey and co-advisor Dr. Krishnaswamy Ravi-Chandar for their continuous guidance and support throughout my thesis research and writing. It has indeed been an honor to have worked and discussed ideas with such experts in their respective fields.

I would like to express my gratitude and thanks to Dr. Markey for bringing me into this program and for teaching me how to be an independent researcher. I also thank Dr. Ravi-Chandar for teaching me biomechanics and opening up his lab and resources to me to make these studies possible, for sharing his invaluable knowledge of mechanics from which I have learned immensely.

I express my deep gratitude to everyone in the Biomedical Informatics Laboratory and the Center for Mechanics of Solids, Structures and Materials.

Finally, I would like to thank my husband and my two wonderful kids who have been very patient with me all the times I had to stay late or work on the weekends. I also want to express my thanks to my parents and sister for their love and encouragement, which they have given me unconditionally for 30 years.

Abstract

Characterization of Biaxial Mechanical Properties of Rubber and Skin

by

Nishamathi Kumaraswamy, MSE

The University of Texas at Austin, 2014

Supervisor: Mia K. Markey

Co-Supervisor: Krishnaswamy Ravi-chandar

Breast cancer is one of the most frequently diagnosed cancers affecting women in the United States. An ongoing objective of many research groups is to develop a biomechanical breast model for different applications, ranging from surgical outcome predictions for patients undergoing breast reconstruction surgery, to image registration for planning plastic surgery. Achieving the goal of developing a physics based biomechanical model of the human breast requires the determination of material properties of the various tissues constituting the breast. The objective of this thesis is to develop an appropriate hybrid experimental-numerical technique to enable the calibration of material parameters of skin for different constitutive models (commonly used for skin). The quantification of the material parameters thus obtained validates the bulge test method to be used in testing soft tissue specimens like skin.

A bulge test device was custom-built for this work; it consists of a pressure chamber, two digital cameras, and a syringe pump as its main components. The syringe pump provides a constant flow rate of water into the pressure chamber and results in the bulging of specimens with a diameter between 45 mm and 80 mm. Three-dimensional Digital Image

Correlation technique is used to obtain full field displacement measurements of the three dimensional shape of the bulge. Tests were performed on commercial rubber sheets of different thickness and on porcine skin specimens; in these tests, the bulge shape was measured at monotonically increasing and decreasing pressure levels, as well as during cyclic loading allowing determination of the deformation and strain fields over the specimen surface. In order to extract the material properties, a hybrid experimental-numerical method was used: the experiment was modeled numerically using the finite element analysis software Abaqus, imposing the commonly used Mooney-Rivlin model for isotropic materials and the Gasser-Ogden-Holzapfel model for anisotropic materials. A comparison between the experimentally measured and numerically simulated bulge shapes was used to determine the optimized material parameters under biaxial loading conditions over a large range of stretch levels.

Table of Contents

List of Tables	x
List of Figures	xi
Chapter 1: Introduction	1
1.1 Motivation.....	1
1.2 Introduction - Human Skin	1
1.3 Layers Of Skin	2
1.4 Skin Composition.....	3
1.5 Mechanical Characteristics of Skin	5
1.5.1 Normal Stress-Strain Response of Skin.....	5
1.5.2 Viscoelastic Response.....	7
1.5.3 Anisotropic Response	8
1.6 Constitutive Models	9
1.7 Objective	10
1.8 Thesis Outline	10
1.9 Thesis Chapter Summary	11
Chapter 2: Literature Review.....	13
2.1 Introduction.....	13
2.2 Material Properties Of Skin in Breast Biomechanical Models.....	16
2.3. Skin Mechanics Literature	18
2.3.1. Uniaxial Testing System	20
2.3.2 Planar Biaxial Testing Systems	23
2.3.3 Other Experimental Techniques	28
2.3.4. Multiaxial Testing Systems.....	30
2.3.5. Inflation /Blister/Bulge Testing	31
2.4. Discussion.....	36
Chapter 3: Testing Methods, Experimental Set-Up and Results	37
3.1 Introduction – Bulge Test	37

3.2	Bulge Test Device design	38
3.3	Bulge Test Experiment	41
	3.3.1 Removing the air bubble from the system	42
	3.3.2 Experiment Precautions	42
	3.3.3 Experiment Protocols.....	43
3.4	Digital Image Correlation - Introduction	44
	3.4.1 Basic Principle of 3D DIC	45
	3.4.2 Camera Calibration and DIC Technique.....	46
3.5	Experimental Results	48
	3.5.1 Rubber sheet specimens.....	49
	3.5.1 Porcine skin specimen.....	56
	3.5.1.1 Viscoelastic response:	61
3.6	Finite Elasticity	63
	3.6.1 Kinematics	64
	3.6.2 Stress equilibrium	66
	3.6.3 Boundary conditions	67
	3.6.4 Constitutive equations.....	68
3.7	Simulations in ABAQUS.....	69
3.8	Numerical Results.....	71
	3.8.1 Rubber specimen.....	72
	3.8.2 Porcine skin.....	75
Chapter 4: Conclusions and future work		85
	4.1 Conclusions.....	85
	4.2 Limitations and Future work.....	87
Appendix A.....		90
Appendix B.....		95
References.....		99

List of Tables

Table 3-1: Parameter settings for ARAMIS™ displacement-strain calculations..	48
Table 3-2: Maximum displacement and strains recorded in experiments on rubber sheets.....	54
Table 3-3: Material description and it's response to load.....	68
Table 3-4: Material parameters: 2D GOH model [Reproduced from Tonge et al., 2013]	78
Table 3-5: Material parameters used for the simulations.....	80
Table B-1: Software used in current work and its purpose.....	95
Table B-2: Hardware used in current work and picture of the hardware.....	96

List of Figures

Figure 1-1: Schematic of different layers of skin. Reproduced from http://www.dermnet.org.nz/doctors/principles/dermis.html	4
Figure 1-2: Schematic of skin behavior under uniaxial and biaxial tension. [Reproduced from Xu, 2013].....	6
Figure 1-3: Phases in typical stress-strain relationship for skin	7
Figure 1-4: Typical stress-strain curve for skin showing hysteresis [Reproduced from Fung, 1984].....	8
Figure 1-5. Anisotropic response in two orthonormal directions (length and width of the body) observed in skin. [Reproduced from Lanir and Fung, 1974 Part ii].....	9
Figure 1-6: Thesis schematic flowchart.....	12
Figure 2-1: Langer Lines from torso of a human cadaver. [Reproduced from Ridge and Wright, 1966].....	13
Figure 2-2: Isotropic eight-chain network of freely jointed chain model [Reproduced from Arruda and Boyce, 1993]	22
Figure 2-3: In-vitro uniaxial test data for normal and Hypertrophic scar (HTS) skin from Dunn et al. (1985) best fitted using an Isotropic eight-chain network of freely jointed chain model [Reproduced from Bischoff et al., 2000]	23
Figure 2-4: Optomechanical Biaxial Testing Device Set-up [Reproduced from Lanir and Fung, Parts i and ii, 1974].....	24
Figure 2-5: Schematic of optomechanical system. [Reproduced from Lanir and Fung Parts i and ii, 1974].....	25

Figure 2-6: Vito's Biaxial Test Device set-up [Reproduced from Vito, 1980]	27
Figure 2-7: Nielsen's modified Biaxial set up from that of Lanir's set-up [Reproduced from Nielsen et al., 1991].....	28
Figure 2-8: Schematic representation of the suction device attached to imaging system (ultrasound). [Reproduced from Hendriks et al., 2003].....	29
Figure 2-9: <i>In-vivo</i> Multi axial Testing set up. [Reproduced from Kvistedal and Nielsen, 2009].....	31
Figure 2-10: Bulge Test schematic	32
Figure 2-11: Pressure-controlled inflation system [Reproduced from Tonge et al., 2012]	34
Figure 3-1: Schematic of Bulge/Inflation test set up of a thin film [Reproduced from Bosseboeuf et al., 1997].....	38
Figure 3-2: Sectional front view of the chamber showing the curvature on the top plate.....	39
Figure 3-3: Picture showing the various components in the bulge test set-up.....	40
Figure 3-4: Schematic of 3D DIC technique. [Reproduced from Pan et al., 2009].....	46
Figure 3-5: Overlay of the full-field u_z displacement with that of the rubber sheet specimen, when $P = 13$ kPa.	50
Figure 3-6: Pressure vs Apex displacement for rubber sheet - 3.0 mm thick (Experimental data).....	51
Figure 3-7: Displacement contour plots for pressures corresponding to points 1, 2, 3, and 4 from Figure 3-6	51
Figure 3-8: Bulge profile for pressures corresponding to points 1, 2, 3, and 4 from Figure 3-6	52

Figure 3-9: Major strain contour plots for pressures corresponding to points 1, 2, 3, and 4 from Figure 3-6	52
Figure 3-10: Minor strain contour plots for pressures corresponding to points 1, 2, 3, and 4 from Figure 3-6	53
Figure 3-11: Apex Major and Minor strain Vs Strain stage (Time) plots for rubber (3.0 mm thick)	53
Figure 3-12: Pressure vs. Apex displacement for all 3 rubber sheet specimens (Experimental data).....	55
Figure 3-13: Bulge profile for different thickness rubber sheet specimens at a pressure of 2.6 kPa.	55
Figure 3-14: Bulge profile for different thickness rubber sheet specimens at the maximum pressure of 13.0 kPa.....	56
Figure 3-15: Overlay of the full-field u_z displacement with that of the actual porcine skin specimen, when $P = 13$ kPa.....	57
Figure 3-16: Pressure vs. Apex displacement for porcine skin (Experimental data).....	58
Figure 3-17: Displacement contour plots for pressures corresponding to points 1, 2, 3, and 4 from Figure 3-16	59
Figure 3-18: Bulge profile for pressures corresponding to points 1, 2, 3, and 4 from Figure 3-16	59
Figure 3-19: Major strain contour plots for pressures corresponding to points 1, 2, 3, and 4 from Figure 3-16	60
Figure 3-20: Minor strain contour plots for pressures corresponding to points 1, 2, 3, and 4 from Figure 3-16	60
Figure 3-21: Apex Major and Minor strain vs. Strain stage (Time) plots	

for porcine skin	61
Figure 3-22: a) Pressure profile for cyclic loading and unloading for 5 cycles to study viscoelastic response.	
b) Apex displacement profile for cyclic loading and unloading for 5 cycles to study viscoelastic response.	62
Figure 3-23: Pressure vs. Apex point displacement for cyclic loading and unloading of 5 cycles to study viscoelastic response.....	62
Figure 3-24: Motion of a particle P and line segment from the reference configuration to the deformed configuration.	65
Figure 3-25: Meshed geometry with an eight node linear brick element	70
Figure 3-26: Load and boundary conditions applied on the geometry	71
Figure 3-27: Pressure vs. Apex displacement for rubber – 3.0 mm thick (Simulated data).....	72
Figure 3-28: Simulated displacement contour plots for pressures corresponding to points 1, 2, 3, and 4 from Figure 3-27	73
Figure 3-29: Imagesc plot of difference in displacement measures between experimental and simulated points in rubber - 3.0 mm thick	73
Figure 3-30: Comparison of displacements from experiment and simulations for a section through the center at a maximum pressure of 13 kPa in rubber - 3.0 mm thick	74
Figure 3-31: Experiment and simulated displacement comparison through a center section for values of Pressure = 3.25 kPa, Pressure = 6.50 kPa and Pressure = 13.0 kPa	75
Figure 3-32: Pressure Vs Apex displacement porcine skin using 2D GOH model with C_{01} (Simulated data)	80

Figure 3-33: Displacement contours using 2D GOH model with C_{01} for points marked in Figure 3-32.....	81
Figure 3-34: Displacement profile using 2D GOH model with C_{01} for points marked in Figure 3-32.....	81
Figure 3-35: Major strain contour plots using 2D GOH model with C_{01} for points marked in Figure 3-32.....	82
Figure 3-36: Minor strain contour plots using 2D GOH model with C_{01} for points marked in Figure 3-32.....	82
Figure 3-37: Major strain profile at 13 kPa using 2D GOH model with C_{01} for a section taken at the center of the specimen (Simulated data)	83
Figure 3-38: Minor strain profile at 13 kPa using 2D GOH model with C_{01} for a section taken at the center of the specimen (Simulation data)	83
Figure 3-39: Comparison of experimental and simulated displacements for all points at pressure values marked in Figure 3-16	84
Figure 3-40: Apex displacements Vs Pressure plots for experiment and simulation results on porcine skin.....	84
Figure 4-1: Biaxial Bulge Test set-up.....	86

Chapter 1: Introduction

1.1 MOTIVATION

Skin is the largest organ of the human body whose main function is to protect the body against external influences. The mechanical behavior of skin is considered to be important in many applications such as in plastic surgery, cosmetic surgery, and for other treatment or understanding of skin based diseases. Many experiments have been performed on skin (porcine, human, rabbit etc.,) to understand the complex mechanical behavior of skin. Many numerical models have also been proposed to describe the mechanical response of skin. However, no standard constitutive model is available yet for skin in the literature. Most of the experiments that have been reported either do not cover the large stretch range that skin can undergo which limits their use or the model developed is based on the experimental results of skin from animals or the model developed is solely based on just the dermal fiber layers ignoring the contributions of epidermis and hypodermis. In order to develop a general constitutive model and parameters that can predict the skin response as a whole organ, an experimental-numerical approach is developed in this thesis work.

1.2 INTRODUCTION - HUMAN SKIN

Skin is a multilayered organized membrane and makes up approximately 14% to 16% of a human adult's body weight. It plays an important role in thermo-regulation, wound healing, sensory, and protective functions [Goodwin, 2011]. The skin is polymeric in nature and is considered a complex material to model. This thesis focuses mainly on the mechanical behavior of skin as opposed to its physiological aspects.

The mechanical demands of the skin vary in different parts of the human body. Based on these demands the mechanical behavior and thickness of skin also vary with different parts of the body. For example, eyelids, whose main function is to blink (folding and unfolding), have a thickness of only 0.5 mm. In contrast the skin on the sole of feet, which undergoes a lot of abrasions, is at least 4 mm thick. Furthermore, the *in vivo* mechanical behavior of skin tissue is described as heterogeneous, anisotropic, non-linear, and visco-elastic because of its non-homogeneous structure and composition. It is affected by many other factors as well such as age, gender, hydration, etc.

1.3 LAYERS OF SKIN

There are generally 3 kinds of skin defined in an adult human body.

- a) Glabrous skin - hairless areas such as palms of the hands and soles of the feet
- b) Hairy skin - skin where hair follicles are present
- c) Mucocutaneous skin - skin areas that border entrances to the interior of the body

All three types of skin are composed of three main layers: epidermis, dermis, and subcutaneous (hypodermis) tissue. The overall mechanical behavior of skin is thus a combination of the behavior of these three different layers. Therefore, a thorough knowledge of the three layers that compose skin is important to comprehend the mechanical behavior of skin over all. To date, research on skin mechanics has focused mainly on full-thickness skin. However, there are some studies where the focus is to understand the mechanics of individual layers of skin such as the viable epidermis, stratum corneum, etc., [Rigal and Lévêque, 1985; Geerligs, 2010]. The purpose of these studies is to provide a better understanding of the way a treatment or disease affects the skin behavior, where the different layers of skin and their individual mechanical properties play an important role. The goal of the current work is to find material

parameters to characterize normal skin that can be used in a Breast Biomechanical Model (BBM). Thus, finding the mechanical properties of full-thickness skin would suffice. The following chapters focus mainly on skin and its mechanics as a full thickness organ consisting of all three layers for this purpose. The structure of skin is described in the next section briefly for completeness.

1.4 SKIN COMPOSITION

A schematic representation of the three different layers of skin is shown in Figure 1-1. Each layer of skin is further classified into different layers in itself; however, keeping our goal in mind, it suffices to have a good understanding of the skin as a structure in itself. For more details on each layer, readers are referred to the books and articles in the literature [see, for example, Cox, 1941; Elden, 1971; Agache et al., 1980; Rigal and Lévêque, 1985; Goodwin, 2011].

Epidermis is the superficial layer of skin and is approximately 0.07 - 0.12 mm [Satin, 2009] thick depending on the location on the human body. The main function of the epidermis is to act as a protective layer against any kind of external injury. It also has a high cellular turnover as it acts as the primary line of defense for the human body. These outward moving cells are called keratinocytes and they migrate to the outer skin surface and are dead, thus forming the stratum corneum. Beneath the layer of dead cells is the viable epidermis. This layer of epidermis is known as a very highly immune reactive structure and hence has been the target for vaccinations.

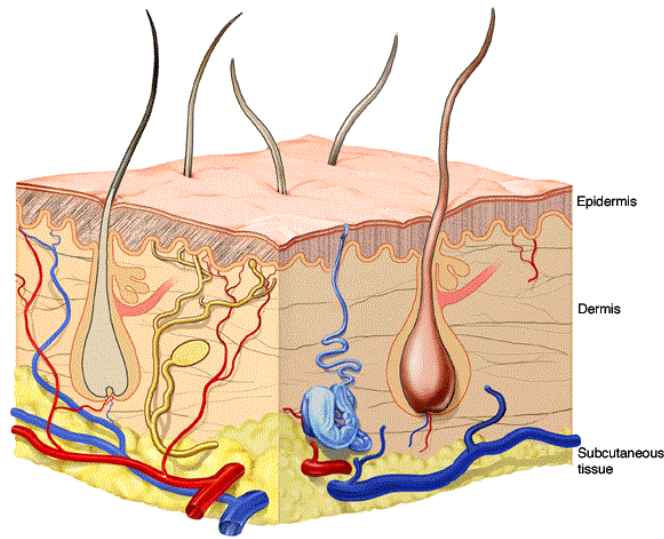


Figure 1-1: Schematic of different layers of skin. Reproduced from <http://www.dermnet.org.nz/doctors/principles/dermis.html>

Dermis is the second layer that is sandwiched between the (outer) epidermis and (inner) subcutaneous layer of skin. This layer is about 1-4 mm thick [Satin, 2009] and makes up the bulk of human skin. Dermis can be further classified into 2 layers with each layer containing elastin and collagen fibers in a matrix. The fiber direction is related to the Langer lines in the body and thus determines the behavior of skin in that part of the body. High levels of deformation due to stretch are thus allowed due to this network of elastin and collagen fibers. The contribution of the fiber and matrix to the mechanical properties of skin is discussed in detail in Section 1.5. This layer of skin also hosts other important thermoregulatory organs or structures such as hair follicles, sweat gland, receptors and a microcirculatory bed of arterioles, arterial and vein capillaries and venules [Xu and Lu, 2011].

Hypodermis is the third layer and is composed of loose fatty connective tissues (adipose). This layer found below the dermis is not part of skin, but is considered more as

a deep extension of the dermis [Xu and Lu, 2011]. Its thickness varies with anatomical site, age, gender, race, and health of the individual. The adipose tissue stores fat and serves as a potential source of energy. The mechanical functions of this layer include providing cushioning for bony prominences and attenuate or disperse the externally applied pressure [Shoham, 2012].

1.5 MECHANICAL CHARACTERISTICS OF SKIN

Skin, as mentioned in Section 1.1, is complex material covering the entire surface of human body. To enable the different changes that the body undergoes during the process of growth, it is flexible, compliant and facilitates large deformations in any direction. As mentioned in Section 1.3, we will consider full thickness skin in this thesis. Henceforth in this thesis, the term “skin” will be used to represent all layers thereof; namely, epidermis, dermis, and hypodermis and its mechanical behavior is considered to be anisotropic, viscoelastic, and non-linear. These characteristics of its mechanical behavior allow skin to undergo large deformations in accordance to the demands of its functional role.

1.5.1 Normal Stress-Strain Response of Skin

As described in Section 1.4, the dermis contains of a dense irregular network of collagen and elastic fibers in a matrix allowing large deformations of skin. Early mechanical studies [Craik and McNeil, 1965; Daly, 1966; Brown, 1972] on human skin from the abdominal region using Scanning Electron Microscopy (SEM) have shown that skin is anisotropic. The suggested anisotropy is due to the fiber orientation in a preferential direction in the dermal layer. The sandwiched layer dermis thus contributes or dominates the overall mechanical properties of skin [Xu, 2011].

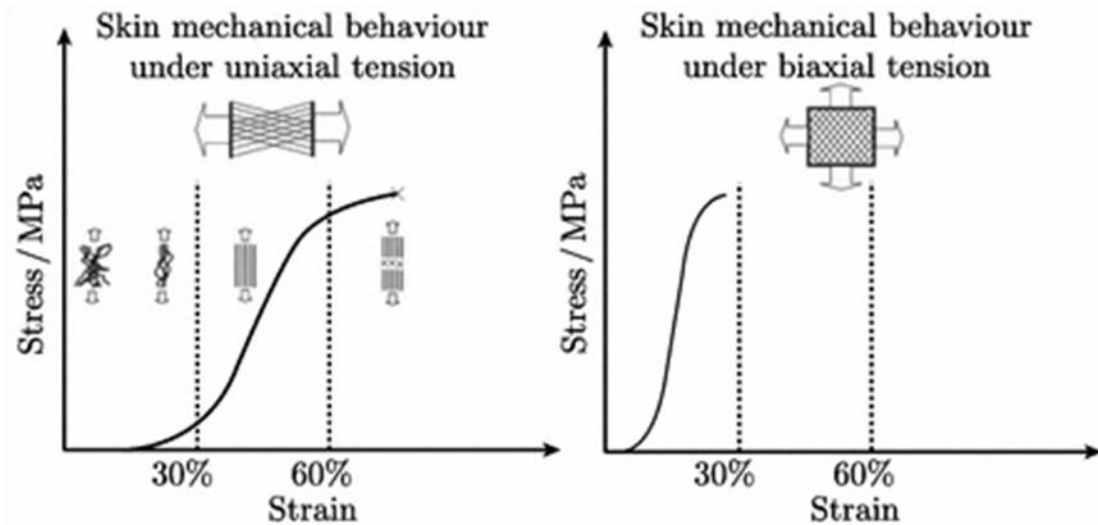


Figure 1-2: Schematic of skin behavior under uniaxial and biaxial tension. [Reproduced from Xu, 2013]

The typical stress-strain curve of skin under uniaxial and a biaxial tension loading is shown in Figure 1-2 [Xu, 2013]. Both tests give a typical J shaped non-linear curve for skin. This curve can be typically classified into 3 phases as shown in Figure 1-3. Phase I is extension at low strain values; this is the initial low-stiffness toe region where energy and shape recovery is important. In this phase, it is generally accepted that elastin fibers and the matrix mainly provide resistance to deformation [Oxlund, 1988]. Typically, the stiffness in this region is difficult to measure due to resolution limits in the measuring system.

By the end of Phase I, the collagen fibers that are initially randomly oriented (and in some cases kinked or crimped) begin to elongate and line up in the direction of applied load. Phase II results due to the alignment and/or uncrimping of the collagen fiber network. Since the collagen fibers are stiffer, the straightened collagen fibers resist the applied load, making the skin stiffer in this phase. Phase III results when the fibers come

under directly applied external load exhibiting high stress and eventually, the fibers begin to break thus reaching the ultimate tensile strength. Thus, the initial compliance property of skin is due to elastin fibers, the increasing stiffness at higher strain levels is due to the collagen fiber network, and eventual limit in stress due to breaking of the fibers.

1.5.2 Viscoelastic Response

In addition to the nonlinear behavior indicated above, skin also exhibits time-dependent mechanical behavior. The elastic behavior is important in shape recovery after deformation (Phase 1 in Figure 1-3) while the viscous behavior is responsible for energy dissipation by means of sliding of the collagen fibers (Phase 2 in Figure 1-3) during alignment as the load is applied. This leads to the hysteresis in the stress-strain curve. A typical hysteresis curve for soft tissue is shown in Figure 1-4.

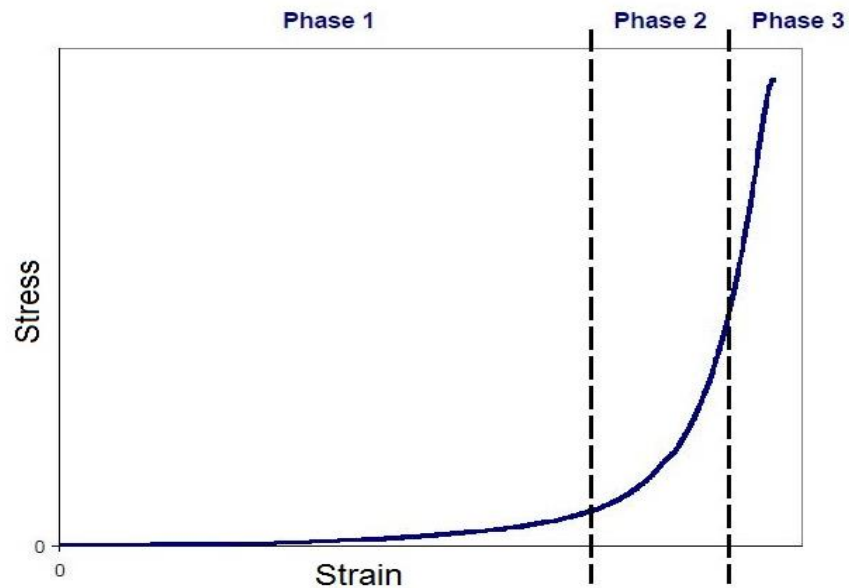


Figure 1-3: Phases in typical stress-strain relationship for skin

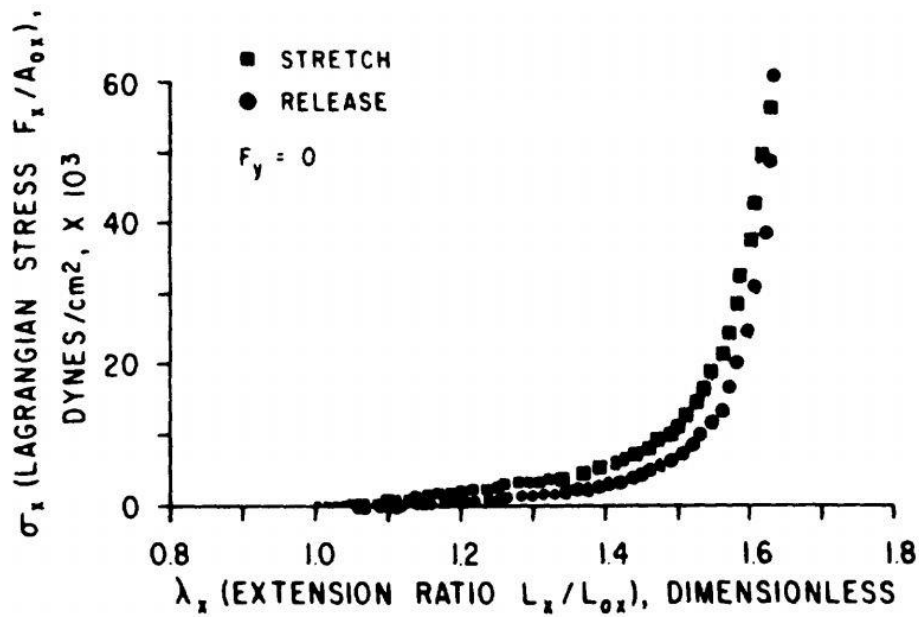


Figure 1-4: Typical stress-strain curve for skin showing hysteresis [Reproduced from Fung, 1984].

1.5.3 Anisotropic Response

Soft tissues such as skin are known to contain a matrix of fibers, allowing for its large deformations and anisotropic properties [Craik and McNeil, 1965; Daly, 1966; Brown, 1972]. The fiber matrix network, fiber orientation, and fiber strength varies with the function they perform as part of the biological tissue. There seems to be a strong correlation between fiber orientation and its functions requirements in a tissue. For example if a tissue is loaded *in vivo* in one direction only, the fibers will orient in that particular direction resulting in anisotropic mechanical properties of the tissue. Many investigators have shown skin to be anisotropic by comparing results of tests performed in two normal directions (parallel and perpendicular to the fibers). Figure 1-5 shows one such test result performed by Lanir and Fung in 1974 to prove the existence of anisotropy

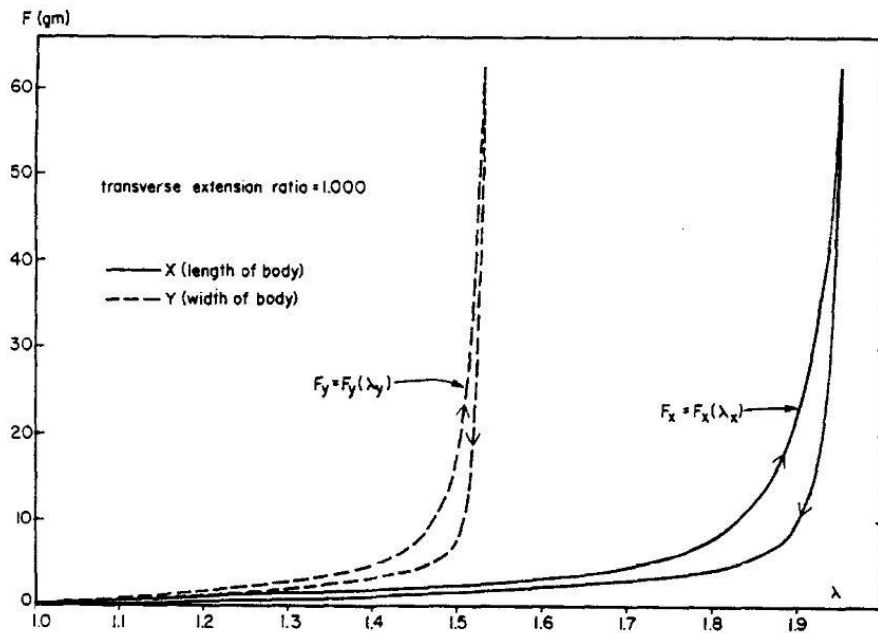


Figure 1-5. Anisotropic response in two orthonormal directions (length and width of the body) observed in skin. [Reproduced from Lanir and Fung, 1974 Part ii]

in skin (rabbit) tissue. The two curves are obtained due to the preferential orientation of the fibers in the tissue.

1.6 CONSTITUTIVE MODELS

There are two main approaches that are commonly used to model the mechanical response of skin:

- a. Phenomenological approach – In this approach a mathematical model is used to fit the experimental data. As a result, we have a mathematical model with suitable parameters that reflect the behavior of the material (skin).
- b. Micromechanical approach – In this approach, the constitutive relations are derived based on a description of the geometry and properties of the constituents

composing the material and a homogenization of the deformation of the representative micro geometry.

The functional form varies for different models and is driven mainly by the underlying assumptions used in the model such as the degree of anisotropy, viscoelasticity etc. In this thesis, a phenomenological approach will be taken, fitting experimentally measured response to different material models.

1.7 OBJECTIVE

The objective of this thesis is to develop an appropriate portable experimental technique and procedure to enable the characterization of mechanical behavior of skin, and to provide a calibration of experimental data to a phenomenological model for use in the investigation of any biomechanical application based models, such as in simulating the motion of breast under gravitational force or simulating the load causing pressure ulcers, etc. Breast skin in existing BBMs is mostly characterized using parameters fitted from simple uniaxial experiments or from experiments performed on animal skin. However, these models or model parameters available in literature do not give consistent results in predicting skin behavior and subsequently the results of the simulations are also far from observations. The outcome of this thesis will enable the mechanical characterization of human skin in a biaxial state.

1.8 THESIS OUTLINE

The flow diagram summarizes the thesis objectives and methods used to reach our aims in a pictorial form. There are 2 main components in the flow diagram.

- a. Experimental set-up and
- b. Computational model

In words, the experimental set-up involves building a design for a bulge test device, and measuring the displacements using a 3D image correlation technique. The computational model involves the optimization routine, to arrive at the optimized material parameters for skin, using a phenomenological model such as Mooney-Rivlin etc. Figure 1-6 is a pictorial representation or work flow of the thesis work done here.

1.9 THESIS CHAPTER SUMMARY

In order to achieve the thesis goals, an experimental set-up has been designed and fabricated. We have tested rubber and porcine skin specimens using this test device. Chapter 2 summarizes the previous studies on skin and the importance of the availability of a reliable constitutive model for skin in breast biomechanics literature. Chapter 3 summarizes the materials needed to design the biaxial bulge test device. This chapter details the experimental set-up and the sample preparation protocols required before testing followed by experimental results. It also discusses the simulation parameters used to create the numerical model followed by the numerical results. Chapter 4 discusses the limitations of this thesis and future work goals.

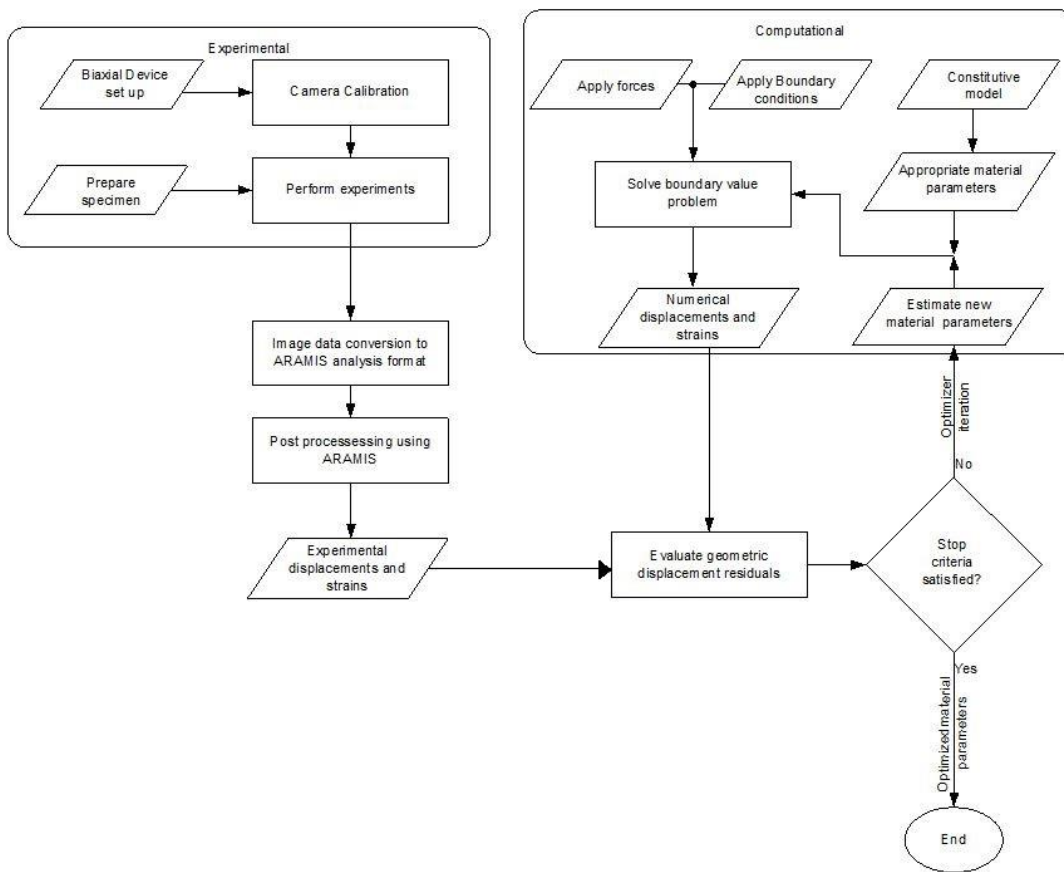


Figure 1-6: Thesis schematic flowchart

Chapter 2: Literature Review

2.1 INTRODUCTION

In 1834, Dupuytren [Dupuytren, 1834] observed that a puncture in cadaver skin tissue did not create a round cut but instead formed an elliptical hole. This was one of the earliest studies that provided the motivation to understand this behavior of skin. Almost 30 years after this finding, Langer conducted his experiments that led to the observation of “cleavage” lines; these cleavage lines are now commonly known as *Langer lines*.

Langer [Langer, 1861] conducted a repeated set of puncture experiments on human cadaver skin on different parts of the body. He noted that the resulting wounds assumed an elliptical configuration and hence he joined the major axes of these ellipses to

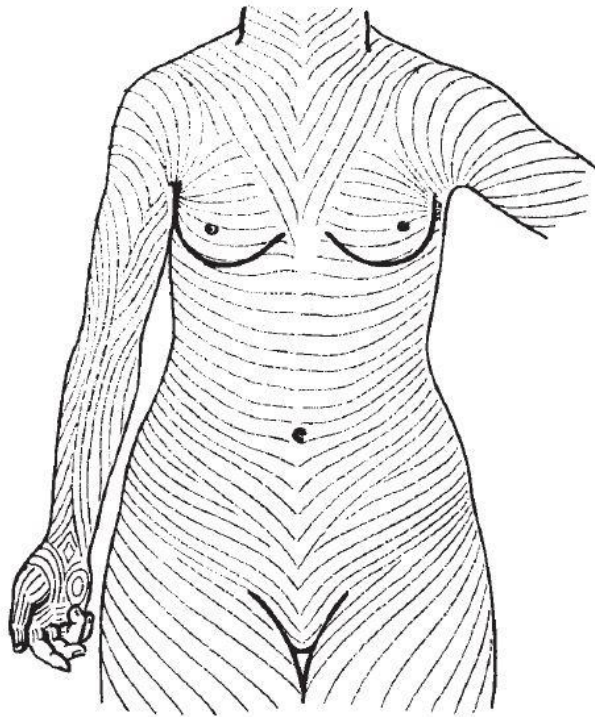


Figure 2-1: Langer Lines from torso of a human cadaver. [Reproduced from Ridge and Wright, 1966]

produce a series of lines; these are now called Langer Lines. Figure 2-1 shows Langer Lines on the whole torso. Following Langer, Cox [Cox, 1941] used histological methods to show that these Langer lines were formed due to the preferred orientation of fibers in the skin tissue. He showed, by means of a quantitative analysis of scanning electron microscopy (SEM) images, that the fiber network in the skin from any body part was multidirectional. However, he observed that the fibers had an overall preferential orientation which is usually in the direction of maximum tension, characterized by the Langer lines. It was thus concluded that the sample's response to externally applied load will depend on the direction of the load application with respect to the orientation of the Langer Lines. Langer Lines are well recognized by surgeons, who intentionally make incisions along the direction of Langer lines in order to allow wound healing with minimum scarring. The major conclusion reached from these early experiments is that the skin (connective tissue) is always under a state of pre-tension caused by the arrangement of the fibers in the tissue. Another conclusion is that skin response is dominated by the fiber orientations in the different body parts.

Studying the mechanical properties of skin is important for many modern applications, such as understanding the mechanics of stabbing [Annaidh et al., 2010], planning plastic surgery, dermatology, impact biomechanics [Annaidh et al., 2012], and designing devices that interact with the skin, such as shaving blades [Evans, 2009]. However, there is a lack of accurate mechanical property data in the literature for soft biological tissues in general, and skin in particular. Recently, there has been more focus on this issue to facilitate the modeling of skin in various biomechanical applications [Annaidh et al., 2012].

Many investigators have used *in vitro* [Tonge et al., 2012] and *in vivo* [Kvistedal and Nielsen, 2009] studies to understand the mechanical behavior of skin under large deformations. However, we are not aware of any studies in the skin mechanics literature that characterize the mechanical properties of human breast skin. Rather, breast biomechanical models [Azar et al., 2000; Pathmanathan et al., 2004] typically use material properties of rabbit skin, cat skin, or human cadaver (back) skin. However, skin properties obtained from cadavers, especially from other parts of the human body, or from animals are not representative of the exact mechanical behavior of human breast skin [Tonge et al., 2012]. It is well known that it is better to extract mechanical properties from tests performed on skin within 24 hours of harvesting rather than tests on cadaver skin. Skin mechanical properties are known to change from their *in vivo* to *in vitro* configuration. It is also known from the literature that skin mechanical properties depend on age, race, and the body site from which they are harvested [Agache et al., 1980].

The accuracy of the experimental data and the constitutive model used to parameterize breast tissues in a breast computational model greatly influence the breast model simulation results. On studying the different Breast Biomechanical Models (BBMs) available in literature, it is observed that the major variability in solving the boundary value problem comes from the

1. Prescribed boundary conditions (application dependent) and
2. Material properties of the breast tissues used in the BBMs.

These two entities contribute to the different results of BBMs, even those designed for the same medical application such as simulating breast mammographic compression. In this study, we seek to address the lack of knowledge of the material properties of breast skin.

For example, during movement from upright to supine position, the skin is witnessed experimentally to deform significantly due to the change in gravity loading. This deformation has been quantified experimentally [Khatam et al., 2013] by placing skin markers and tracking them during the change in orientation of the subject using the 3dMD torso system (3Q Technologies Inc., Atlanta, GA). Numerical simulations of such movements need to account for both the appropriate mechanical properties of skin and the displacement boundary conditions used so as to provide realistic simulation results.

In this thesis, we address an important source of error in BBMs, which is the lack of appropriate material parameters of breast skin. To that front, we designed a testing device to test skin in a biaxial state. The working of the biaxial bulge test device is calibrated by conducting tests on rubber sheets and porcine skin and can now be used with human skin specimens as well.

2.2 MATERIAL PROPERTIES OF SKIN IN BREAST BIOMECHANICAL MODELS

We briefly review the breast biomechanics literature focusing on the skin material parameters used in the different models for simulating the breast in applications such as magnetic resonance compression, image registration from different imaging modalities, model surgical applications, etc.

Azar et al., [2000] developed BBMs both with and without skin to simulate Magnetic Resonance (MR) compression. In their final breast compression model, skin was not modeled because a sensitivity analysis had shown that it had minimal effect on the accuracy of the simulations. They justified their assumption by stating that the skin's stiffness is mainly responsible for counteracting gravity effects and played a small role in responding to MR compression. In their sensitivity study, the mechanical properties of

skin were modeled by assuming a piece-wise linear function throughout stress-strain regime using small deformation theory. The experimental stress-strain curve for skin was obtained from [Elden, 1971].

Pathmanathan et al., [2004] developed a BBM to simulate the shape changes resulting from a shift from a prone to a supine configuration. The strain energy density function for the skin, assumed to be a homogeneous, isotropic, incompressible material, was described by an exponential model:

$$\mathbf{W} = \mathbf{a}(e^{b(I_1-3)} - \mathbf{1}) + \mathbf{c}(I_2 - 3) - \frac{p}{2}(I_3 - 1) \quad (2-1)$$

where I_i are the fundamental invariants of the left Cauchy-Green tensor and p is Lagrangian multiplier enforcing the incompressibility constraint. The parameters a, b, c for the skin model were obtained from experimental results of a uniaxial test on cat skin [Veronda and Westmann, 1970]. In a sensitivity analysis, they could not confirm conclusively the sensitivity of the model to the skin material model and parameters used.

Tanner [Tanner, 2005] modeled skin as being 10 times stiffer than adipose tissue in her BBM using linear and piece-wise linear approximations for skin. Including the skin in her BBM improved maximum displacement errors by 0.25 mm on average for one volunteer dataset. However, the effect of skin in her BBM could not be conclusively confirmed as the second volunteer dataset did not show any improvement in displacement error.

Carter [Carter, 2009] evaluated the effect of including skin in his BBM. He used a density of 1000 kg/m³ and modeled skin as an incompressible neo-Hookean material with the unknown parameter α_s as given below:

$$\mathbf{W} = \alpha_s(I_1 - 3) \quad (2-2)$$

Carter used a range of values for α_s in his BBM and studied the effect of including skin. The search for a suitable value for the parameters was based on the quantitative measure of minimum error in displacement for different combinations of parameter values for skin (α_s), fibro-glandular (α_g), and adipose tissue (α_a). His exhaustive search was confined to values nearest to 0.05 kPa for fibro-glandular and adipose tissue and nearest to 2 kPa for skin. No specific justification for searching in the range of 2 kPa for skin is provided in his work.

2.3. SKIN MECHANICS LITERATURE

In the skin mechanics literature, the two main types of testing that are usually performed to quantify the material properties of skin can be classified as *in vivo* and *in vitro*. Typical experimental techniques that fall into these two categories include uniaxial, planar biaxial and multiaxial, tension, indentation, blister, suction, and torsion tests. In this thesis, experimental techniques and procedures for uniaxial tension, planar biaxial, multiaxial, and blister tests from literature are discussed in detail. These are the main methods that are closely related to the experimental technique used in this thesis, and hence a thorough summary is provided. A shorter summary is provided on all the other types (includes suction, torsion, *in vivo* tension, and indentation tests) of experimental techniques that have been reported in the literature. A typical stress-strain curve for a biological specimen is shown in Figure 1-3 to provide context for the discussion on the test methods.

In vivo Testing – This is a class of test methods where the skin is tested in its native environment within the human body. In this testing procedure, natural conditions such as pre-strain experienced in the human body are maintained unaltered prior to the performance of the test. However, the effect of the surrounding tissues like subcutaneous

muscle that underlie the skin tissue and the fascia that separate the skin and muscle layers on the response of the skin itself cannot be separated without an inverse modeling approach.

In vitro Testing – This is a class of test methods where skin is harvested from the human body and tested outside its native environment. Although this does not allow replication of complete *in vivo* conditions, the test results can be interpreted with elementary analysis procedures. Furthermore, such tests also allow the tissue to be subjected to extreme conditions such as those of fracture conditions which cannot usually be performed *in vivo*.

The standard experimental techniques for both *in vivo* and *in vitro* mechanical characterization of skin are uniaxial and biaxial state of testing. Some *in vivo* studies in skin literature are performed using multiaxial testing as well. In a uniaxial state of testing, the load is applied in one direction (typically, parallel or perpendicular to fiber orientation in the specimen). In a biaxial state of testing, loading is applied in two distinct directions. In multiaxial testing force and displacements are applied along more than one axis or direction.

According to the skin literature, most attempts to determine the mechanical properties of anisotropic biological tissues like skin are done by means of uniaxial testing. Very few attempts have been made to characterize skin by means of biaxial [Lanir and Fung, Parts i and ii, 1974] or multiaxial [Kvistedal and Nielsen, 2009; Jor et al., 2011] testing. It has often been recognized that limiting the evaluation of a planar soft tissue like skin to uniaxial tests can lead to misrepresentation of its behavior. Therefore, use of a more realistic loading during the test such as the biaxial or multiaxial loading

conditions that better represents the *in vivo* behavior is preferred. However, a multiaxial testing rig is considered more cumbersome and unrealistic.

Skin, being a planar tissue, can be completely characterized by biaxial loading alone, and by assuming incompressibility to determine the strains in the thickness direction. Thus, recently biaxial testing has become increasingly common [Nielsen et al., 1991; Billiar and Sacks, 2000; Kim et al., 2011] to characterize skin. Some of the early biaxial tests were done *in vivo* and *in vitro* by means of planar tensile, indentation, torsion, suction, or blister test devices.

2.3.1. Uniaxial Testing System

In uniaxial testing, the skin specimen of length l and cross-sectional dimensions $d \times b$ is pulled along the length l and the corresponding stress-strain (force-elongation) relationship is obtained. Uniaxial tensile tests are relatively easy to perform and cost-effective. The majority of the experiments done to investigate skin material properties are done by means of such uniaxial tests. Although uniaxial tensile tests do not provide sufficient information for a full characterization of the in-plane mechanical properties, it provides a means for direct comparison between specimens, body sites, and the influence of environmental conditions for the various treatments [Geerligs, 2010]. Several early uniaxial studies were performed by applying tensile loads by means of hanging weights on the specimens. However, it was soon realized that these tests were not well controlled experimentally and subsequent uniaxial tests were done by using simple tensile test machines [Wilkes et al., 1973].

One of the early uniaxial tests on human skin was performed by Dunn et al. in 1985. Normal and hypertrophic scar (HTS) samples from human cadavers, 20 mm long and 10 mm wide were tested uniaxially at room temperature in Phosphate Buffered

Saline (PBS) solution in an Instron model 1122 testing machine [Dunn and Silver, 1983; Dunn et al., 1985]. They reported the results of stress-strain curves for both normal and HTS skin. Several specimens in different orientations were tested to report the stress-strain experimental data. However, no specific constitutive model was fitted to the experimental results obtained.

Bischoff et al. [Bischoff et al., 2000] simulated the experiment of Dunn and Silver using Finite Element Modeling. They used a statistical mechanics based constitutive model for a biologic material like skin. Here, a material is represented as a structure/network of random flexible long molecular chains which can rotate and stretch to accommodate deformation. Any deformation of this assembled structure/network creates change in entropy of the chain network producing stress. The two main components of such statistical models are: the mathematical description of the chains and the manner in which the chains assemble to form the network.

An isotropic eight-chain network of freely jointed chain model developed by Arruda and Boyce was used by Bischoff et al. to model skin behavior. In this model, the eight statistical chains originate from the center of the cube and extend to each corner as shown in Figure 2-2. The freely jointed chains are flexible, unconstrained rotating chains with N rigid segments of length l . The true stress-stretch relation for the eight-chain model is given by

$$\sigma_1 - \sigma_2 = \frac{nk\Theta}{3} \sqrt{N} \mathcal{L}^{-1} \left[\frac{\lambda_c}{\sqrt{N}} \right] \frac{(\lambda_1^2 - \lambda_2^2)}{\lambda_c} \quad (2-3)$$

where σ_i is a principal stress $k = 1.3087 \times 10^{-23} \text{ Nm/K}$ is Boltzmann's constant, $\Theta = 298 \text{ K}$ is absolute temperature, \mathcal{L}^{-1} is the inverse Langevin function and λ_c is the chain stretch defined as $\lambda_c = \frac{1}{\sqrt{3}} (\lambda_1^2 + \lambda_2^2 + \lambda_3^2)^{1/2}$ where the subscripts 1, 2, 3 represent the

three principal stretch directions. The Langevin function is defined by $\mathcal{L}(x) = \coth(x) - 1/x$

Bischoff et al. found the unknown parameters (n and N) by curve fitting the simulation results to that of experimental results obtained by Dunn et al. in 1985. The parameter n corresponds to an initial modulus and dominates low-stretch behavior while parameter N dominates the large-stretch behavior. The physiological meaning attributed to these parameters is given below.

N - fiber-free length and n - network collagen chain density

However, this model is based completely on the effect of collagen fibers present in skin and does not include any correction to include the mechanical response of matrix (ground substance on which the collagen fibers exist). It should also be noted that the model parameters obtained by best-fit method did not represent the healthy skin data well

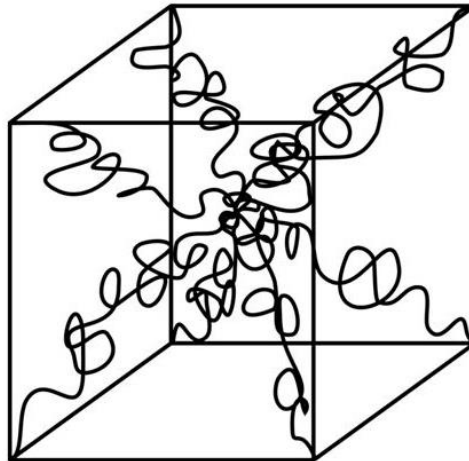


Figure 2-2: Isotropic eight-chain network of freely jointed chain model [Reproduced from Arruda and Boyce, 1993]

at high strains as shown in Figure 2-3. The parameters obtained in this method for a normal healthy skin were $N = 1.10$ and $n = 5 * \frac{10^{22}}{\text{m}^3}$

2.3.2 Planar Biaxial Testing Systems

In general, biaxial testing and its interpretation are considered more difficult and time-consuming to perform. In addition, the equipment is more expensive and not widely available. This section describes the planar biaxial testing system. Other kinds of biaxial state testing system are discussed in Section 2.3.3. One of the earliest 2D experimental biaxial device was developed by Lanir and Fung [Lanir and Fung, Parts i and ii, 1974].

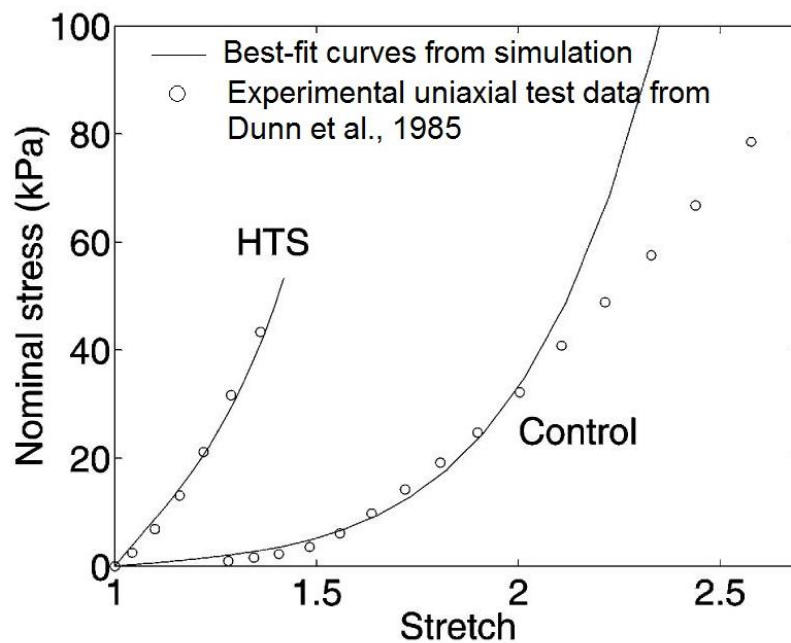


Figure 2-3: In-vitro uniaxial test data for normal and Hypertrophic scar (HTS) skin from Dunn et al. (1985) best fitted using an Isotropic eight-chain network of freely jointed chain model [Reproduced from Bischoff et al., 2000]

The experimental set up of the skin specimen in its temperature bath compartment is shown in Figure 2-4. This was an *in vitro* experimental set-up, where an optomechanical system had the rabbit skin specimen floating in physiological saline solution, with a thermoregulation compartment to maintain the specimen's temperature during the test. A square specimen of $35\text{ mm} \times 35\text{ mm}$ was cut out from an area exterior to the nipple line of rabbit. The specimen was then hooked by means of staples along its four edges. They were connected to a force distributor by means of silk threads. One end of the force distributing platform is rigidly mounted to a mechanism that slides in an orthogonal direction, while the opposite end of the platform is attached to a force transducer. The support and the transducer are connected to the carriage of another sliding unit. The carriages of opposite sliding units are connected by means of shaft-

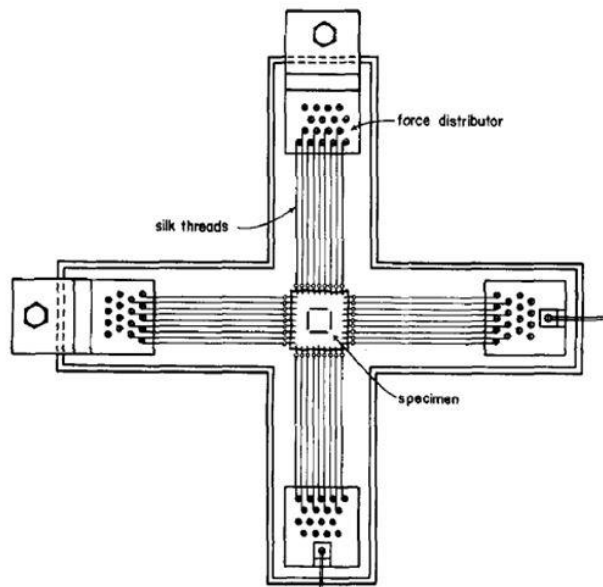


Figure 2-4: Optomechanical Biaxial Testing Device Set-up
[Reproduced from Lanir and Fung, Parts i and ii, 1974]

drive. The threads of the left and right sliding units are thus pulled in opposite direction at the same rate or contracted at the same rate. A side view of the whole optomechanical system is shown in Figure 2-5.

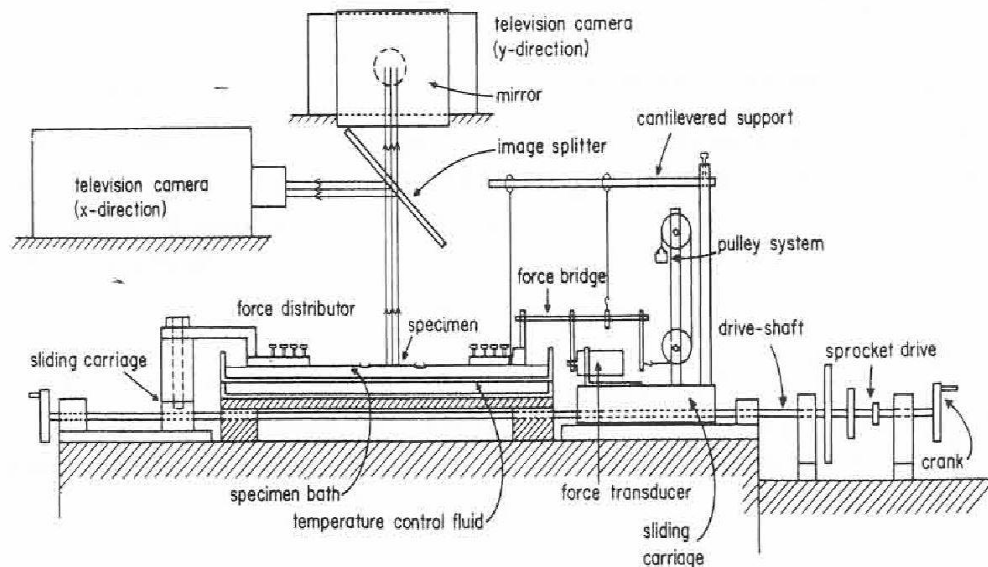


Figure 2-5: Schematic of optomechanical system. [Reproduced from Lanir and Fung Parts i and ii, 1974]

This set-up allowed the following types of tests to be performed on rabbit skin specimens.

- a. Quick Stretching (relaxation and creep testing) and slow stretching
- b. Biaxial slow-rate-of stretching
- c. Uniaxial slow-rate-of stretching
- d. Biaxial relaxation tests
- e. Uniaxial relaxation tests
- f. Effect of temperature on relaxation tests

The following major conclusions were reached from the biaxial tests performed on rabbit skin

- a. Stress-strain relationship was indeed non-linear
- b. Stiffness of skin increased with increasing strain rates
- c. Hysteresis was observed in all strain rates

Vito's [Vito, 1980; Choi and Vito, 1990] device was one of the first closed loop software based biaxial testing devices with multi-particle tracking allowed during the test. The main components of this biaxial system are the tissue bath, stretching mechanism, force measurement system, and dimension measurement system. They performed equibiaxial tension tests on a square specimen (cut from the original circular pericardium of dogs). Multiple test protocols were used to obtain stress-strain data under multiple loading states. This was accomplished by using constant ratios of strain or stress during each protocol, with a sufficient number of protocols and ratios chosen to cover the complete Green-Lagrange Strain ($E_{11} - E_{22}$) plane. Figure 2-6 shows their equibiaxial test set-up for dog pericardium. The main conclusion from their set of experiments is that the constants determined using an individual data set were not the "material constants". So they used the complete data set for each specimen to arrive at the "true material constants". These constants were able to give reliable material parameters for individual specimen. However, their analysis did not take into account any induced shear effects in the specimen.

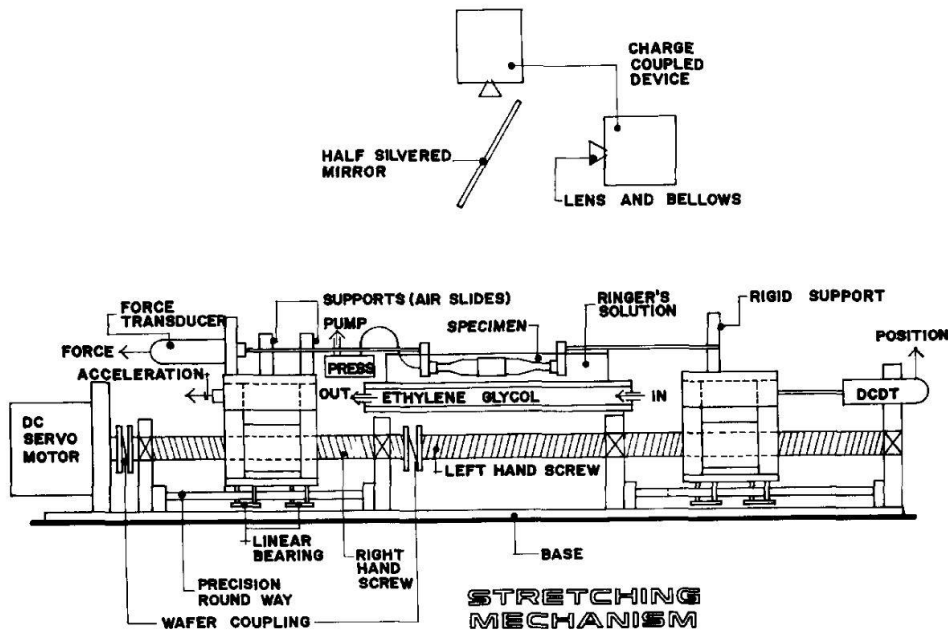


Figure 2-6: Vito's Biaxial Test Device set-up [Reproduced from Vito, 1980]

According to Nielsen et al. [Nielsen et al., 1991], the main shortcoming of the Lanir and Fung set-up is that it involves a time-consuming specimen preparation. The point forces needed to be separate and the strain rates did not measure as high as physiological strain rates. They modified the set-up slightly to add variations to Lanir's device as shown in Figure 2-7. This set-up was used to determine the mechanical properties of skin. In their set-up point forces are applied only at four sites, along each edge of the specimen.

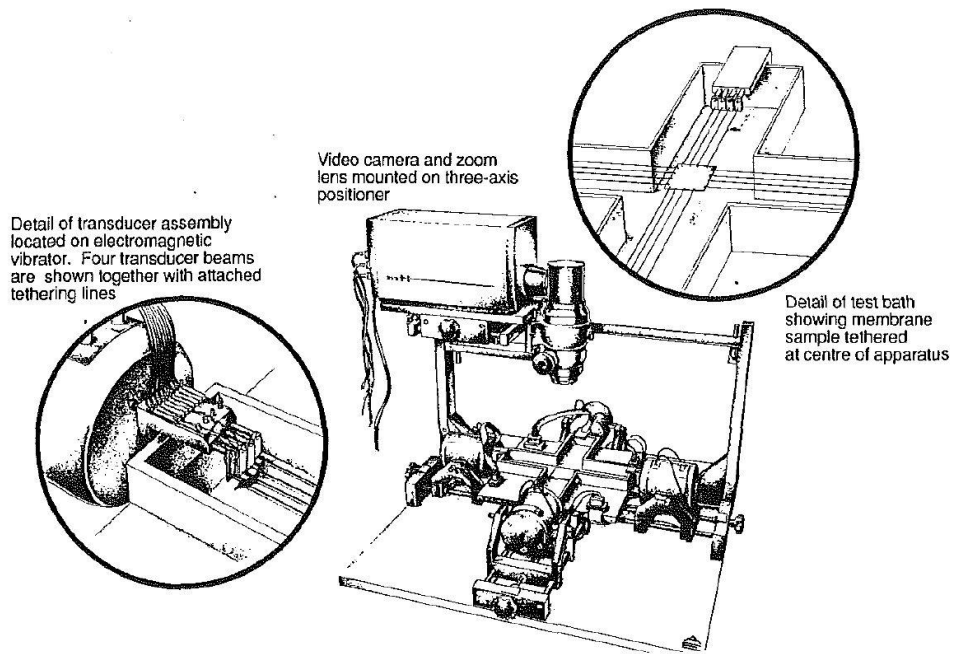


Figure 2-7: Nielsen's modified Biaxial set up from that of Lanir's set-up [Reproduced from Nielsen et al., 1991]

2.3.3 Other Experimental Techniques

The other main experimental techniques such as suction, torsion, and indentation are mostly done *in vivo*.

Suction blisters are produced by applying suction cups on the skin. The principle involved in suction test is very simple. The surface deformation of skin is created by partial vacuum and is visualized using any suitable imaging system. A schematic of such a device design [Hendriks et al., 2003] is shown in Figure 2-8. Here a partial vacuum is applied on to the skin causing it to deform and a 20 MHz ultrasound is used to measure the deformations in the skin specimen. A numerical-experimental method was used to characterize the non-linear mechanical behavior of human dermis. The material parameters were found from the experimental dataset by using an extended Mooney-

Rivlin strain energy function W of the form given below, to optimize for the skin material parameters

$$W = C_{10}(I_1 - 3) + C_{11}(I_1 - 3)(I_2 - 3) \quad (2-4)$$

where C_{10} and C_{11} are the unknown material parameters, I_1 and I_2 are the first and second invariant of the strain tensor. Mooney-Rivlin constants were found to be $C_{10} = 9.4 \pm 3.6 \text{ kPa}$ and $C_{11} = 82 \pm 60 \text{ kPa}$.

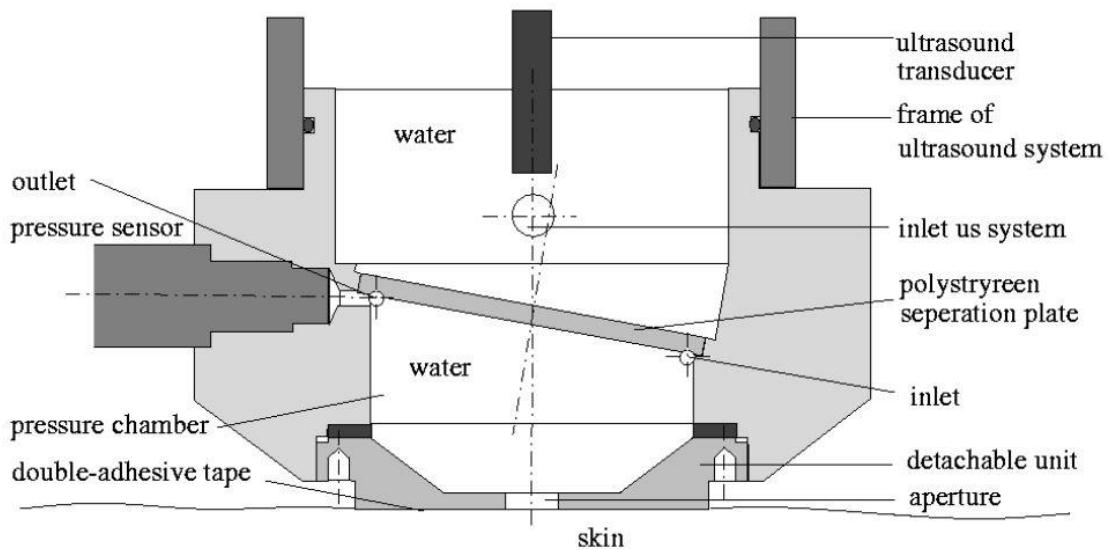


Figure 2-8: Schematic representation of the suction device attached to imaging system (ultrasound). [Reproduced from Hendriks et al., 2003]

Torsional tests are done by placing a central disc that is rotated while an encompassing ring remains fixed, thus creating a torque [Sanders, 1973].

In vivo tensile loading tests [Wan Abas and Barbenel, 1982; Lim, et al., 2008] are done by attaching two tabs on the skin and then pulling the tabs apart by a set of prescribed displacements. The force for the set of prescribed displacements is measured using a load cell as the skin deformation occurs.

Indentation test technique is a method where an indenter is applied to a skin site and the load is applied by pressing against the skin. The displacement measured on the indenter is used to quantify the material properties of skin along with the load applied. This method has been used to measure the response of different layers of skin by varying the size of the indenter. For example, a small indenter can be used to characterize the upper layers of skin while a larger indenter can be used to characterize the lower layers as well [Pailler-Mattei, et al., 2008].

2.3.4. Multiaxial Testing Systems

A custom built multiaxial testing device [Nielsen, et al., 2002], shown in Figure 2-9, was used to investigate the stress-strain properties of human skin *in vivo* by Kvistedal and Nielsen [Kvistedal and Nielsen, 2009].

In this set up 16 actuators arranged in a circular fashion allowed deformation to occur in 8 directions/axes. These actuators were capable of an incremental motion as small as 0.2 μm to a range of up to 50mm. A CCD camera was used to record the skin (marked with carbon powder to create a speckle pattern) deformations. A 2D finite element model was used to determine the material parameters. A strain energy function W of exponential form (modified from the original Tong and Fung's Strain Energy Density form) shown below (neglecting 3rd order terms) was used in this analysis to arrive at the optimized material parameters for skin.

$$W = \frac{1}{2}(\alpha_1 e_1^2 + \alpha_2 e_2^2) + \frac{1}{2}c \exp(a_1 e_1^2 + a_2 e_2^2) \quad (2-5)$$

where $\alpha_1, \alpha_2, c, a_1, a_2$ are the unknown material parameters obtained by an optimization routine; W is the strain energy function, e_1 is the strain along the Langer line (fiber direction), and e_2 is the strain across the Langer line (perpendicular to fiber

direction). With an initial estimate for the unknown material parameters, the algorithm looped through the parameters applying small increments to their value. After solving for each deformed state, residuals were calculated from the difference between the predicted and measured displacements of the data points. Based on a least square fit to these residuals a non-linear optimization algorithm was used to refine the estimates for the material parameters.

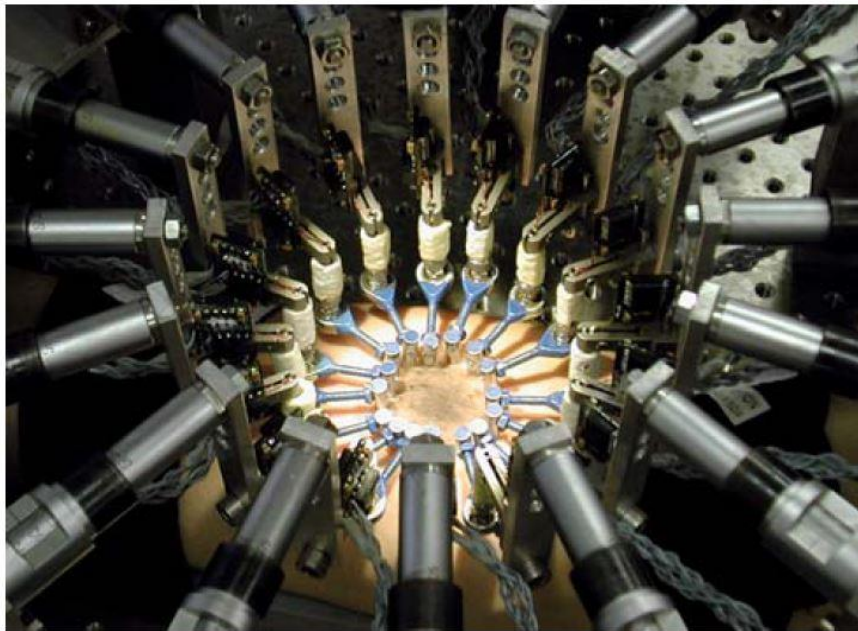


Figure 2-9: *In-vivo* Multi axial Testing set up. [Reproduced from Kvistedal and Nielsen, 2009]

2.3.5. Inflation /Blister/Bulge Testing

This is another type another type of *in vitro* biaxial testing method used to test biological specimens. The idea of bulge test has been in existence since Treloar [Treloar, 1944] first used this method to characterize rubber materials to find material constants in the early 1940's. The principle involves clamping the specimen between 2 plates and

inflating the specimen using air or water to cause a blister/bulge as shown in Figure 2-10. For a spherical membrane, the maximum membrane tension, T , is given by the Law of Laplace as

$$T = \frac{1}{2}PR \quad (2-6)$$

where P is the pressure applied and R is the corresponding radius of the sphere.

This idea can be used as the basis for an experimental method to test any membrane, such as a biological specimen. The inflated shape of an initially flat circular disk of an isotropic material is axisymmetric and the inflated shape of an anisotropic membrane will depend on the specific form of the material anisotropy. Inflating an initially-flat circular disk of an orthotropic material will produce a surface which will have oval contours with major and minor axes as the 2 direction of axes of elastic symmetry [Zioupes et al., 1992].

Bulge tests are not commonly used to characterize skin specimens, but there are at least 3 studies in literature where a bulge test has been used to study skin. In the study by Dick [Dick, 1951], the investigators only studied the response of skin to forces which was thought to be within physiological limits. The cadaver skin was subjected to pressure of up to 35 ($cm.H_2O$) $\sim 3.4 KPa$. The main conclusions were that cadaver skin from

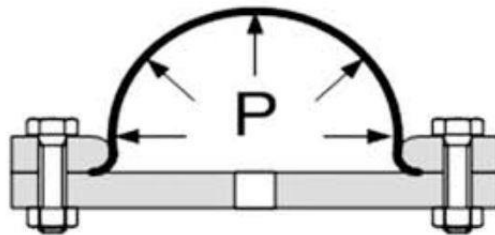


Figure 2-10: Bulge Test schematic

younger subjects expanded more gradually in comparison to that of older subjects. Although, no quantitative results were given, they concluded that skin from younger subjects was more compliant than that of older subjects.

In another study [Ahlfors and Billiar, 2007] that used the bulge test to investigate skin properties, the researchers tested the tensile strength of fibroblasts in natural human penile skin. As part of achieving their goal, they lysed the cells in the skin specimen using a chemical solution before performing the test, thereby eliminating the intrinsic tension produced by the fibroblasts in the skin specimen. Thus, we can safely say that their results were not obtained on the natural skin specimen but a modified pre-treated skin. So, the material properties obtained in their testing might not represent the natural skin properties because they would have changed due to the pre-treatment of skin.

The experimental bulge test set-up of a recent investigation of skin by Tonge et al. [Tonge et al., Part 1, 2012] is shown in Figure 2-11. The set-up designed by these investigators is very similar to the one that is discussed in this thesis and is therefore described in detail here.

The investigators used stereoscopic Digital Image Correlation (DIC) for full-field displacement measurements of the deformation. The main components of the experimental set-up are a pressure chamber, pressure transducer, two cameras (for 3D-DIC), and a Proportional-Integral-Derivative (PID) controlled syringe driven by MTS Insight 5 (MTS, Eden Prairie, MN, USA). The full thickness square specimens of dimensions $10\text{ cm} \times 10\text{ cm}$ were obtained within 24 hours of post-mortem and were immediately flash frozen for later mechanical testing. The flash frozen specimen was stored in -20°C temperature until ready for testing. The specimen was then thawed overnight in Phosphate Buffered Saline solution (PBS) at 4°C before testing. The

specimen was then glued to the plexiglas ring fixture (7.5 cm inner diameter and 9.5 cm outer diameter) and the pressure was controlled based on feedback from the pressure transducer. Samples were loaded from a baseline pressure of 0.276 kPa to a maximum pressure of 5.516 kPa at a rate of 0.069 kPa/second. The inflation of the specimen to an elliptical shape was observed and was used to confirm the anisotropy of skin. At each pressure step, the Green-Lagrange strain tensor (E) components were calculated over the entire specimen from the DIC displacement field.

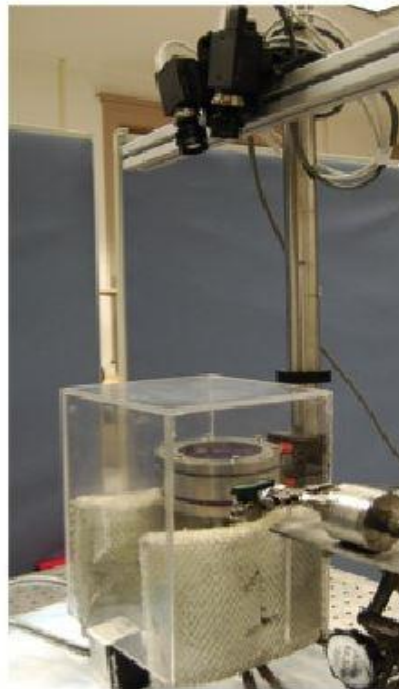


Figure 2-11: Pressure-controlled inflation system [Reproduced from Tonge et al., 2012]

After rotating the displacement components (u, v, w) obtained from DIC coordinate system (x, y, z) to displacement components (u', v', w') in the material coordinate system (x', y', z') , the corresponding strain components in the fiber (E_f),

perpendicular (E_p) and shear (E_{fp}) directions were calculated using the following equations:

$$E_f = E_{X'X'} = \frac{\partial u'}{\partial x'} + \frac{1}{2} \left[\left(\frac{\partial u'}{\partial x'} \right)^2 + \left(\frac{\partial v'}{\partial x'} \right)^2 + \left(\frac{\partial w}{\partial x'} \right)^2 \right] \quad (2-7)$$

$$E_p = E_{Y'Y'} = \frac{\partial v'}{\partial y'} + \frac{1}{2} \left[\left(\frac{\partial u'}{\partial y'} \right)^2 + \left(\frac{\partial v'}{\partial y'} \right)^2 + \left(\frac{\partial w}{\partial y'} \right)^2 \right] \quad (2-8)$$

$$E_{fp} = E_{X'Y'} = \frac{1}{2} \left[\frac{\partial u'}{\partial y'} + \frac{\partial v'}{\partial x'} + \frac{\partial u'}{\partial x'} \frac{\partial u'}{\partial y'} + \frac{\partial v'}{\partial x'} \frac{\partial v'}{\partial y'} + \frac{\partial w}{\partial x'} \frac{\partial w}{\partial y'} \right] \quad (2-9)$$

The corresponding stretches in fiber and perpendicular directions were calculated from the strain components (E_f, E_p). The local stress resultants (N_f and N_p) were calculated analytically for the bulged specimen from the inflation pressure P and the curvature, K_f and K_p , at the apex in the fiber and perpendicular direction using the following equations:

$$N_f = \frac{P}{2K_p} \quad (2-10)$$

$$N_p = \frac{P}{K_p} \left(\frac{2K_p - K_f}{2K_p} \right) \quad (2-11)$$

The anisotropic stress resultant-stretch relationship was characterized for 6 skin specimens by the authors. They also studied the effects of preconditioning and humidity on the skin specimens. They concluded from their experiments that there was minimum effect of preconditioning on specimen stress-stretch response. This conclusion is yet to be validated; in contrast, many studies in the biomechanics literature claim the effect of preconditioning on biological specimens to be astounding [Eshel and Lanir, 2001; Lanir and Fung, Part ii, 1974; Liu and Yeung, 2008]. Tonge et al. investigated only one point (the apex of the bulged shape) in their analysis even though they obtained full-field

displacement measurements from the experiment. Tonge et al. also explored different constitutive models through numerical simulations.

2.4. DISCUSSION

The literature reviewed in this chapter highlights the diverse experimental techniques used to characterize the mechanical response of skin. It also considered briefly the different BBMs that include skin. However, there are some areas that have not been thoroughly investigated in the skin mechanics literature. A key area is the availability of a constitutive model for breast skin to use in a BBM to predict deformation due to change in position. This is of great importance since preliminary experiments by our group on tracking the skin movement in the breast due to change in position prove the importance of including skin in the BBM and also the importance of using an appropriate constitutive model for breast skin. Even though some studies provide a reasonable constitutive model for skin, they are modeled using experimental results from human cadaver skin from the back or are modeled using experimental results from animal skin. This does not suffice for our purpose of including skin in our BBM, to predict deformation of breast due to body forces like gravity. In addition, these proposed skin model parameters using inverse analysis or a new form for W do not necessarily validate the experimental stress-stretch results in the complete stress-stretch regime.

This study aims to address some of these gaps to allow for a better understanding of skin mechanical properties and provide more robust constitutive parameters using an inverse experimental-numerical technique along with experimental methods.

Chapter 3: Testing Methods, Experimental Set-Up and Results

3.1 INTRODUCTION – BULGE TEST

The bulge test or bubble inflation technique was first developed experimentally by Treloar [Treloar, 1944]; it was then used to investigate deformation of vulcanized rubber. As discussed in the previous chapter, this test has since been commonly used to characterize the mechanical properties of thin films. A thin film is characterized by a thickness that is small in comparison to the in-plane dimensions, thereby facilitating the use of *ad hoc* theories of shells or membranes to characterize the deformations of the specimen.

In this type of mechanical test, a thin film of the material to be tested is clamped between two constraining plates both of which usually have circular holes in the middle. An inflation medium, which may be liquid or gas is then introduced into the chamber mounted on one side of the inflation fixture, causing the film to deform. The inflation pressure and the bulge deformation of the specimen are monitored as a function of time/pressure to provide load-deformation data from which material parameters are determined using elementary mechanics [Li Yong, 2004, Bosseboeuf et al., 1997n Tonge et al. (Part 1), 2013]. A bulge test schematic for thin films is shown in Figure 3-1. Here p is the pressure applied by the injected fluid and a is the initial radius of the circular material specimen and h is the apex deflection from the initial configuration.

After a few years of using this experimental method for performing inflation tests, it was used to characterize bio-solid materials as well. One of the initial experiments includes conducting the tests on human thoracic aorta specimens [Mohan and Melvin, 1983]. However, there are very few studies that use the same technique to characterize skin.

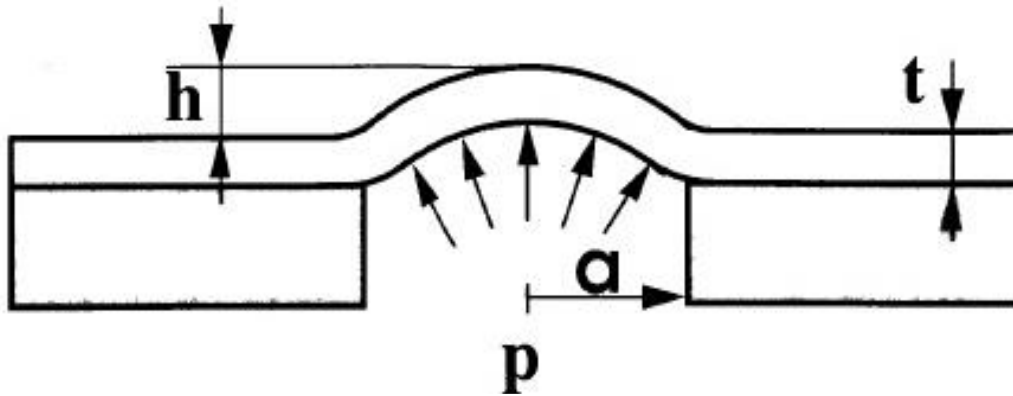


Figure 3-1: Schematic of Bulge/Inflation test set up of a thin film
 [Reproduced from Bosseboeuf et al., 1997].

3.2 BULGE TEST DEVICE DESIGN

The inflation or bulge test device consists of one clear acrylic hollow cylinder with an outer diameter = 4 in, inner diameter = $3\frac{1}{4}$ in, wall thickness = $\frac{3}{8}$ in, and height = 6 in. The hollow cylinder was glued to a flat square (6×6 in) clear cast acrylic plate of $\frac{1}{4}$ in thickness by means of permanent glue. The device also contained two circular acrylic plates each of wall thickness = $\frac{1}{4}$ in and outer diameter = 4 in. This cylinder, henceforth referred to as the pressure chamber, is attached to plate 1 (middle plate) by means of screws. Plate 2 (top plate) is attached to the middle plate by means of screws as well. The middle plate was machined to have 5 holes each of diameter $\frac{1}{2}$ in. These holes ensure contact of the tissue specimen with the inflating liquid solution from the pressure chamber uniformly. The middle plate also serves to avoid any bending of soft tissue specimen under its own weight. The top plate has an inner diameter of $2\frac{1}{4}$ in and was machined with an O-ring groove of $\frac{1}{10}$ in width and mean diameter of 3.09 in on the bottom side which acts as a means to seal any gap between the two plates as the specimen is placed in between. This set-up prevents any solution leak from between

the plates as the test is performed. Additionally the top plate has a curvature as shown in Figure 3-2 from the bottom to the top side of a radius $\frac{1}{4}in$ (through its thickness) to provide natural deformation of the specimen and avoid any tethering induced stress on the specimen. The detailed drawings of the chamber and its component plates, and the screw specifications are provided in the Appendix A with accurate dimensions as machined in the machine shop.

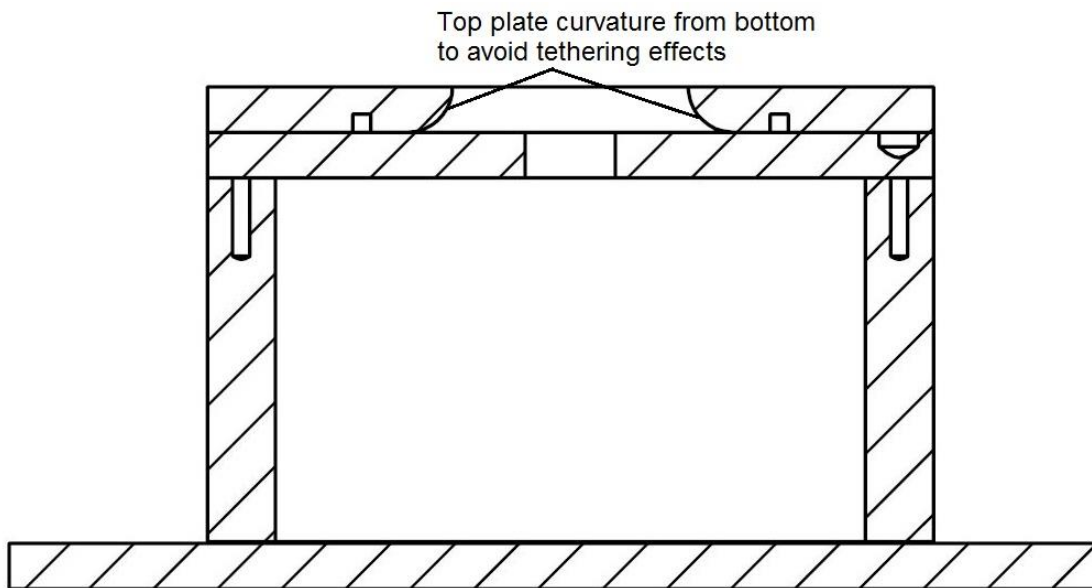


Figure 3-2: Sectional front view of the chamber showing the curvature on the top plate.

The pressure chamber has three access ports as shown in Figure 3-3. One port is connected to a two-way stopcock. One opening of the stopcock was connected to the pressure chamber (shown in Figure 3-3), and the second opening was connected to another two-way stopcock attached to the blood pressure transducer BLPR2 (World Precision Instruments Inc., Sarasota FL) with an operating range between -50 mm to +300mm Hg. The second port also acts as a bleed valve to release any air bubble from the

pressure chamber during the filling process. The third port is a release valve to drain all solution from the chamber when not in use.

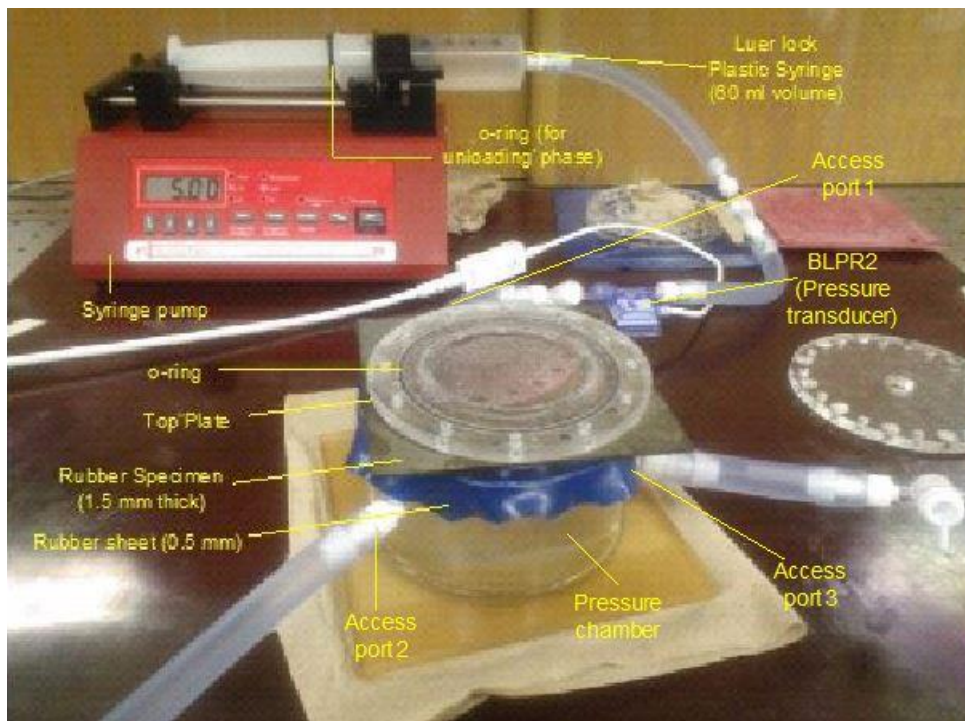


Figure 3-3: Picture showing the various components in the bulge test set-up. The blue rubber sheet is used to seal any leaks and the O-ring is used on the syringe in the unloading phase.

The other end of BLPR2's stopcock is connected to the luer-lock syringe (Plastic/Glass) using another 2-way stopcock. The luer-lock syringe volume is 60 ml (plastic syringe) or 100 ml (glass syringe) and is placed in a syringe pump. The syringe pump used in this device design is a NE 1010 programmable high pressure syringe pump (New Era Pump Systems Inc., Farmingdale, NY) using a RS-232 control interface. The pumping rate range for this pump depends on the volume of the luer-lock syringe used for pumping. A pumping rate as low as 58.3 $\mu\text{L/hr}$ and a maximum rate of 7635 mL/hr can be attained when a 60 ml luer-lock syringe with an inner diameter of 29.7 mm is used

with the pump. A pumping rate as low as 80.86 $\mu\text{L/hr}$ and a maximum rate of 9999 mL/hr can be attained when a 100 ml glass luer-lock syringe with an inner diameter of 34.9 mm is used with the same pump. A transducer signal amplifier, BP-1 pressure monitor (World Precision Instruments Inc., Sarasota FL) was used to amplify (maximum 100x gain) the signal from the BLPR2 pressure transducer. The BLPR2 is rated at 5 $\mu\text{volts per volt of excitation per mm of Hg pressure}$. The output from BP-1 for an excitation of 10 volts and a gain of 100 \times is therefore given by $5 \frac{\mu\text{V}}{\text{V}} \times 10 \text{ V} \times 100 = 5 \text{ mV per mm Hg}$. Detailed specifications on the hardware used in this design can be found online. The hardware and the software components used in this device are summarized in Appendix B.

3.3 BULGE TEST EXPERIMENT

After the device is set-up as shown in Figure 3-3, the specimen is placed in between the two acrylic bounding plates. The top plate is screwed through the specimen to the middle plate; the middle plate is then screwed separately to the top of the pressure chamber. A 0.3 mm thick rubber sheet with the same hole pattern as the middle plate is placed between the middle plate and the pressure chamber act as a gasket and prevent leaking of the inflating solution. One of the side ports in the pressure chamber is connected to the source of inflating solution through the transducer. In this present work, the inflating liquid used is water. We use a constant flow rate (5ml/min) of the inflating liquid rather than a constant pressure rate as used by other investigators, for example, Tonge et al., 2013, who performed similar experiments. The reason for using constant flow liquid to induce and monitor pressure is to avoid any instabilities that might be caused at large stretches due to a fixed pressure rate.

3.3.1 Removing the air bubble from the system

The pressure chamber is filled initially with the inflating liquid up to its brim with all the access ports closed. The luer-lock syringe and the tubes connecting them to the device are also filled with the inflating liquid carefully making sure that there are no air bubbles in the system. As the stopcock is opened to let the solution into the pressure chamber, there might be possibility of bubbles entering the system. These bubbles are removed manually using the second access port by inverting the whole system (after ensuring that it is completely closed from all possible leaks) and let the air bubble travel up through the port hole tube. The bubble has to be removed to avoid any mechanical compliance of the system [Bossboeuf, 1997]. The whole system has to be airtight to ensure valid experimental results. After the air bubbles are completely removed, the luer-lock syringe is refilled with the solution and the system is ready for pumping.

3.3.2 Experiment Precautions

A number of precautions are taken to ensure proper preparation, fixing, and loading of the specimens. The specimen sample holes are made by a skin punch tool typically used by surgeons for skin biopsy. In this work, a 3.5 mm Acu-Punch (Acuderm Inc., Fort Lauderdale, FL) was used to punch holes in the test specimens (includes rubber sheets 3.0 mm thick and porcine skin). This makes a clean and precise hole as per the screw measurements and helps avoid any leaking due to any extra holes or tear in the test specimen. When the screws are tightened from the top to the middle plate with the specimen in-between, it is best to keep the specimen as flat as possible. We used a cylindrical acrylic solid that fit the diameter of the top plate and held the specimen as flat as possible. This was done to avoid the entry of the inflating liquid through the 5 holes. High vacuum grease (Dow Corning Corporation, Midland, MI) was used in addition to

the rubber sheet to seal the middle plate to pressure chamber. When tightening the top plate to middle plate using screws, it is best if they are not done in one particular direction (like clockwise or anticlockwise) as this creates slack in tightening the screws and results in non-uniform bulging of the specimen while testing. Instead it is suggested to tighten them diagonally. For example, if there are 12 screw holes, then start tightening the 1st screw and then the diagonally opposite to the 7th screw, then the 2nd screw followed by the 8th screw, and continuing in that order. An O-ring is used on top of the syringe to ensure the syringe is held in place as the pump withdraws after the loading phase of the test. During the unloading phase of the test, there is a tendency for the syringe to slip as a whole rather than just withdrawing the injector. Placing an O-ring strapped around the syringe top as shown in Figure 3-3 avoids this movement thus ensuring the correct readings in pressure and the displacements in the unloading phase. When zeroing the pressure reading in BP1 monitor for the BLPR2 sensor, we have to make sure the complete system is air tight and is ready to test.

3.3.3 Experiment Protocols

The aim of the present work is to determine the constitutive parameters for soft tissues like skin using a hybrid experimental and numerical method. Since the bulge/inflation test itself is commonly used for solid materials from which a well-defined sample can be obtained, we need to have a fixed testing protocol in place for reproducible results.

Commercial rubber sheet specimens of thickness 0.3 *mm*, 1.5 *mm*, and 3.0 *mm* were purchased and tested. A square specimen of 5 *in* × 5 *in* was cut from the sheet and the screw hole positions (12 of them) were marked using a Sharpie™ marker. Following this the holes were made using a skin punch tool for the 3.0 *mm* rubber

specimen. The holes in the 0.3 mm thick specimen were made using a knife. The holes in the 1.5 mm thick specimen were made using a Leather Hole Punch Tool.

Porcine skin specimens were obtained from an abattoir in Austin, TX and were kept in the freezer in a freezer-safe box until testing. The skin specimens were obtained from the belly portion as reported by the abattoir. The skin was allowed to thaw for a few minutes in water before the removal of fat. The fat was removed manually using a surgical blade as uniformly as possible. The nominal skin thickness was then measured using a Vernier caliper in at least 8 locations and an average was calculated as the mean skin thickness for the porcine specimen.

3.4 DIGITAL IMAGE CORRELATION - INTRODUCTION

Any experimental mechanics testing technique such as the bulge test or a planar biaxial test relies heavily on the measurement of surface displacement field to perform further analysis. There are many optical techniques such as speckle pattern interferometry, moiré interferometry, or holography that have been in use since the late 17th century to measure such surface displacements. Due to the major limitations of these techniques such as those in the data processing step, the Digital Image Correlation (DIC) technique was proposed in the late 1980's for experimental stress analysis. DIC has become a very popular and widely used technique for experimental diagnostics, due to the ease in setting up the optical system and quantifying surface deformation measurements. When this method is used with a single camera the in-plane displacement/strain fields on the specimens can be obtained. By using 2 cameras, 3-D displacement and surface strain field can be measured [Pan et al, 2009; Chu et al, 1985].

DIC is a full-field optical method that employs pattern tracking and uses a stereo-vision based analysis to examine the 3D deformation measurements during any

mechanical test. This technique evaluates the change in the surface characteristics of a test specimen subjected to a user-defined mechanical test load. This technique is thus commonly used to measure displacement and strain, and can provide a 3D map of displacements and strains of the entire specimen surface (subjected to mechanical test) from a series of images. This technique has now attracted applications in other broader fields such as in studies of bio-materials, fracture mechanics, etc., [Yoneyama, S., and Murasawa, G.; 2009]

3.4.1 Basic Principle of 3D DIC

3D DIC is a non-contact full-field optical measurement technique that is rapidly enhancing the experimental mechanics discipline. This technique can be used for deformation measurements of both planar and curved surfaces.

3D DIC is based on stereoscopic binocular vision principle and a conventional digital image correlation technique. This principle is best explained by means of understanding the schematic shown in Figure 3-4. In this figure, O_{c1} and O_{c2} are the optical centers of the left and right cameras, respectively. Here a point P on the specimen or testing material is imaged as P_1 by the left camera and P_2 by the right camera. Using stereoscopic vision and DIC techniques the 3D coordinates of the point of interest P with respect to a global coordinate system can be determined from P_1 and P_2 . This 3D correlation technique always uses 2 cameras to determine the 3D coordinates of the point of interest P or a region of interest on the surface of the specimen from two different orientations and positions. To determine the 3D coordinates of point P , a world coordinate system needs to be established which is done by means of calibrating the 2 camera sensors using a standard calibration target. The final 3D shape reconstruction is based on the world coordinate system obtained by means of calibration.

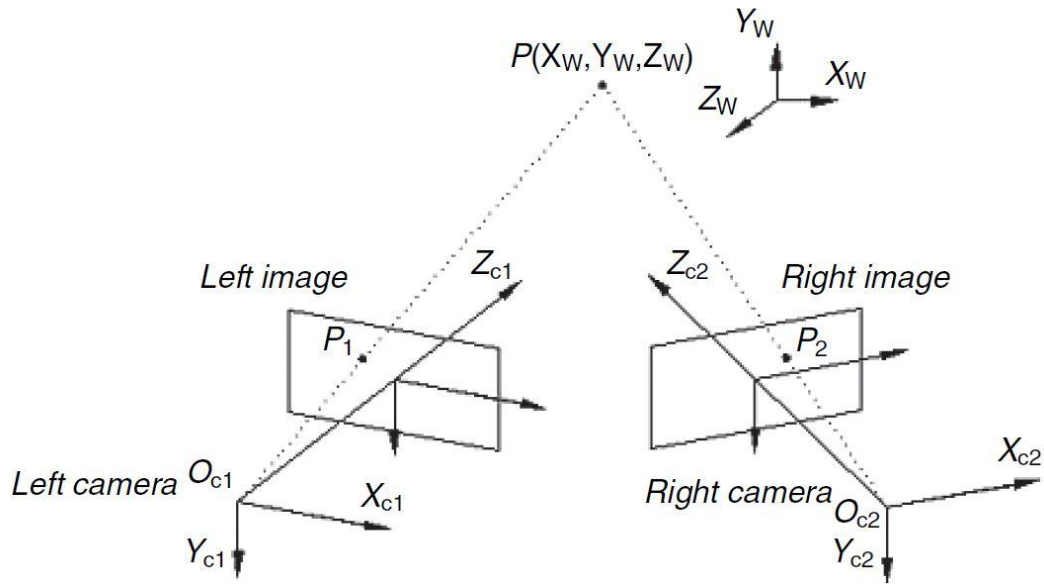


Figure 3-4: Schematic of 3D DIC technique. [Reproduced from Pan et al., 2009]

3.4.2 Camera Calibration and DIC Technique

Prior to actual imaging of the specimens for deformation measurements, the cameras need to be calibrated using calibration panels or targets. The commercial software ARAMIS™ (GOM, Germany) was used to calibrate the 2 cameras using a standard calibration panel that comes with the system. This calibration panel is a series of dots placed on a rigid plate surface. The calibration panel is imaged in different orientations (rotated 30°, 90°, 180°, 270°) and positions (near the lens, far from the lens) such that it fills the desired field-of-view for the actual measurement (of the specimen bulge) step. A series of snapshots of the calibration panel is then analyzed by the ARAMIS™ software allowing the position of cameras relative to each other and the other internal parameters of each lens to be accounted for in its calibration file that is created at the end of calibration of these images. For deformation analysis of the images,

the calibration file is provided as an input based on which the strain and displacement gradients are calculated. This calibration file is valid as long as the settings of camera lenses (focus) or the position of cameras relative to each other are not changed.

The ARAMISTM software uses a correlation algorithm that defines a field of “subsets” or “facets” on the specimen’s surface using the digital images captured from the 2 cameras. These subsets are **N by N** pixel square boxes that contain an array of pixel gray-scale values. For the correlation to work, each facet must contain a unique “fingerprint” or “signature” of gray scale values. This is ensured by creating a random speckle pattern on the specimen surface prior to the actual imaging. A speckle dot pattern of diameter about 7-12 pixels works best when viewed by the cameras used in this work. Such a speckle pattern was created on both rubber and skin specimens by means of using a bullet point SharpieTM permanent ink marker. In case of rubber specimens, to provide a better contrast on the speckle pattern, a spray paint (white color) was used to create a fine speckle pattern and then a Sharpie was used to create the contrast against the white fine speckle dots. For porcine specimens, the speckle pattern was created by placing random closely spaced dots using a bullet point Sharpie permanent ink marker. The speckle pattern is important for the purposes of correlations [Moerman et al., 2009] and hence was made carefully.

By matching facets across two calibrated cameras, along with the camera parameters such as focal length, displacement fields, $\mathbf{u}(\mathbf{x})$ are calculated in all three dimensions. Strain can also be calculated by analyzing deformation of the facets over time. The displacement field is then used with continuum mechanics definitions of strain (see Section 3.6) to calculate the strain field on the specimen’s surface.

The settings used in ARAMIS™ for all DIC measurements included in the current work are shown in Table 3-1. No filtering was applied to our image data to reduce noise and thus default filter settings were used.

Table 3-1: Parameter settings for ARAMIS™ displacement-strain calculations

Parameters	Displacement	Strain
Facet Size	20	20
Facet Step	14	14
Computation Size	-	3 (default setting)
Validity quote	-	55% (default setting)
Maximum Deviation	0.4 (each stage)	-

In the bulge tests performed, the first image taken was considered to be the reference configuration and is assumed stress-free; DIC revealed a specimen surface that was flat to be within 0-0.1 mm. This image was used as the reference image, and then a series of images were taken at 1 second time intervals during the deformation/pressurization process. The sequence of deformed images shows variations in the random dot pattern, resulting from the bulge deformation, relative to the initial undeformed reference image. DIC then reveals the entire displacement field during the bulge deformation process. The out-of-plane displacement of the specimen and the surface components of the Green-Lagrange strain tensor were calculated using ARAMIS.

3.5 EXPERIMENTAL RESULTS

The experimental results of the bulge/blister test for both rubber specimen and porcine skin are described in this section.

3.5.1 Rubber sheet specimens

A typical bulge for rubber sheet of thickness 3.0 mm at a pressure of 13 kPa generated from ARAMIS using DIC is shown in Figure 3-5. This shows the bulge of the specimen with a color plot overlay on the specimen to show the out-of-plane displacement in the specimen. The maximum displacement ('apex displacement') is about 10.0 mm and is seen in the center of the specimen. Figure 3-5 shows the apex point as marked in the specimen and the center section used to generate the bulge profile for different specimens and at different pressure values later in this section. The circular symmetry of the out-of-plane displacement field is indicative of isotropy of the material up to this stage of loading.

The overall variation of the apex displacement with pressure of the 3.0 mm thick rubber specimen is shown in Figure 3-6. Figure 3-7 shows the contour plot of out-of-plane displacements of all points on a 3.0 mm rubber sheet specimen for the four pressure levels marked in Figure 3-6. The non-linearity in the response is evident from Figure 3-8 which shows deflection of all points on a section (shown in Figure 3-5) through the specimen center at different pressures. In case of the rubber specimen of thickness 3.0 mm (Figure 3-8), the apex displacement rises rapidly as the pressure increases to about 0.2 kPa after which there is a much sharper pressure rise with apex displacement. The test was stopped at a maximum pressure of 13.0 kPa which corresponds to a displacement of 9.8 mm. Figures 3-9 and 3-10 show the major and minor strain contours recorded experimentally for the pressure values corresponding to the points marked in Figure 3-6 in a 3.0 mm rubber. Figure 3-11 shows the variation of the major and minor strain at the apex point with respect to time (in seconds) or strain stage (as shown in the ARAMIS software). This corresponds to a pressure increase from 0 to 13 kPa in the first 226 stages,

and a decrease to about 1 kPa over the next 175 stages. It is noted that the major and minor strains are equal at the apex, indicating an equibiaxial strain state and an isotropic material response for the rubber. A comparison of the experimental bulge profile to that of the simulated profile (using ABAQUS) for these pressure values will be discussed in Section 3.7.

Bulge tests were also performed on rubber sheet specimens of thickness 0.3 mm and 1.5 mm. Figure 3-12 shows a comparison of the apex displacement for varying pressures for all the three specimens of varying thickness. The tests on 0.3 mm rubber sheet was only performed up to a pressure of about 2.6 kPa as the system started leaking beyond this pressure value due to inability of the specimen to seal leaks from between the

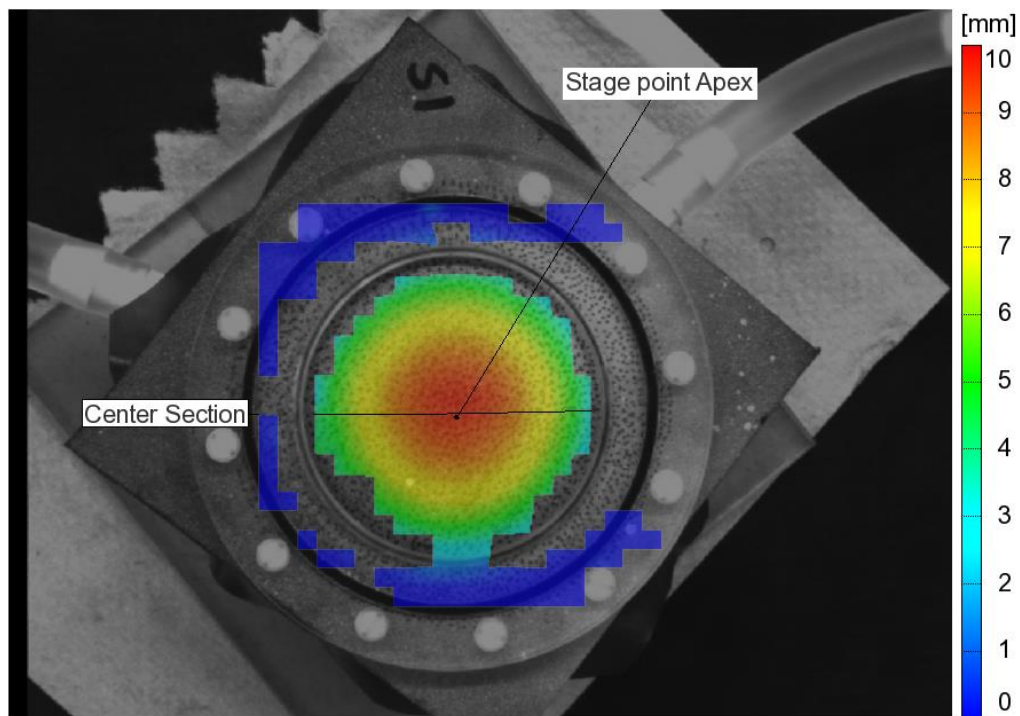


Figure 3-5: Overlay of the full-field u_z displacement with that of the rubber sheet specimen, when $P = 13$ kPa.

two plates (top and middle). However for the 1.5 mm and 3.0 mm thick rubber sheet specimen, the bulge test was performed up to a pressure 13 kPa.

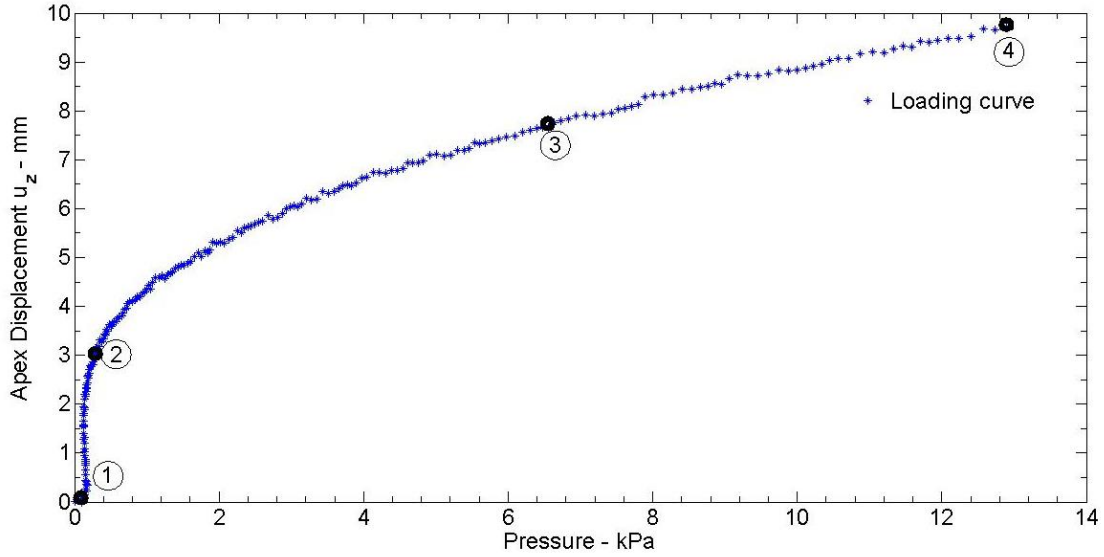


Figure 3-6: Pressure vs Apex displacement for rubber sheet - 3.0 mm thick (Experimental data)

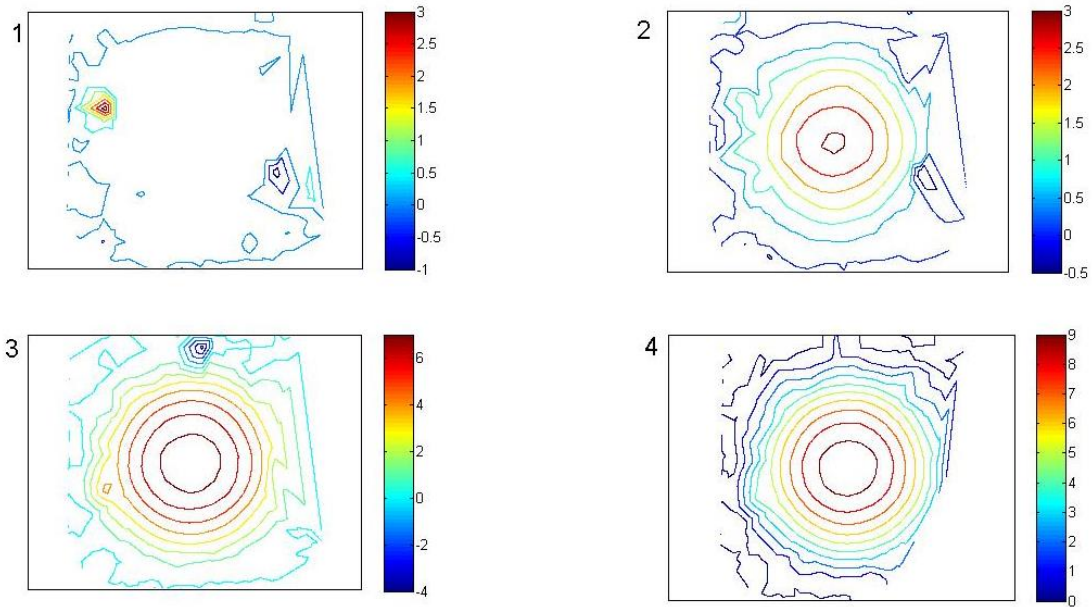


Figure 3-7: Displacement contour plots for pressures corresponding to points 1, 2, 3, and 4 from Figure 3-6

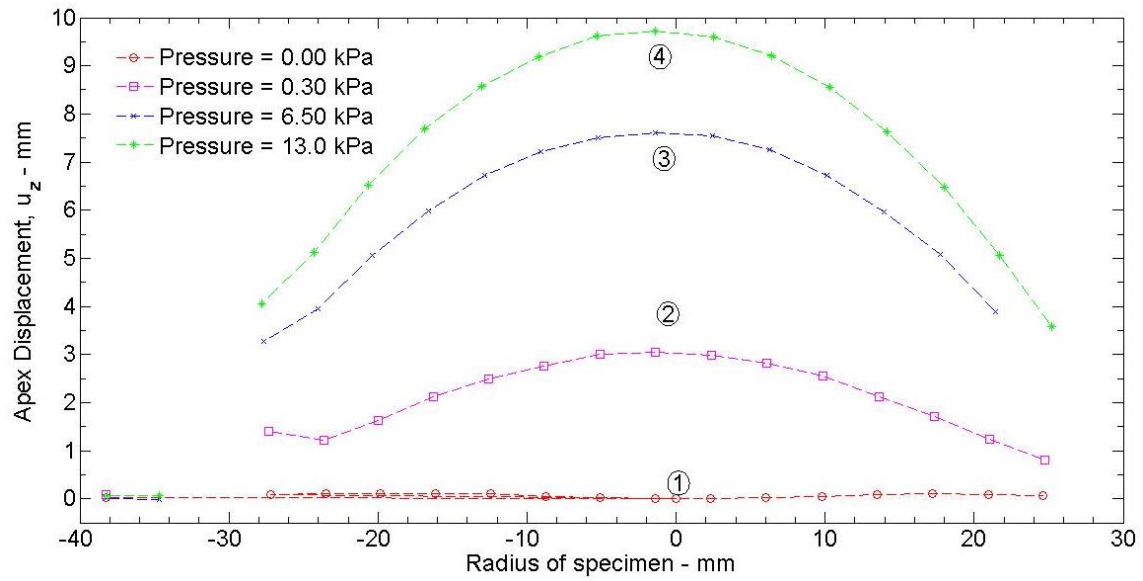


Figure 3-8: Bulge profile for pressures corresponding to points 1, 2, 3, and 4 from Figure 3-6

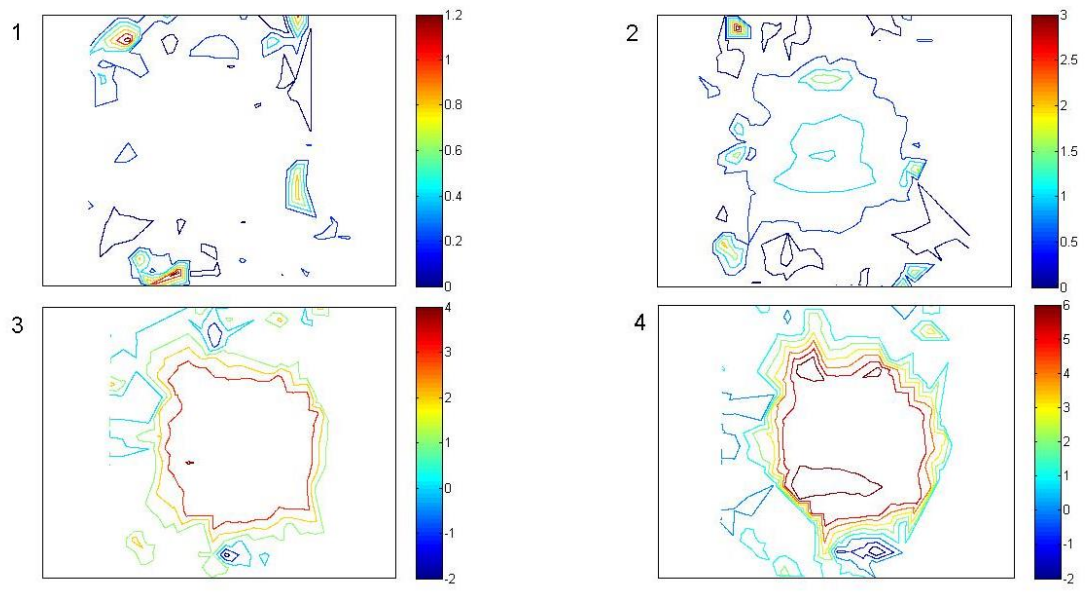


Figure 3-9: Major strain contour plots for pressures corresponding to points 1, 2, 3, and 4 from Figure 3-6

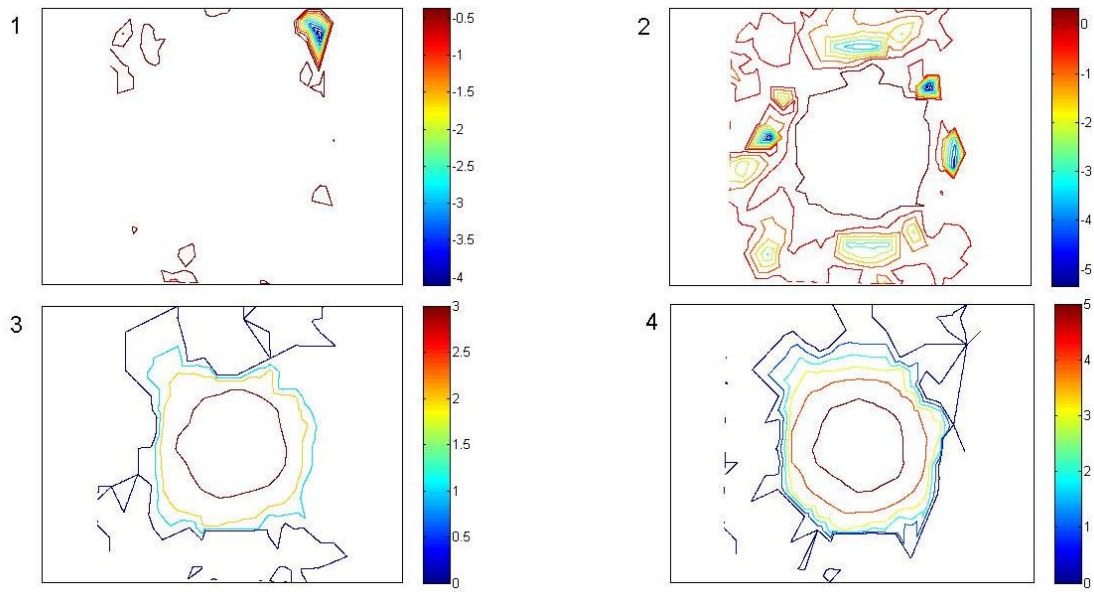


Figure 3-10: Minor strain contour plots for pressures corresponding to points 1, 2, 3, and 4 from Figure 3-6

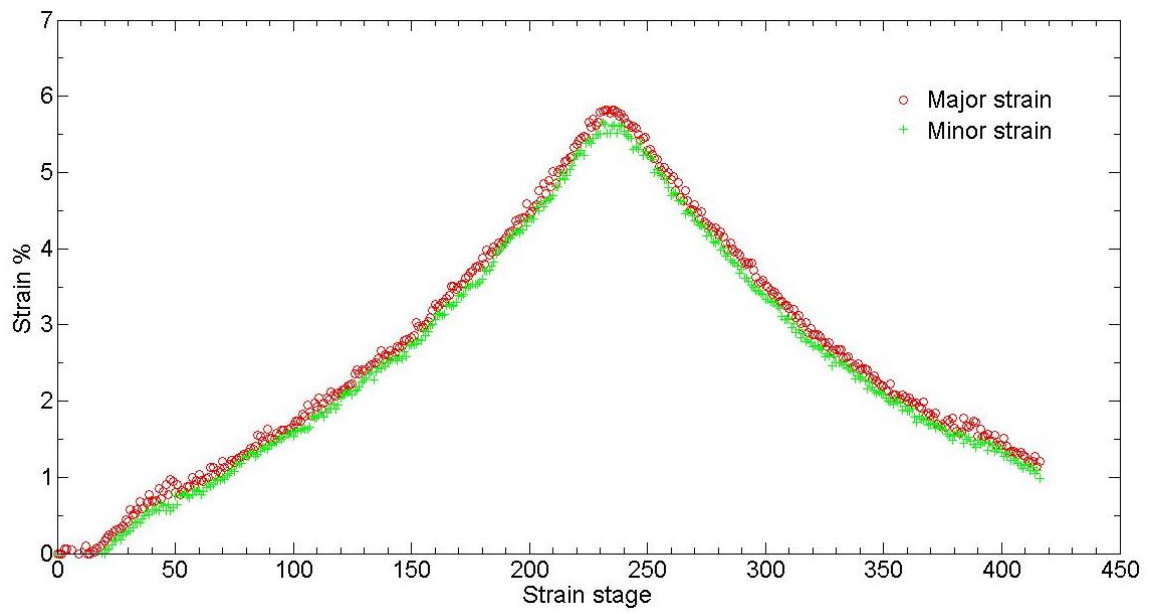


Figure 3-11: Apex Major and Minor strain Vs Strain stage (Time) plots for rubber (3.0 mm thick)

The absolute value of out-of-plane displacement for initial pressures for rubber specimens 0.3 mm and 1.5 mm thick were not reliable due to slipping, bubble formation and leaking issues encountered while performing the test. However, uniformity was established beyond a pressure level of about 1 kPa. It is evident from Figure 3-12 that the most compliant rubber (0.3 mm) had a larger displacement value for a smaller pressure value. Figures 3-13 and 3-14 are plots showing the variation in the bulge profile of the different rubber sheet specimens for a pressure of 2.6 kPa (highest pressure recorded for 0.3 mm thick rubber sheet experimentally) and 13.0 kPa. The bulge profile shown here is obtained from a section (similar to that in Figure 3-5) through the center of the specimen sheets. The thickest rubber specimen (3.0 mm) has the smallest bulge profile confirming that it is the least compliant specimen. The displacement recorded at the apex point for the different rubber sheets and the corresponding strains reached is summarized in Table 3-2.

Table 3-2: Maximum displacement and strains recorded in experiments on rubber sheets

Rubber sheet thickness in mm	Maximum Displacement recorded in mm (Apex point)	Pressure corresponding to the recorded displacements in kPa	Strains recorded at maximum displacements in %
0.3	14.93	2.6	8
1.5	16.60	13	16
3.0	9.72	13	6

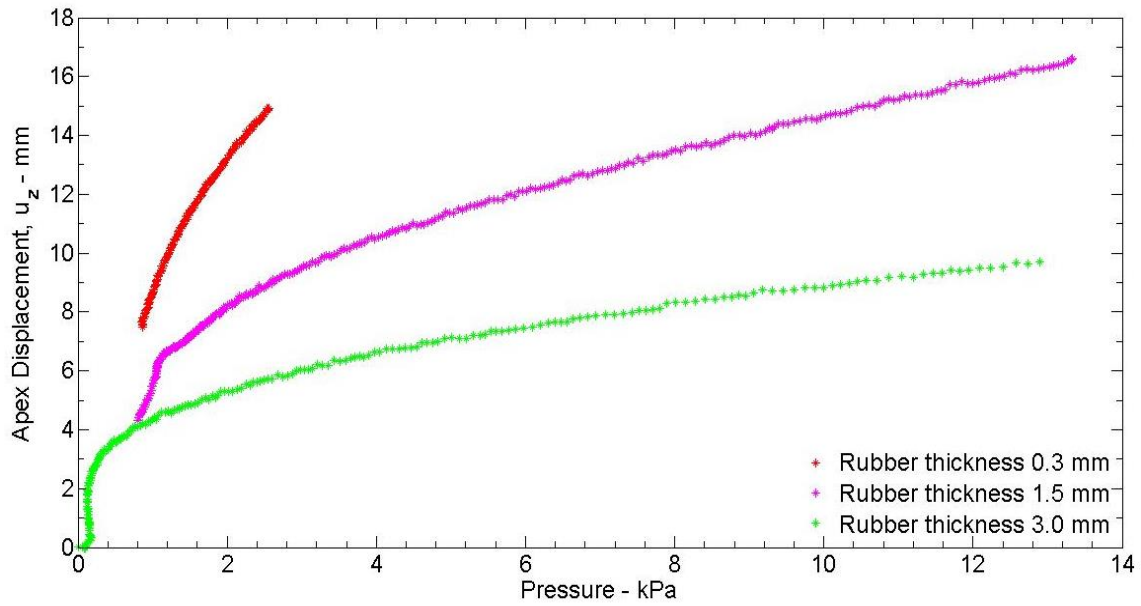


Figure 3-12: Pressure vs. Apex displacement for all 3 rubber sheet specimens (Experimental data)

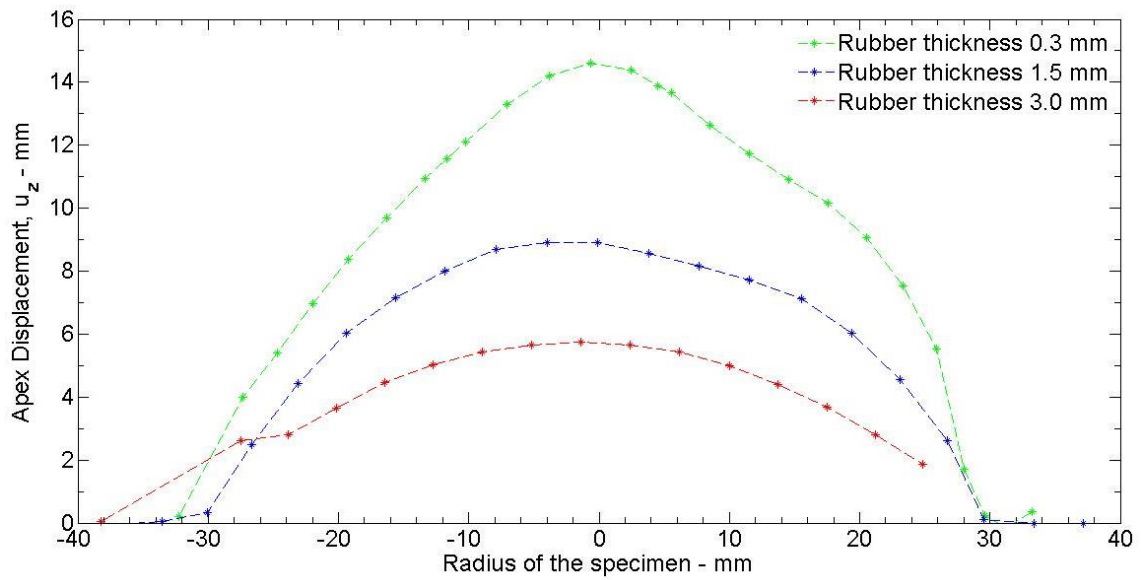


Figure 3-13: Bulge profile for different thickness rubber sheet specimens at a pressure of 2.6 kPa.

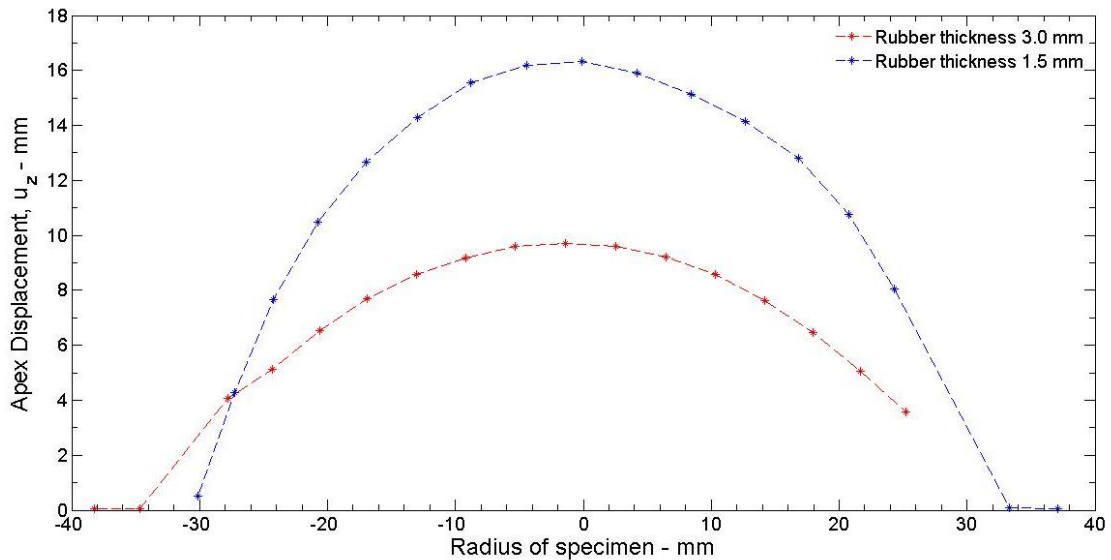


Figure 3-14: Bulge profile for different thickness rubber sheet specimens at the maximum pressure of 13.0 kPa.

3.5.1 Porcine skin specimen

A typical bulge for porcine skin generated from ARAMIS using DIC is shown in Figure 3-15. This shows the bulge of the specimen with a color plot overlay on the specimen to show the maximum displacement in the specimen. The maximum displacement is approximately 10.9 mm and is seen in the center of the specimen. An axisymmetric shape of the bulge was observed (Figure 3-15) indicating that the skin sample obtained and tested from the pig's belly region exhibits nearly isotropic behavior, but this will be examined quantitatively.

The pressure vs. apex displacement relation for the porcine skin specimens during loading is derived from the experimental pressure recorded and the displacements recorded using ARAMIS's 3d DIC system. Similar to the response of the rubber, the

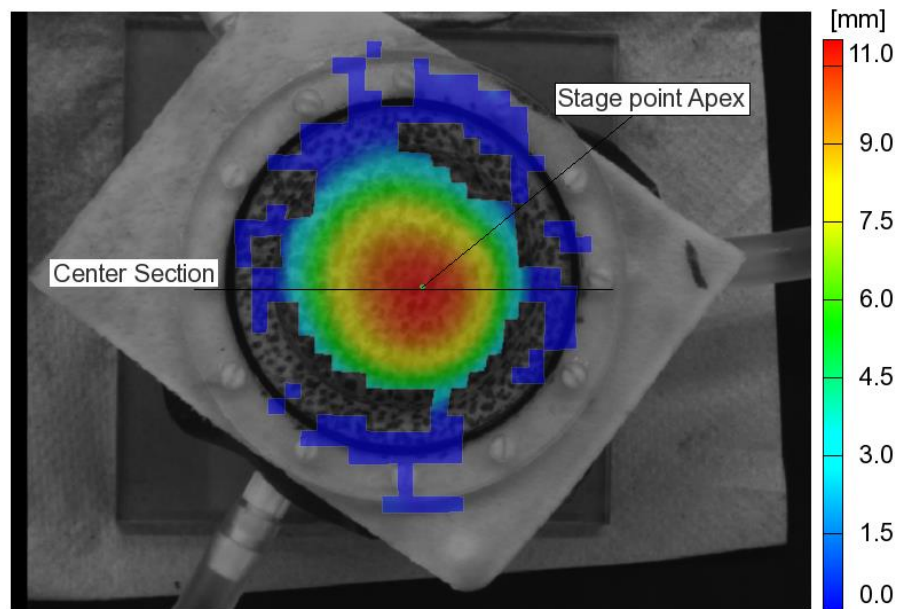


Figure 3-15: Overlay of the full-field u_z displacement with that of the actual porcine skin specimen, when $P = 13$ kPa

porcine specimen (Figure 3-16), indicates a rapid increase in the apex displacement during the first 1 kPa, but a much more gradual increase in the apex displacement beyond this pressure level.. For porcine skin, the test was stopped at a pressure of 13 kPa, which corresponded to 10.9 mm displacement at the apex point on the specimen. No visible damage was observed in the specimen for this pressure value. Figure 3-17 shows the contour plot of out-of-plane displacements of all points on the porcine specimen for the four pressure values marked in Figure 3-16. The non-linearity in the stress-strain curve is evident from Figure 3-18 which shows deflection of all points on a section (shown in Figure 3-15) through the specimen center at pressures corresponding to points marked in Figure 3-16. Figures 3-19 and 3-20 show the experimental major strain and minor strain contour plots at pressures corresponding to points marked in Figure 3-16. Figure 3-21

shows the variation of major and minor strain at the apex point (marked in Figure 3-15) with respect to time (in seconds) or strain stage (as shown in the ARAMIS software). A systematic difference is observed between the major and minor principal strain levels, suggesting anisotropic material response; this result points to the need for an anisotropic material model to capture the response of porcine skin.

The experimental results obtained from the DIC method was later compared with the numerical simulations (from ABAQUS) to find the material parameters for both rubber and porcine skin. The numerical simulations of the bulge test were done based on Finite Elasticity theory which is described in Section 3.6.

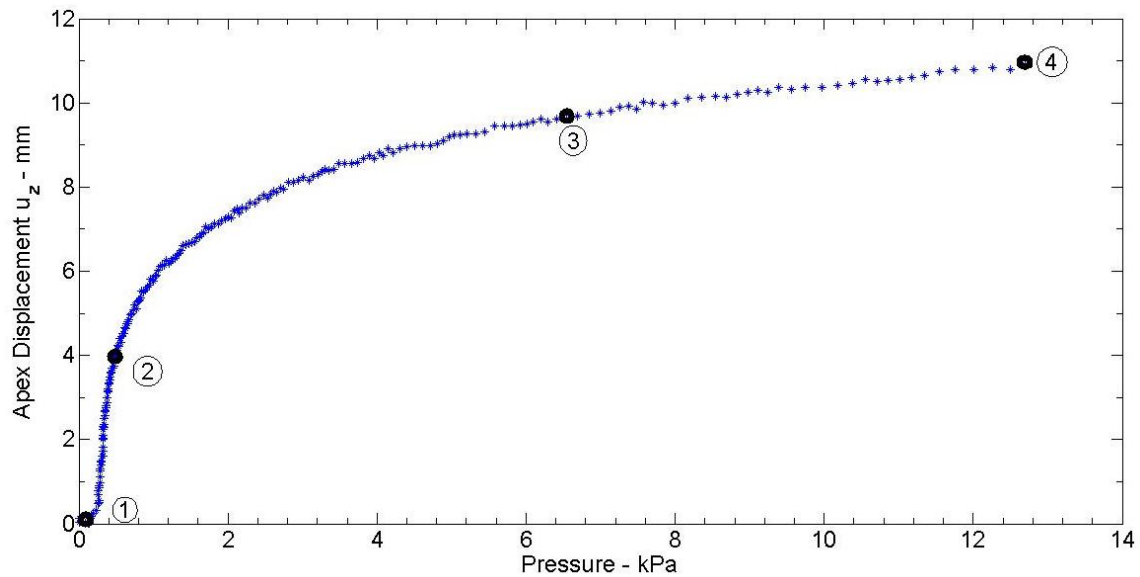


Figure 3-16: Pressure vs. Apex displacement for porcine skin (Experimental data)

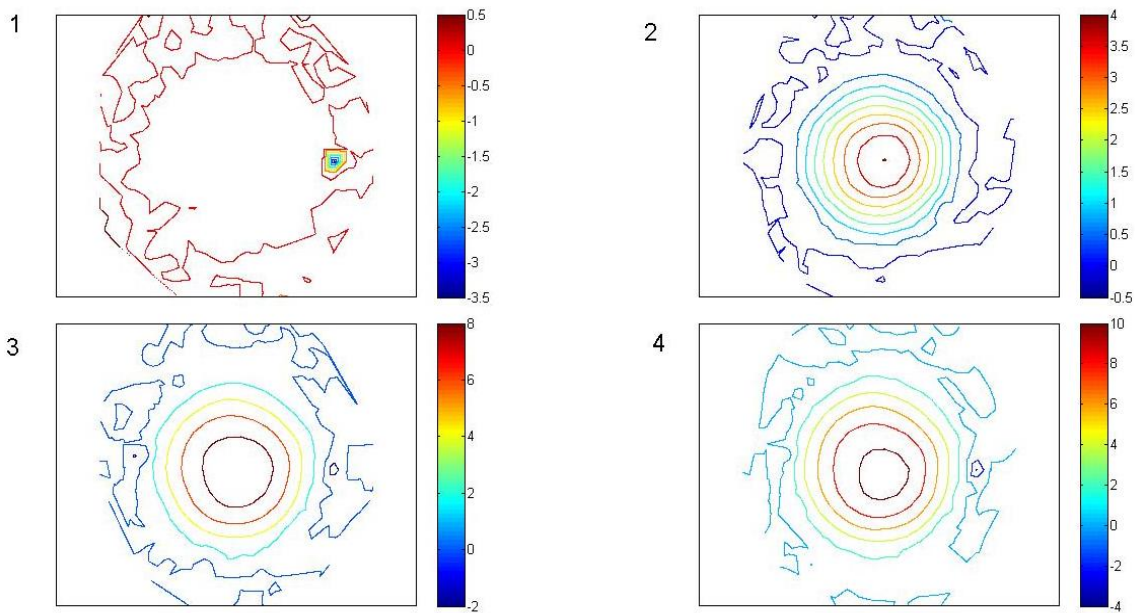


Figure 3-17: Displacement contour plots for pressures corresponding to points 1, 2, 3, and 4 from Figure 3-16

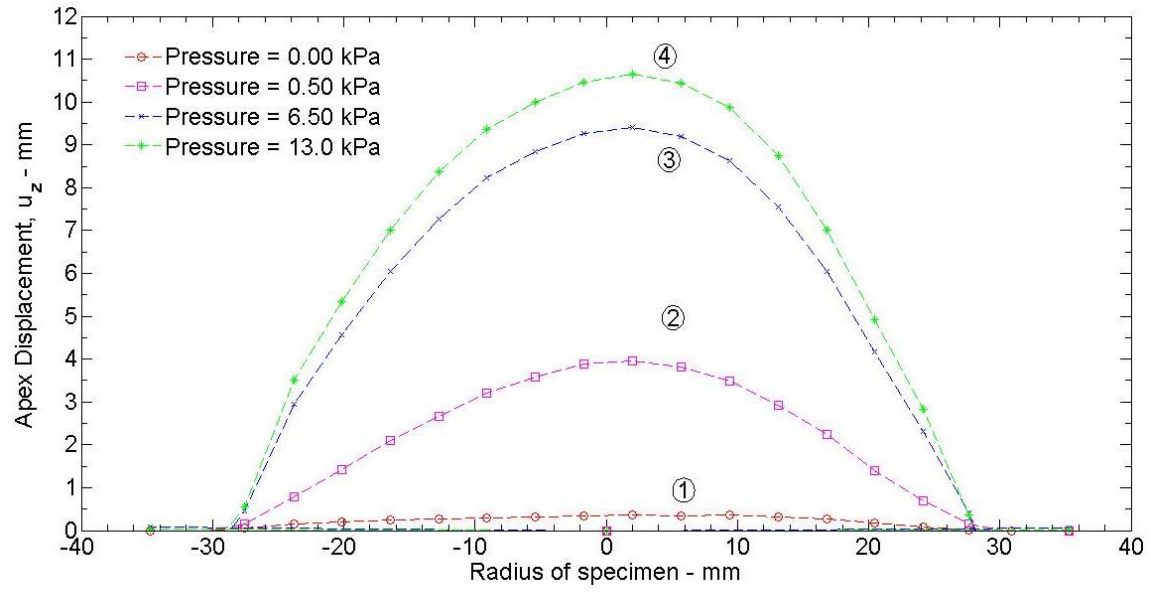


Figure 3-18: Bulge profile for pressures corresponding to points 1, 2, 3, and 4 from Figure 3-16

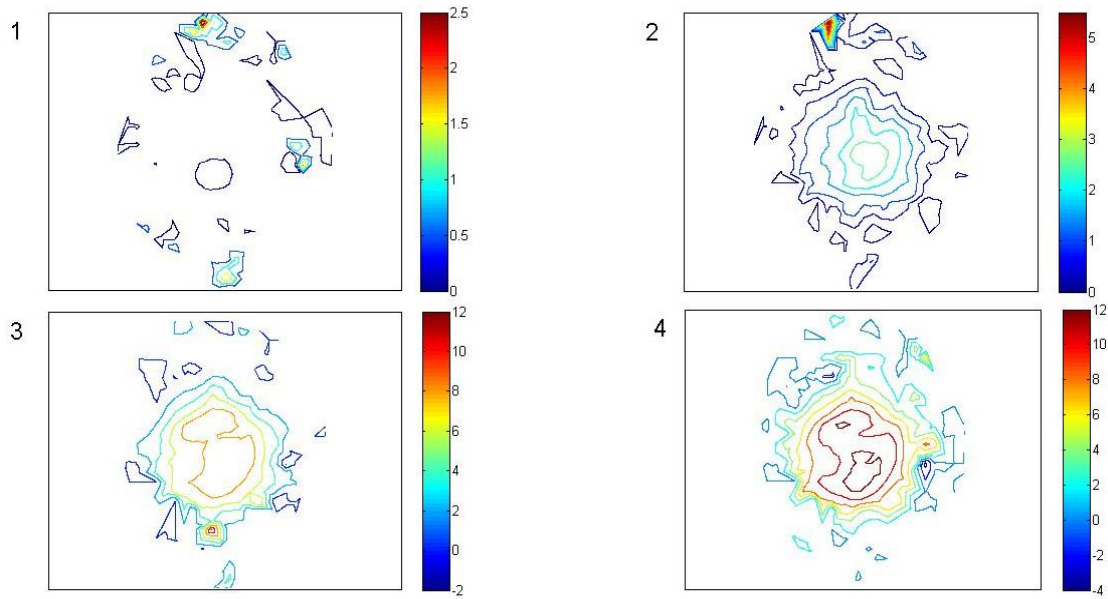


Figure 3-19: Major strain contour plots for pressures corresponding to points 1, 2, 3, and 4 from Figure 3-16

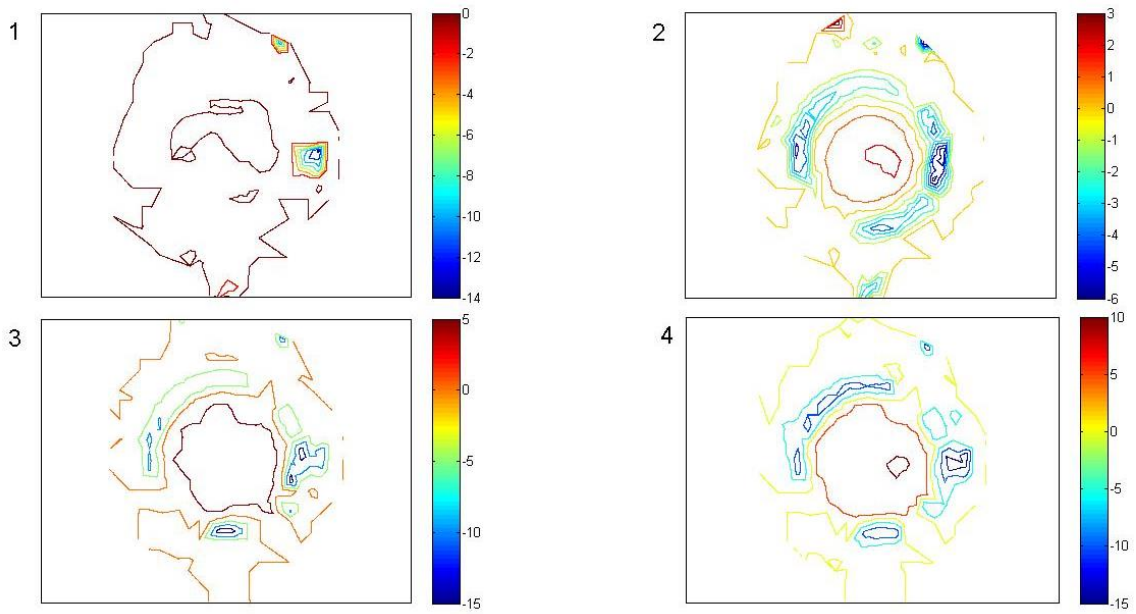


Figure 3-20: Minor strain contour plots for pressures corresponding to points 1, 2, 3, and 4 from Figure 3-16

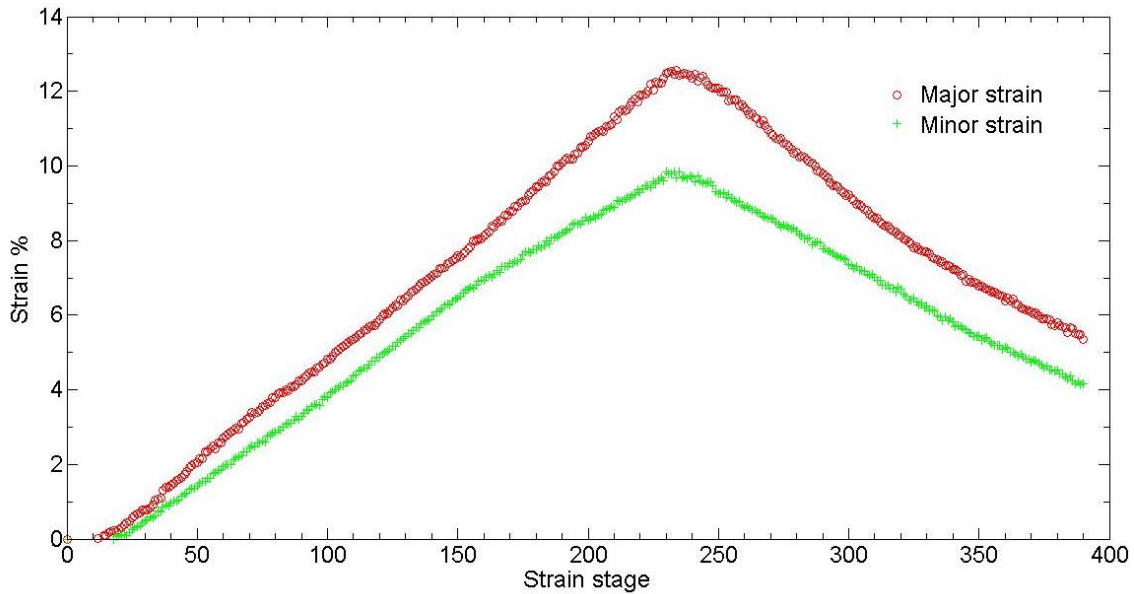


Figure 3-21: Apex Major and Minor strain vs. Strain stage (Time) plots for porcine skin

3.5.1.1 Viscoelastic response:

A cyclic loading test was performed on the porcine skin specimen to examine the effects of viscoelasticity. Figure 3-22-a shows the cyclic loading applied to the porcine skin specimen with respect to time. Figure 3-22-b shows the displacement response with respect to time at a point in the center of the specimen (Apex point). Figure 3-23 shows the displacement response to the applied cyclic loading (pressure) on the porcine skin specimen. The porcine skin was subjected to 5 cycles of loading and unloading. We observed that even though the pressure-time cycle was varied between 0 to 13 kPa (Figure 3-22-a) steadily, the displacement of the apex did not return completely to zero (Figure 3-22-b) upon unloading, but retained a residual displacement of up to 7.5 mm (Figure 3-23) in each cycle and was reasonably consistent with the number of cycles as

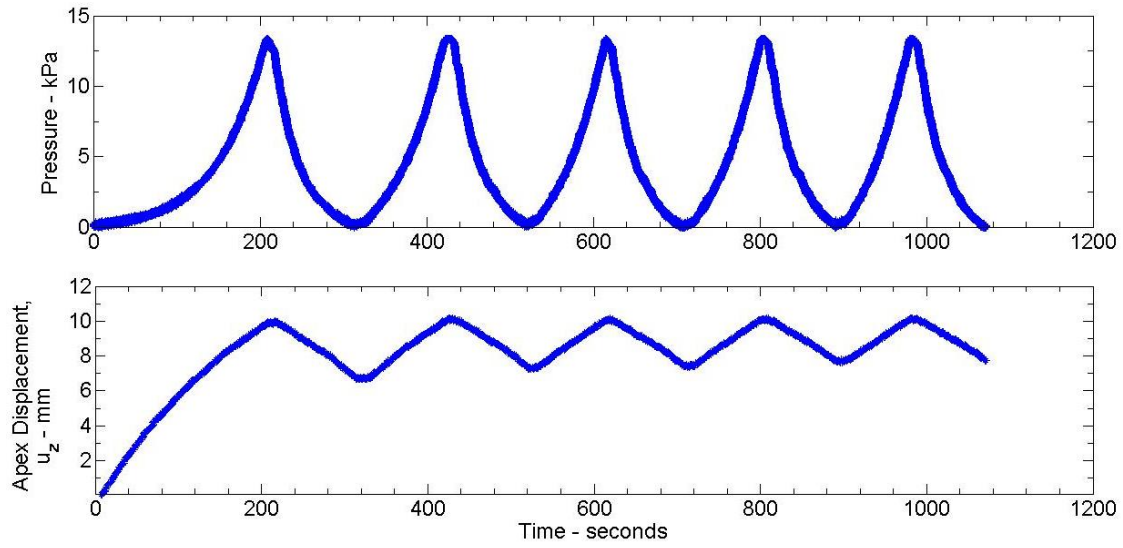


Figure 3-22: a) Pressure profile for cyclic loading and unloading for 5 cycles to study viscoelastic response.
 b) Apex displacement profile for cyclic loading and unloading - for 5 cycles to study viscoelastic response.

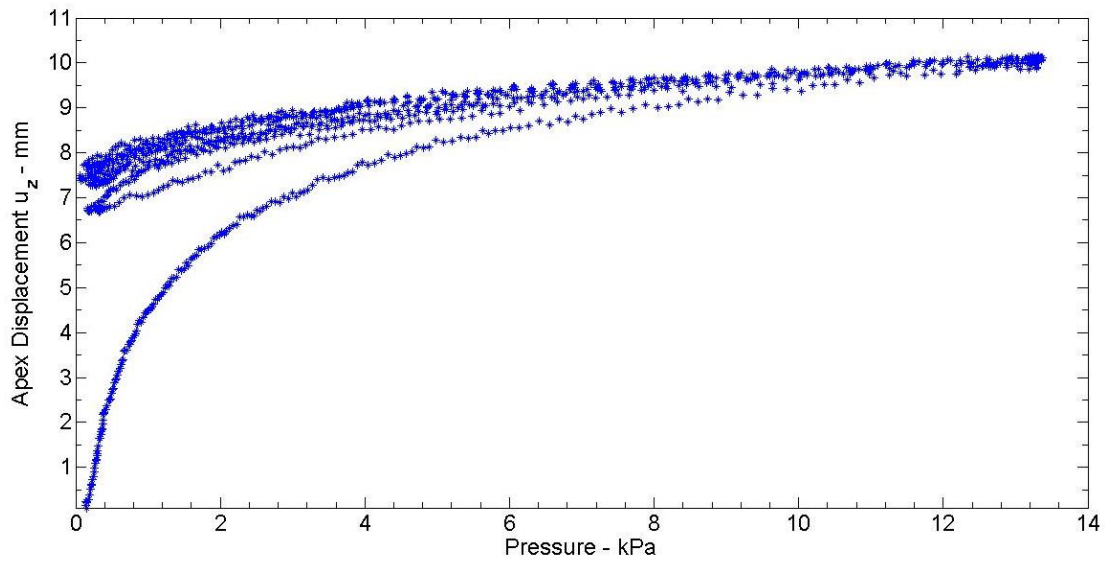


Figure 3-23: Pressure vs. Apex point displacement for cyclic loading and unloading of 5 cycles to study viscoelastic response.

well. The viscoelastic response is simply documented here, and no quantitative models have been pursued.

3.6 FINITE ELASTICITY

It is well known in bio-solid mechanics that the soft biological materials such as skin, arteries, etc. undergo large rotations and strains when deformed under a load and hence we employ the theory of finite elasticity as opposed to infinitesimal strain theory. In solving any boundary value problem numerically or analytically, the following relations need to be considered:

Kinematics: Describes the motion of the material points and relates the undeformed configuration to the deformed configuration by means of strain tensors. This gives a purely geometric description and relates displacement gradients to strain tensors.

Equilibrium: The three conservation laws must be satisfied leading to the equilibrium equations: conservation of mass, conservation of linear momentum, and conservation of angular momentum.

Boundary conditions: Any prescribed displacements or loads must be taken into consideration. The boundary conditions are problem specific.

Constitutive equation: Provides the relation between the stress and the strain tensors by taking into account the material properties of the material involved. This defines the response of individual materials under deformation.

Detailed descriptions of the Theory of Finite Elasticity are widely published and only a brief review relevant to the current work is given here. For more details, please refer [Malvern 1969; Spencer 1980; Lai, 2009]

3.6.1 Kinematics

A material or body $B = \{P_k\}$ is made of a set of material points called particles P_k . As a material undergoes deformation, the vector position of the particles in the body undergoes a change with respect to a fixed origin O and orthonormal basis vector e_i . In a rectangular Cartesian coordinate system $i, j \xrightarrow{\text{varies}} 1..3$. The origin and the orthonormal basis vector together form a reference frame $\psi = \{O; e_i\}$. The motion of any particle P relative to ψ is described as $x(P, t)$ at any another time instant t . Note that t is used to indicate sequential changes in the position, and not to consider inertial effects. Similarly, the position vector of the same particle in its initial position relative to ψ is given as $X(P)$. The relative motion of the particle P in ψ is described by $x = \chi(X, t)$. We can thus have a complete description of the deformation of all the particles and thus the body itself. Figure 3-24 describes the motion of one particle P and a line segment of length dX from the reference frame.

Considering that at each instant t , x is a continuous, differentiable function of X and assuming that the relation between x and X given by χ is uniquely invertible for all values of t , we have the deformation gradient (F) given for the particle motion by

$$\mathbf{F} = \frac{\partial \mathbf{x}}{\partial \mathbf{X}} = \mathbf{grad} \mathbf{x} \quad (3-1)$$

The deformation gradient tensor transforms the element dX from the reference frame configuration into the element dx in the deformed configuration as shown in Figure 3-24. So we have $dx = FdX$. Using a rectangular Cartesian reference system, we can represent the components of x as x_i and X as X_j . Therefore the deformation gradient tensor is given by $F_{ij} = \frac{\partial x_i}{\partial X_j}$

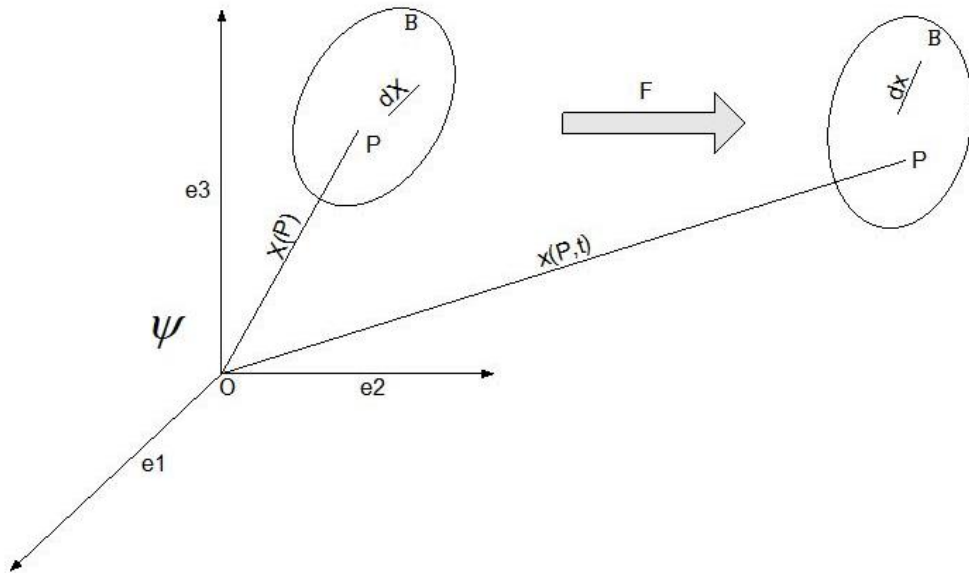


Figure 3-24: Motion of a particle P and line segment from the reference configuration to the deformed configuration.

Although the deformation gradient tensor is used to quantify deformation, it is not a suitable measure of strain because it includes rigid body deformation as well. Strain, by definition is a measure of ratio of change in length to the original length of any segment dx . In order to eliminate the rigid body transformations from F we define another deformation tensor called the right Cauchy-Green deformation (C) tensor.

$$C = F^T F \quad (3-2)$$

The deformation gradient tensor F can be decomposed into two components, namely a rigid body rotation component (R) and a pure stretch (U) component, by means of polar decomposition. Since we are interested in the pure stretch component, having another deformation tensor measure like the right Cauchy-Green is helpful which eliminates the rigid body component in F by means of tensor operations.

$$F = R U \quad (3-3)$$

$$C = F^T F = (R U)^T R U = U^T R^T R U = U^T U = U^2 \quad (3-4)$$

Invariants are scalar combinations of the components of a tensor which remains unaffected during coordinate transformations. The three principal invariants of C in terms of principal values of U denoted as $(\lambda_1, \lambda_2, \lambda_3)$ can be obtained as follows:

$$I_1 = \mathbf{tr}C = \lambda_1^2 + \lambda_2^2 + \lambda_3^2 \quad (3-5)$$

$$I_2 = \frac{1}{2}[(\mathbf{tr}C)^2 - \mathbf{tr}(C^2)] = \lambda_1^2\lambda_2^2 + \lambda_2^2\lambda_3^2 + \lambda_3^2\lambda_1^2 \quad (3-6)$$

$$I_3 = \mathbf{det}(C) = \lambda_1^2\lambda_2^2\lambda_3^2 \quad (3-7)$$

Another useful representation of strain is the Green-Lagrange strain tensor (E) defined below, which returns a zero tensor when there is no deformation. Like the Cauchy-Green deformation tensor, this tensor is also independent of rigid body transformations

$$E = \frac{1}{2}(C - I) \quad (3-8)$$

where C is the right Cauchy-Green tensor and I is the identity tensor. The stretch can be calculated from the Green-Lagrange strain tensor (E).

$$\lambda = \sqrt{2E + \mathbf{1}} \quad (3-9)$$

3.6.2 Stress equilibrium

The equilibrium equations are derived from the three conservation laws and have to be satisfied at all points in the body.

1. Conservation of mass requires that mass of the body be same in initial and final configuration. This results in a relationship between 2 state (reference and deformed) mass densities given by $\rho_0 = J\rho$, where $J = \mathbf{det}(F)$. Here we consider skin tissue as an incompressible material and hence $J = 1$ which gives $\rho_0 = \rho$.
2. Conservation of linear momentum requires that rate of change in linear momentum must balance all external forces (body and surface) acting on the body or material.

Using Gauss' divergence theorem, we arrive at the stress equilibrium equations also called Cauchy's first law for static problem as given below

$$\nabla \sigma_{ij,i} + \rho b_j = 0 \quad (3-10)$$

where σ_{ij} is the Cauchy-stress tensor, defined as the force measured per unit deformed area acting on a surface of the deformed configuration and b_j is the body force component.

3. Conservation of angular momentum requires that rate of change in angular momentum must balance all external moments acting on the body or material. Again using Cauchy traction-stress relations and Gauss divergence theorem, we have a symmetric stress tensor:

$$\sigma_{ij} = \sigma_{ji} \quad (3-11)$$

3.6.3 Boundary conditions

The equilibrium equations are usually posed with one or a mixture of the following general boundary conditions:

1. Displacement boundary conditions – Here a value is prescribed for displacements on the boundary of the body.
2. Traction boundary conditions – Here tractions are prescribed on the boundary of the body.

In the context of this work, we have used a mixed boundary condition, which is a combination of prescribing displacements and traction on different parts of the boundary. Here, a zero displacement boundary condition is prescribed at the edges of the specimen and a uniform pressure boundary condition is applied on the bottom surface of the specimen.

3.6.4 Constitutive equations

After the stress equilibrium and kinematic formulations, a mathematical relationship establishing the relation between stress and strain tensors has to be introduced to complete the boundary value problem. This relationship is given by constitutive equations. The form of constitutive relation is not universal; hence, many material specific or phenomenological models have been proposed. A quick description of different type of materials is given in Table 3-3.

Table 3-3: Material description and it's response to load

Material	Material's characteristic response
Isotropic	Independent of the direction of loading
Transversely Isotropic	Has a single preferred direction due to orientation of fibers
Orthotropic	Is different in each of three mutually orthogonal directions
Homogeneous	Is independent of the position within the body
Heterogeneous	Depends on the position within the body
Incompressible	Volume is preserved and is the usual assumption for soft biological tissues. Enforced using a kinematic constraint that is independent of the load applied.

The strain energy density form of a two-parameter Mooney-Rivlin model is used in the current work to characterize the gross behavior of rubber and soft materials like the porcine skin specimens. A two-parameter Mooney-Rivlin material model is given by Eq.3-12, where W is the strain energy density function and I_i are the invariants of the Cauchy-Green tensor.

$$W = C_{01}(I_1 - 3) + C_{10}(I_2 - 3) \quad (3- 12)$$

The two unknown parameters of Mooney-Rivlin model are determined in this work by means of a numerical-experimental optimization procedure.

3.7 SIMULATIONS IN ABAQUS

Finite Element Method (FEM) is a numerical technique, which provides an approximate solution to a boundary value problem described by a set of differential equations. FEM is employed to determine the unknown displacement field which satisfies virtual work equations when subjected to certain boundary conditions. The principal idea of FEM is to partition a continuous domain of the solid into a finite number of simpler elements. Each element is defined by a set of points, termed nodes and interpolation function, called shape functions. The boundary value problem involved here is non-linear, because the material, namely rubber and porcine skin is expected to undergo large deformations (rotations, displacements and strains).

The commercial finite element simulation software ABAQUS, was used to implement the deformation behavior of the specimen in the bulge test. The specimen geometry - 3D solid deformable, circular geometry of radius 28.57 mm, and a depth of 1.5 mm (for porcine skin) and 3.0 mm for rubber sheet specimen was created in ABAQUS CAE. The geometry was partitioned at the center. The geometry was then meshed using a standard linear 3D hexahedral stress element (C3D8IH- continuum 3-D, 8 node linear brick Hybrid Incompatible modes) available in the element library of ABAQUS, with a seed size of 1 to give a total of 6408 elements and 9885 nodes in all for porcine skin specimen. A finer mesh of seed size 0.5 did not make any significant difference in displacement measures for the applied load. However, the time involved in completing the job for a smaller seed mesh size (0.5) was at least 15 times the time

involved for a normal seed mesh size (1.0). The meshed geometric model is shown in Figure 3-25.

A hyper elastic, isotropic, incompressible two-parameter Mooney-Rivlin material model was assumed for the entire geometry initially. The constitutive equation describing the material model is given in equation 3-11 in the previous section. The initial values for the two unknown parameters were taken from the literature. After meshing, two load steps were created to apply the load and the boundary conditions for the boundary value problem. A fixed boundary condition was applied for all the edge nodes of the 3D solid, by fixing all degrees of freedom (translations and rotations) for these nodes. A uniform pressure load was applied in the positive z direction with a maximum magnitude of 13 kPa in the ramp linear amplitude mode. The pressure was applied linearly for a total time period of 1 second with an increment step size of 0.02 seconds. Due to the large

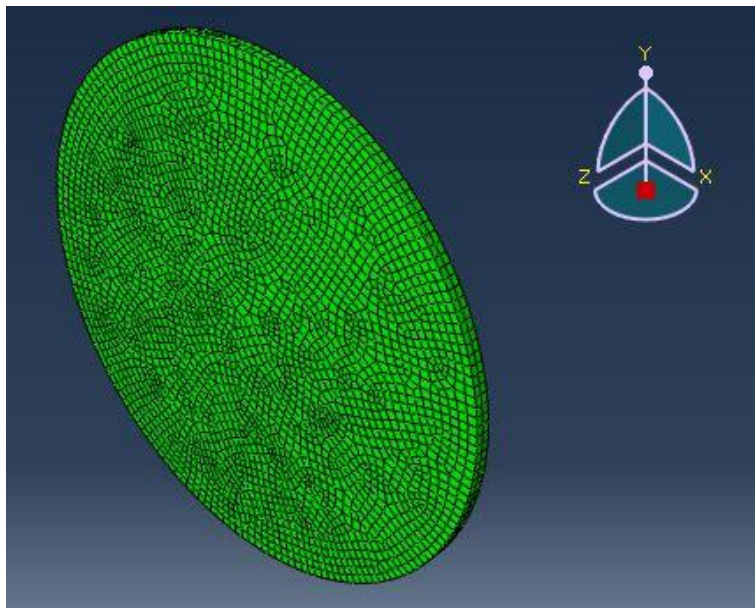


Figure 3-25: Meshed geometry with an eight node linear brick element

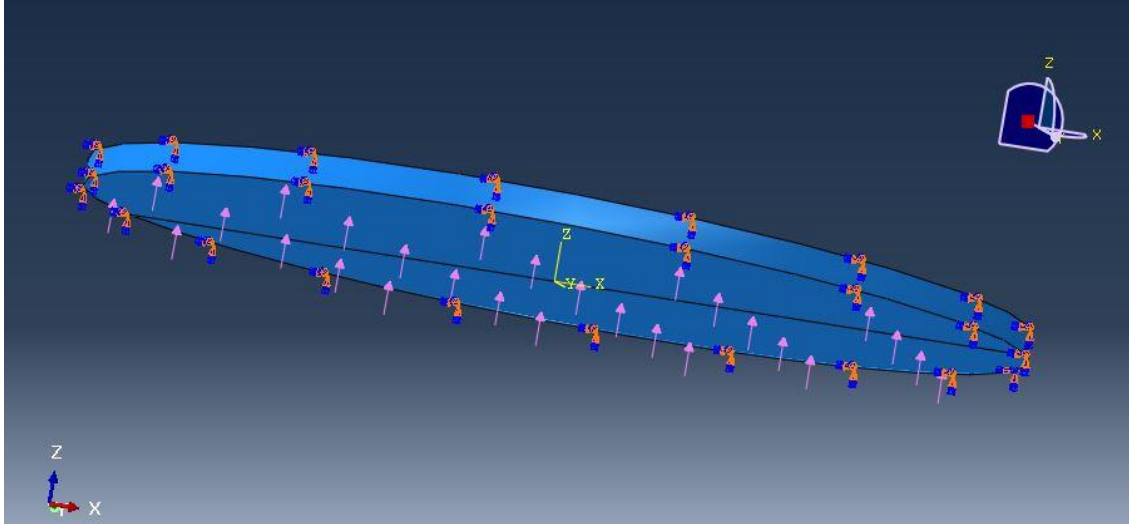


Figure 3-26: Load and boundary conditions applied on the geometry

deformations expected for soft biological materials like skin, the NIgeom parameter was set to ‘ON’ in ABAQUS, which intrinsically accounts for the non-linear geometry of our model. A direct equation solver and Full Newton solution technique was used in this analysis. Figure 3-26 shows the boundary conditions and the direction of the load applied in this analysis.

3.8 NUMERICAL RESULTS

The optimization problem defined here is to find those values for the two unknown parameters (C_{01}, C_{10}) of the Mooney-rivlin model that minimizes the displacement difference between the experimental and simulated model at different pressure values. The objective function is given by

$$\mathit{Min}(\sum_{p=1}^m \sum_{i=1}^n (\mathit{Displ}_{i_exp} - \mathit{Displ}_{i_sim}; C_{01}, C_{10})^2) \quad (3-13)$$

where i is the i^{th} point on the specimen for a particular pressure and p is the pressure value that ranges from 0 to 13 kPa. In the current work, we have taken 3 pressure values

(3.25 kPa, 6.5 kPa and 13 kPa) and minimized the displacement difference between the experiment and numerical displacements for all points on the bulge. The value for the two parameters were obtained by means of trial and error here rather than using a minimization procedure as the absolute difference between simulated and experimental displacement values ranged between 0 to 4.0 mm in all.

3.8.1 Rubber specimen

The apex displacements obtained from the numerical simulation using a Mooney-Rivlin model for rubber (3.0 mm thick) corresponding to the pressure is shown in Figure 3-27. Figure 3-28 shows the displacement contour plots for the points marked in Figure 3-27; note that this is to be compared to the experimental displacement contours shown in Figure 3.7. The simulated displacements were compared with the experimental displacements to find the optimized Mooney-Rivlin material parameters C_{01} and C_{10} . The

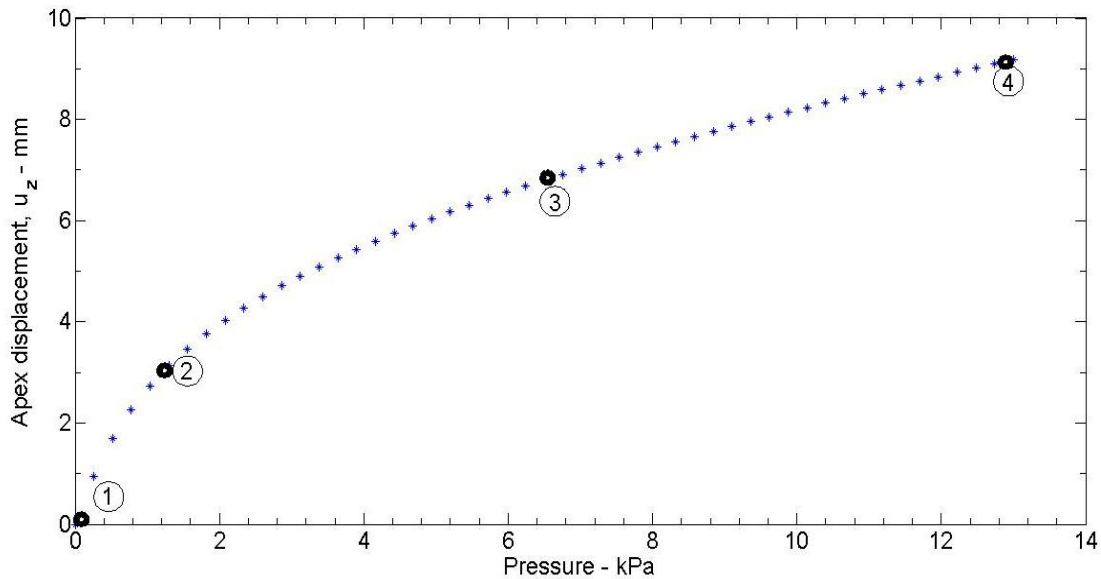


Figure 3-27: Pressure vs. Apex displacement for rubber – 3.0 mm thick (Simulated data)

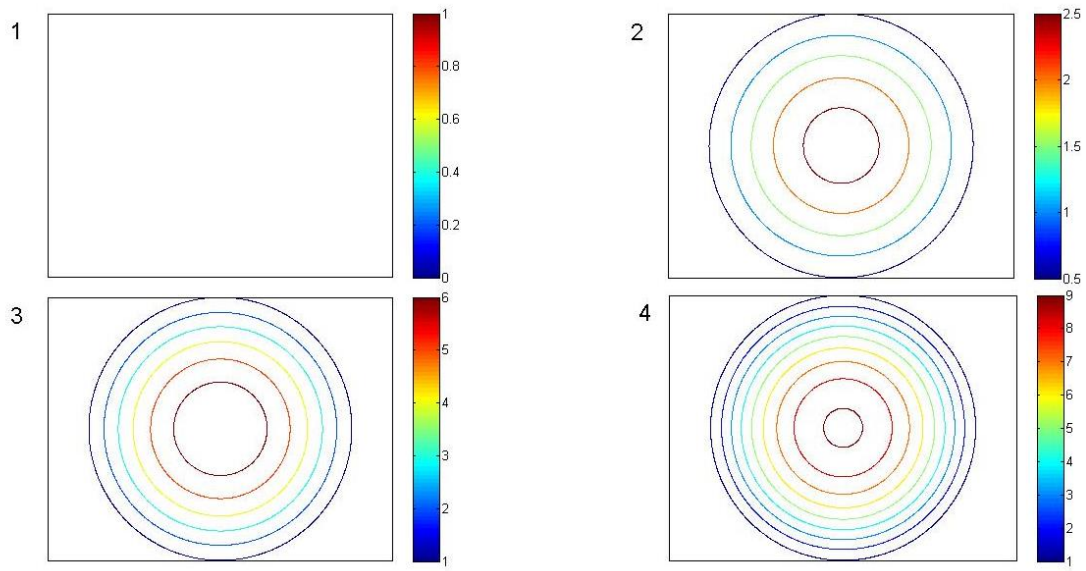


Figure 3-28: Simulated displacement contour plots for pressures corresponding to points 1, 2, 3, and 4 from Figure 3-27

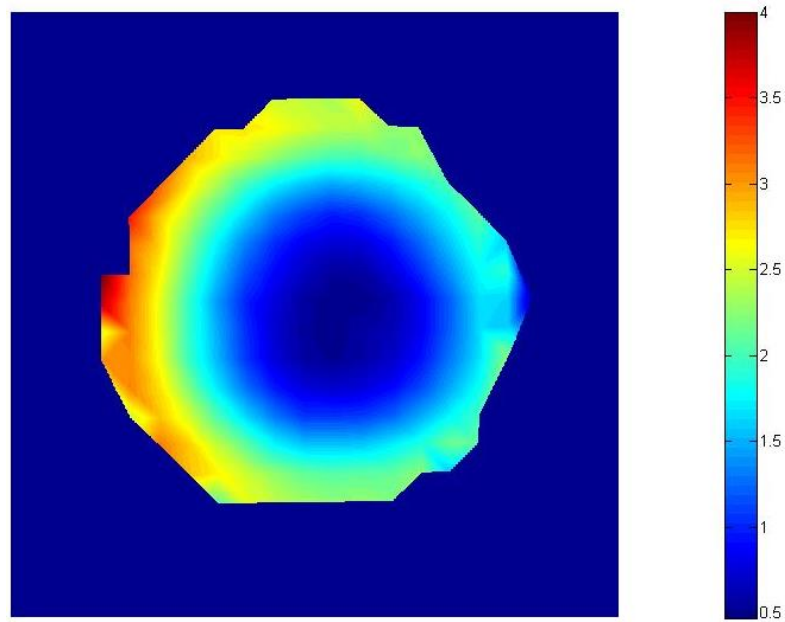


Figure 3-29: Imagesc plot of difference in displacement measures between experimental and simulated points in rubber - 3.0 mm thick

difference in displacement values (in mm) between the experimental and simulation points throughout the membrane specimen (3.0 mm thick) at a tested maximum pressure of 13 kPa is shown in Figure 3-29.

The absolute difference in displacement values between the experimental and simulated points on the rubber specimen (3.0 mm thick) ranges between 0-2.5 mm throughout the membrane; the higher values of 4.0 mm are near the edges of the specimen where the experimental results are not reliable. The optimized material parameters of rubber for the Mooney-Rivlin constitutive model are thus: $C_{01} = 0.14 \text{ MPa}$ and $C_{10} = 0.014 \text{ MPa}$.

The deformed bulge profile of rubber (for a section through the center) is shown in Figure 3-30, in comparison to that predicted using the optimized set of Mooney-Rivlin parameters at 13 kPa. Further refinement of the material properties could be achieved, but was not pursued.

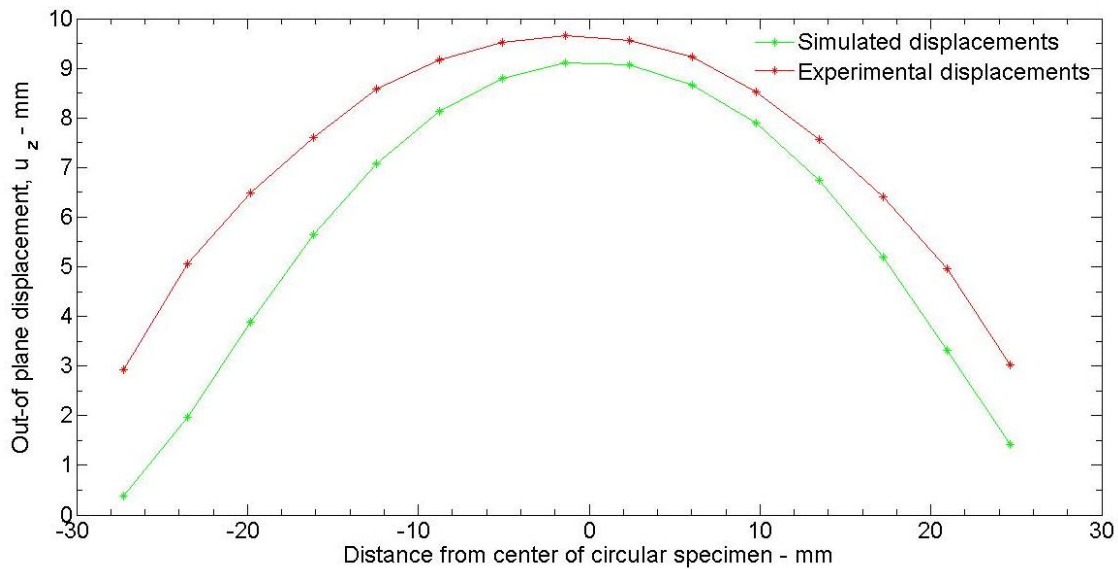


Figure 3-30: Comparison of displacements from experiment and simulations for a section through the center at a maximum pressure of 13 kPa in rubber - 3.0 mm thick

3.8.2 Porcine skin

The simulated displacements were compared with the experimental displacements to find the optimized Mooney-Rivlin material parameters C_{01} and C_{10} for porcine skin. We note that this ignores the anisotropy indicated by the experimental measurements. The absolute difference in displacement values (in mm) between the experimental and simulation points throughout the membrane specimen at three pressures ranged from 0-2.5 mm. The deformed bulge profile of porcine skin (at a section through the center) is shown in Figure 3-31, in comparison to that predicted through an optimized set of Mooney-Rivlin material models at different pressure values (3.25 kPa, 6.5 kPa and 13.0 kPa). The optimized material parameters thus obtained for the Mooney-Rivlin constitutive model were: $C_{01} = 0.207 \text{ MPa}$ and $C_{10} = 0.0389 \text{ MPa}$ for porcine skin.

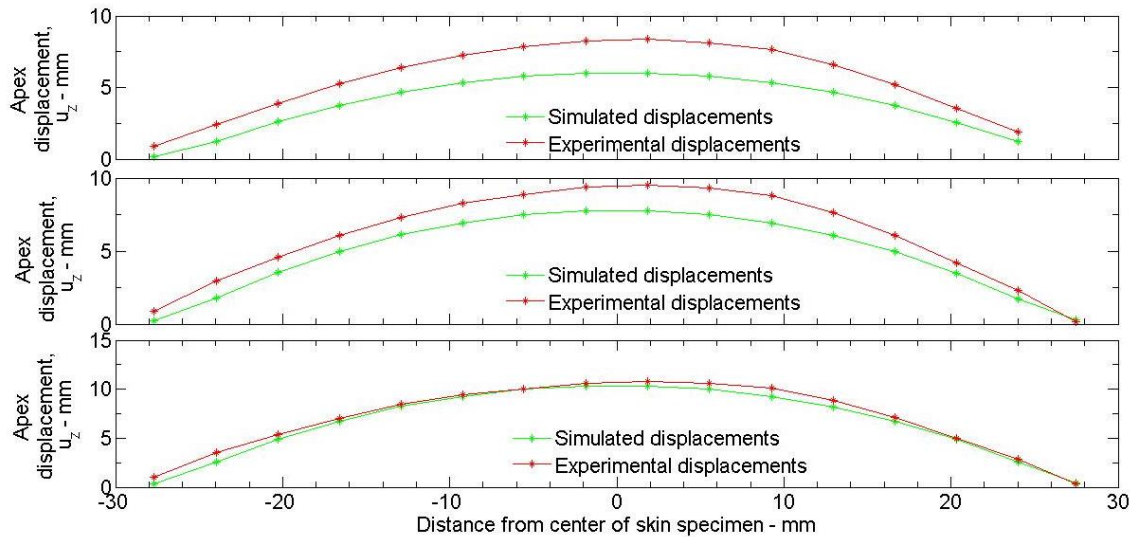


Figure 3-31: Experiment and simulated displacement comparison through a center section for values of Pressure = 3.25 kPa, Pressure = 6.50 kPa and Pressure = 13.0 kPa

However, when we plotted the stress-stretch curve using these Mooney-Rivlin parameters obtained for porcine skin, we found that this model stiffens only at large

stretches (λ), i.e, $\lambda \geq 2$ or 3. However, skin tissue in general is known to exhibit a stiffening response at stretches beyond 1.1 to 1.2 experimentally, evident from our results on porcine skin (Figures 3-16, 3-19, and 3-20) and from human skin experiments reported in the literature [Tonge et al., 2013].

Therefore, we considered anisotropic constitutive models for simulating the porcine skin behavior and calibrating appropriate material parameters that mimic the experimental pressure-displacement curves and strains reasonably.

We simulated the bulge test using the anisotropic Gasser-Ogden-Holzapfel (GOH) model, an internal material model present in ABAQUS. GOH model is applicable to any incompressible solid with two oriented fiber directions in general. The constitutive stress-stretch relation of this model is devised accounting for the orientation and distribution of the fiber families. A complete description of this model (both 2D and 3D) is given elsewhere [Holzapfel et al., 2000; Gasser et al., 2006; Tonge et al., 2013]. The stress-stretch relation for the 3D (transverse isotropic) GOH model obtained from the strain energy density function is given by equations 3-14 and 3-15 [Tonge et al., 2013]. The stress-stretch relation for the 2D (planar fiber distribution) GOH model obtained from the strain energy density function is given by equations 3-16 and 3-17 [Tonge et al., 2013].

$$\begin{aligned} \sigma_f(\lambda_f, \lambda_p) = & (\mu + 2k_1\kappa(I_\alpha - 1) \exp[k_2(I_\alpha - 1)^2]) \left(\lambda_f^2 - \frac{1}{(\lambda_f\lambda_p)^2} \right) \\ & + 2k_1(1 - 3\kappa)(I_\alpha - 1) \exp[k_2(I_\alpha - 1)^2] \lambda_f^2 \end{aligned} \quad (3-14)$$

$$\sigma_p(\lambda_f, \lambda_p) = (\mu + 2k_1\kappa(I_\alpha - 1) \exp[k_2(I_\alpha - 1)^2]) \left(\lambda_p^2 - \frac{1}{(\lambda_f\lambda_p)^2} \right) \quad (3-15)$$

$$\sigma_f(\lambda_f, \lambda_p) = \mu \left(\lambda_f^2 - \frac{1}{(\lambda_f\lambda_p)^2} \right) + 2k_1(1 - \kappa_{2D})(I_\alpha - 1) \exp[k_2(I_\alpha - 1)^2] \lambda_f^2 \quad (3-16)$$

$$\sigma_p(\lambda_f, \lambda_p) = \mu \left(\lambda_p^2 - \frac{1}{(\lambda_f \lambda_p)^2} \right) + 2k_1 \kappa_{2D} (I_\alpha - 1) \exp[k_2 (I_\alpha - 1)^2] \lambda_p^2 \quad (3-17)$$

where σ_f, λ_f are the stress and stretch in fiber direction, σ_p, λ_p are the stress and stretch in perpendicular direction, μ is the shear modulus term to consider the effect of the matrix (ground matrix on which the fibers are arranged), k_1 and k_2 are the 3D fiber parameters describing the stiffening response, κ_{2D} is the 2D dispersion parameter and κ is the 3D dispersion parameter, both dispersion parameters describe the contributions of the isotropic and anisotropic distribution of the fibers, I_α is a pseudo-invariant of the resultant tensor evaluation of Cauchy-Green strain tensor (C) and a generalized structure tensor (A) evaluating to $\kappa I_1 + (1 - 3\kappa)\lambda_f^2$ for 3D and $\kappa_{2D} \lambda_p^2 + (1 - \kappa_{2D})\lambda_f^2$ for 2D.

The unknown material parameter values in these models are $\mu, \kappa/\kappa_{2D}, k_1$ and k_2 . These parameters have a large variation amongst different subjects as reported in Table 3-4 [Tonge et al., 2013]. For example, Sample 83/M differs greatly in the μ and k_2 values from that of Sample 43/M. This is due to the fiber alignment and dispersion being different amongst the specimens. The large differences in parameter values will result in different stress-stretch curve using the same 2D GOH model.

We used the average GOH 2D parameter values for the bulge test simulations calibrated from that of Tonge et al. However, using these parameter values in the GOH model, the apex displacement (21.74 mm) at a pressure of 5 kPa was well above that of the experimental apex displacement of 10.9 mm at the maximum pressure of 13 kPa. Considering that the Mooney-Rivlin parameters (C_{01}, C_{10}) calibrated above attained the necessary peak displacement at the apex point similar to that in the experiment, we used the C_{01} value for the shear modulus parameter (μ) of the 2D GOH model, keeping all

other fiber parameters the same as the average values from Tonge et al. This model will be referred further as ‘2D GOH model with C_{01} ’.

Table 3-4: Material parameters: 2D GOH model [Reproduced from Tonge et al., 2013]

Sample	μ (kPa)	κ_{2D}	k_1 (kPa)	k_2
43/M	6.804	0.107	3.766	30.739
44/M	5.648	0.195	0.040	39.131
59/M	4.773	0.271	0.281	45.959
61/M	8.262	0.369	0.221	120.852
62/F	6.286	0.467	0.006	18.845
83/M	22.634	0.540	4.636	200.967
Average	9.068	0.325	1.446	76.082
Std Dev.	6.748	0.165	2.040	71.001

The pressure displacement curve for the apex point thus obtained is shown in Figure 3-32. The apex displacement reached for a maximum pressure of 13 kPa using the 2D GOH model with C_{01} was 11.6 mm, which is close to the experimental apex displacement of 10.9 mm (at 13 kPa). Figure 3-33 and Figure 3-34 shows the displacement contours and the bulge profile at pressure values corresponding to points marked in Figure 3-32. The major and minor strain contours at pressure values corresponding to points marked in Figure 3-32 are shown in Figures 3-35 and 3-36. The major and minor strain profile at the maximum pressure of 13 kPa for a 2D GOH model with C_{01} is shown in Figure 3-37 and Figure 3-38.

Figure 3-39 shows the contour plots of the difference in displacement at four different pressure points shown in Figure 3-32 and Figure 3-16. The displacement

difference range from 0 – 2 mm overall at any pressure value and the strain values obtained from the simulation and that of the experiment are almost in the same range (11-13%). Even though we have not reached very high strain levels, we believe we have reached a strain range that is enough to see the effect of the fibers in action.

In conclusion, ‘2D GOH with C_{01} ’ gives a reasonably good prediction for both displacements and strains. The stiffening effect observed in skin at about stretch values of 1.05 to 1.2 is also accounted for by using the 2D GOH with C_{01} model.

We also simulated the bulge tests using GOH models parameterized with other material calibration values from Tonge et al. [Part 2, 2013]. Figure 3-40 is a plot showing the pressure vs. apex displacement variation for all the simulated models in comparison to the experimental results for porcine skin. At the maximum pressure of 13 kPa and a very low pressure of 0.5 to 1 kPa, both the 2D GOH with C_{01} model and 3D GOH model fit reasonably well our experimental results. We can also conclude that both Mooney-Rivlin and 2D GOH models work well at larger stretches, while 3D GOH model works well at lower stretches as well; however, a complete optimization procedure over all pressure points needs to be considered to extract the parameter values for these models. Table 3-5 shows the material parameters used for the different models shown used here in this thesis.

Table 3-5: Material parameters used for the simulations

Model	C_{01} (kPa)	C_{10} (kPa)	μ (kPa)	κ/κ_{2D}	k_1 (kPa)	k_2
Mooney-Rivlin	207	38.9	-	-	-	-
2D GOH with C_{01}	-	-	207	0.325	1.446	76.082
2D GOH 83M	-	-	22.634	0.33	4.636	200.967
3D GOH 83M	-	-	22.634	0.33	2427.7	5984.20

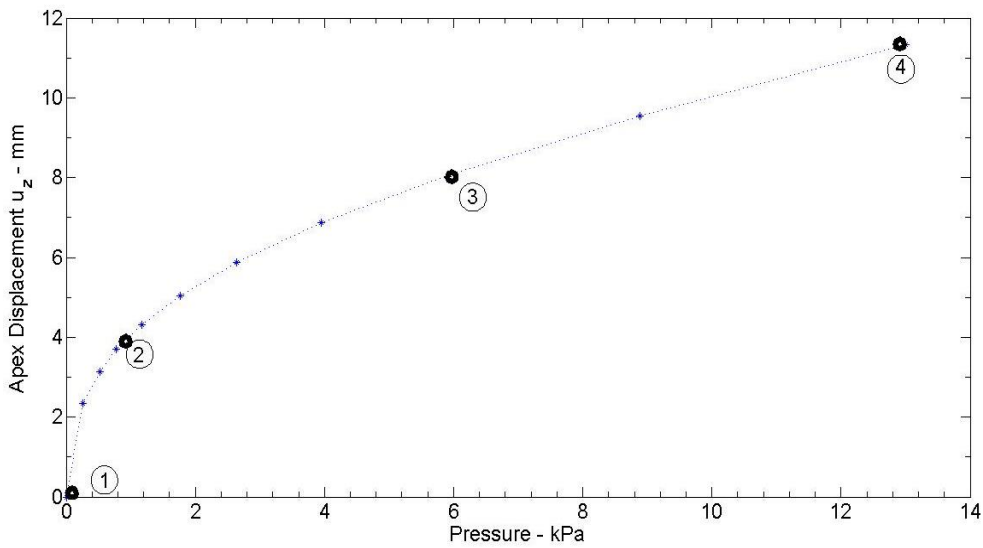


Figure 3-32: Pressure Vs Apex displacement porcine skin using 2D GOH model with C_{01} (Simulated data)

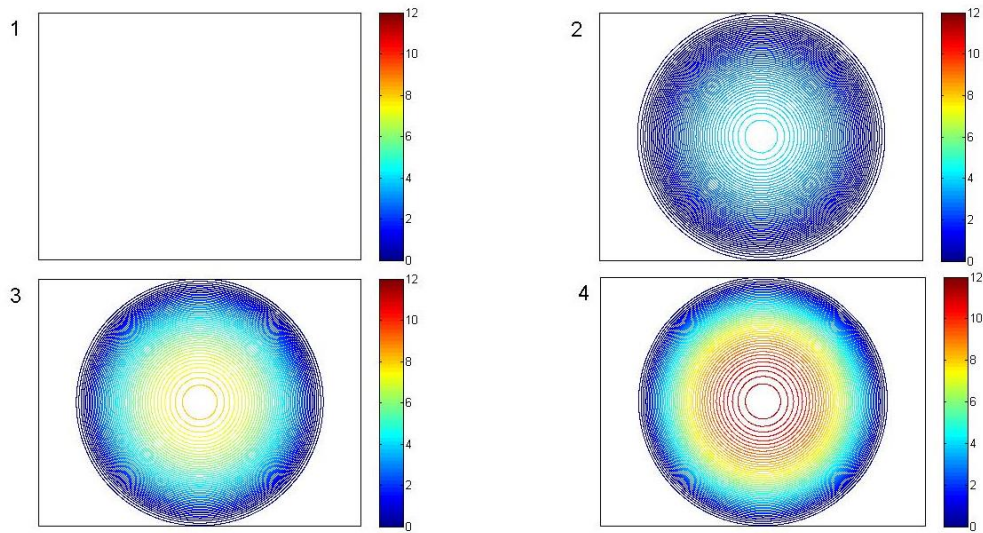


Figure 3-33: Displacement contours using 2D GOH model with C_{01} for points marked in Figure 3-32

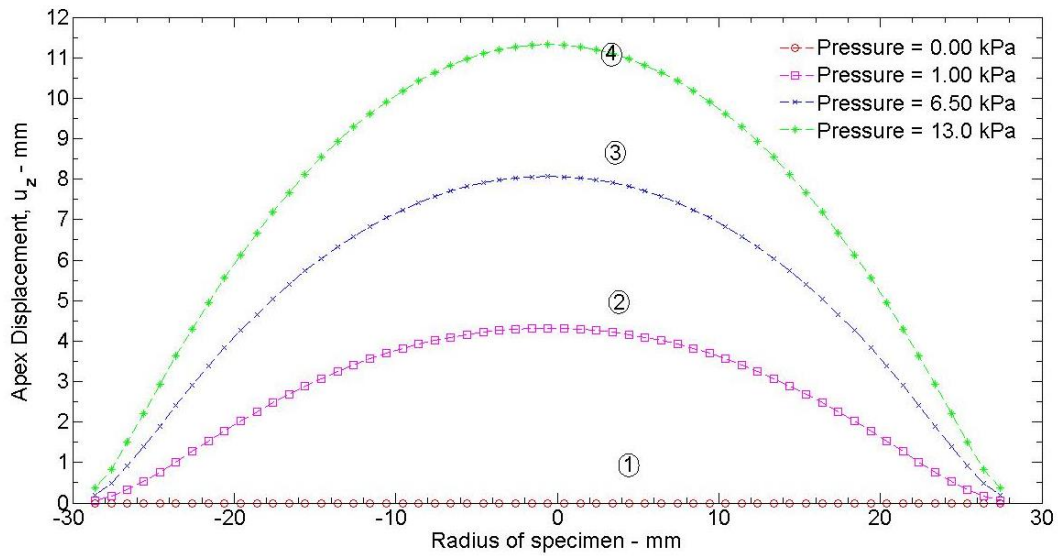


Figure 3-34: Displacement profile using 2D GOH model with C_{01} for points marked in Figure 3-32

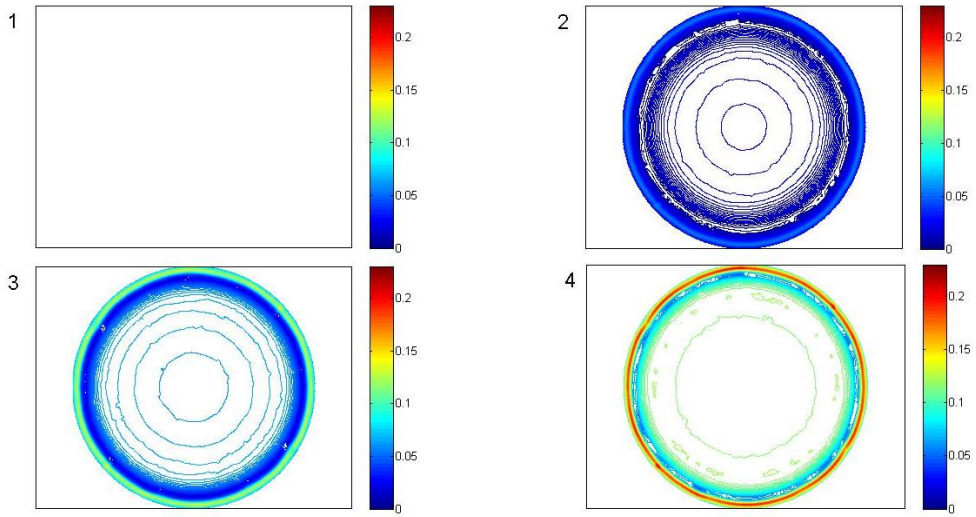


Figure 3-35: Major strain contour plots using 2D GOH model with C_{01} for points marked in Figure 3-32

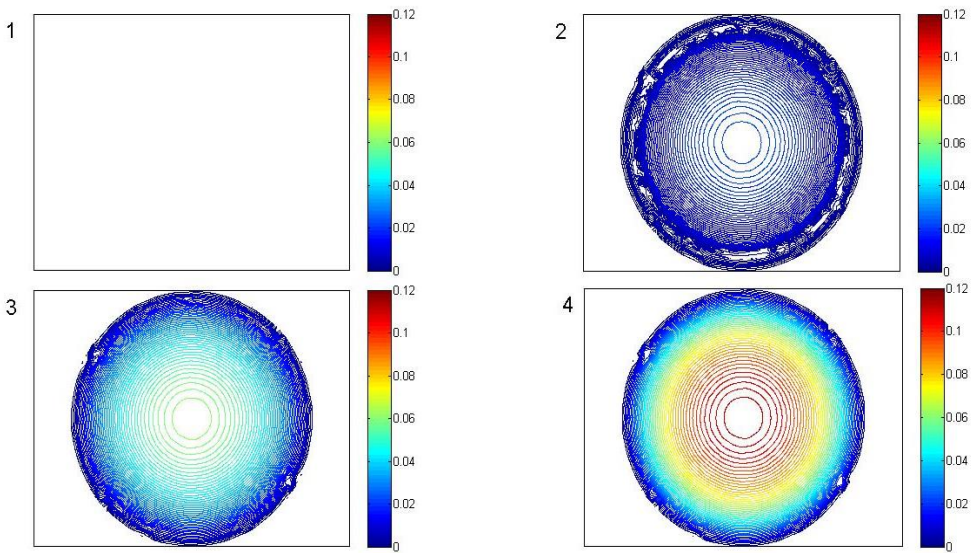


Figure 3-36: Minor strain contour plots using 2D GOH model with C_{01} for points marked in Figure 3-32

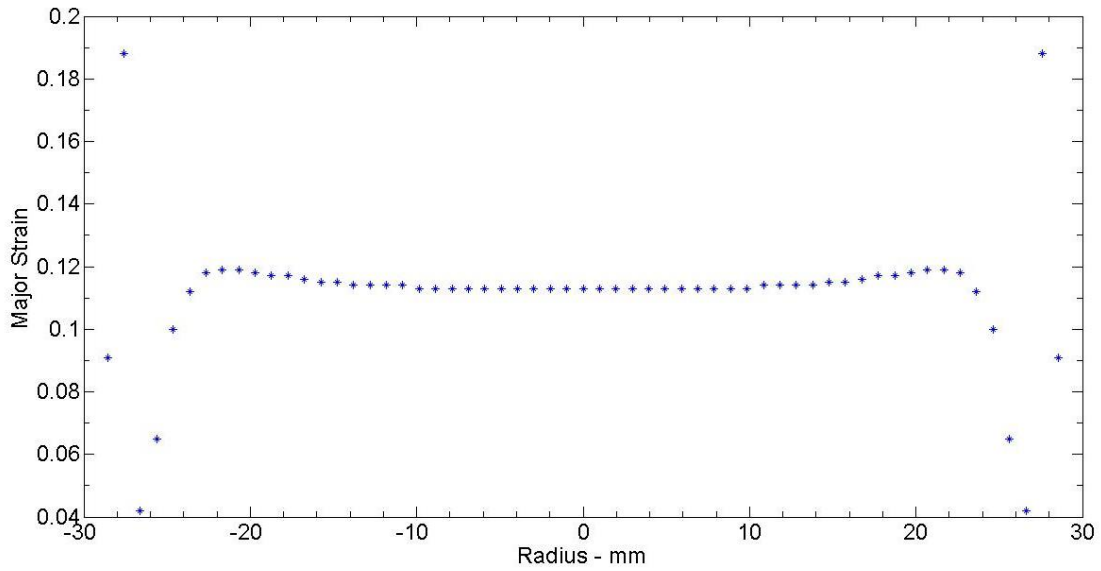


Figure 3-37: Major strain profile at 13 kPa using 2D GOH model with C_{01} for a section taken at the center of the specimen (Simulated data)

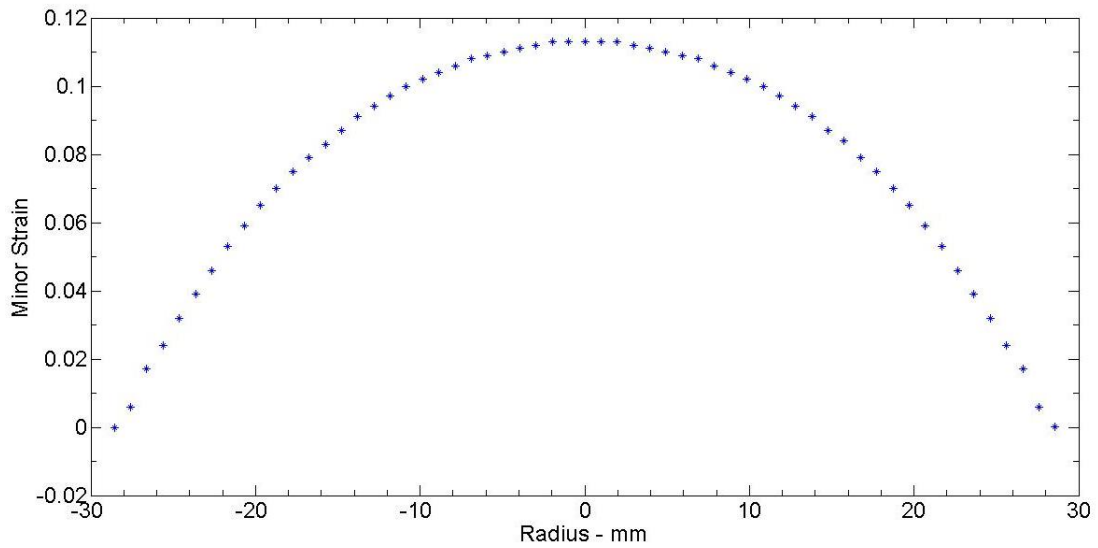


Figure 3-38: Minor strain profile at 13 kPa using 2D GOH model with C_{01} for a section taken at the center of the specimen (Simulation data)

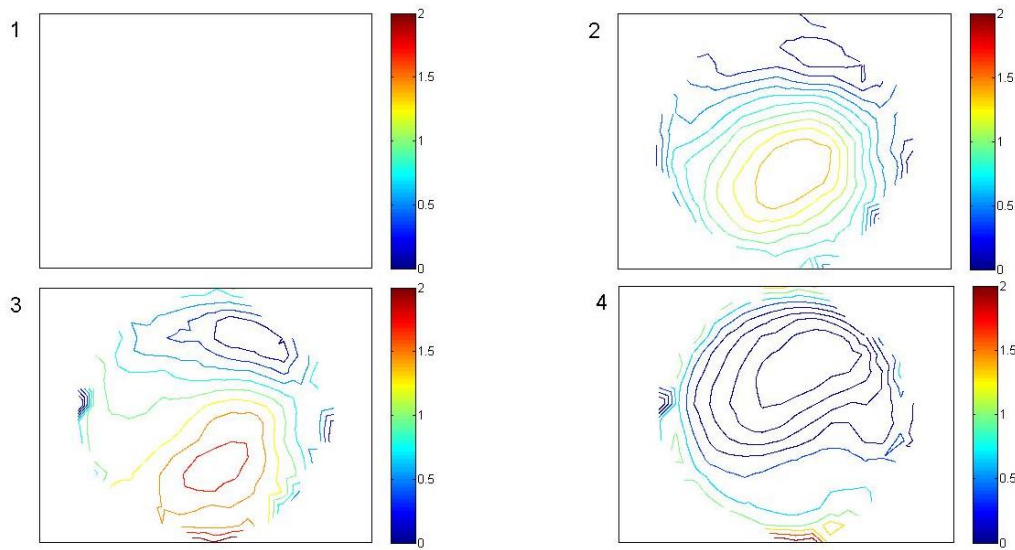


Figure 3-39: Comparison of experimental and simulated displacements for all points at pressure values marked in Figure 3-16

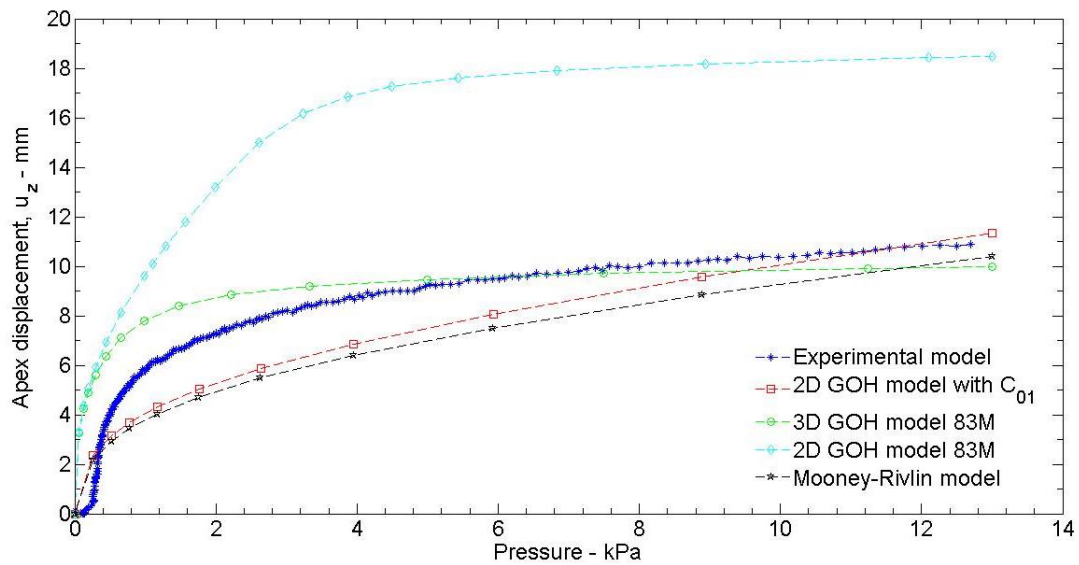


Figure 3-40: Apex displacements Vs Pressure plots for experiment and simulation results on porcine skin

Chapter 4: Conclusions and future work

4.1 CONCLUSIONS

Skin contributes an important role to the total mechanical behavior of any body part. An accurate material model capturing the behavior of normal healthy skin is thus important for many applications such as in computer assisted surgery, to simulate deformations related to different types of incisions and closing techniques, pressure ulcer research and in identifying stabbing mechanisms and burn mechanisms. Therefore, it has to be included in corresponding mathematical models that replicate any physical phenomenon of a complete body part. Unfortunately, accurate mathematical descriptions of skin mechanical behavior still remain a limiting factor to achieve realistic simulation results in the biomedical field.

It is common to use material parameters of skin from cadavers or animal skin in a Breast Biomechanical Model (BBM). Our group's research has found modeling skin in a BBM as an important component to obtain reasonable simulation results, for a physical phenomenon of movement of the breast from an upright to supine position. Thus, the motivation for this work comes from the need to find appropriate material parameters that constitute breast skin to use in a BBM.

The overall goal of this research thus was to develop a suitable test method and to find an optimized set of material parameters to describe the material behavior of an *in vitro* human skin specimen. To that end, we have developed a portable bulge or inflation test device that can be used to test the human skin specimens. A complete set-up of this device with the associated hardware as described in Chapter 3, section 3.2 is shown in Figure 4-1. The working principle of the test device is validated by conducting the inflation tests on rubber and porcine skin specimens. The biaxial bulge tests on rubber

sheets were performed on three different sheet thicknesses: 0.3 mm, 1.5 mm, and 3.0 mm. The testing device that is designed here can also be used to test any planar biological soft tissue such as, human eye, chorioamnion, etc.

The customized bulge test device uses a Digital Image Correlation technique to find the strains and displacements on the specimen during the bulge. A numerical simulation of the bulge test on rubber and porcine specimen was performed using the Finite Element software, Abaqus. The numerically predicted displacements were then compared with the experimentally measured displacements at different points on the specimen for fixed pressure values to arrive at a set of optimized parameters. These



Figure 4-1: Biaxial Bulge Test set-up.

parameters minimized the difference between the experimental and simulated displacements. The difference in displacement values ranged from 0 – 4 mm in all for both rubber and porcine specimens. The optimized material parameters for rubber were found by using a two-parameter Mooney-Rivlin constitutive model. The optimized material parameters for porcine skin were found by using a Gasser-Ogden-Holzapfel model along with Mooney-Rivlin parameters for porcine skin.

The biaxial pressurized bulge tests performed on rubber sheets and porcine skin specimens revealed that there was no specimen failure at least until a pressure of 13 kPa. The maximum displacement reached for a pressure of 13 kPa was 10.8 mm for the porcine specimen. The two principal strains recorded for porcine specimen from the experiments were 12.56% and 9.84%, thus showing slight anisotropy in the specimen. A cyclic load testing on porcine specimen revealed that there is a relaxation of up to 7 mm that was not recovered from the first cycle's loading phase (Figure 3-18).

4.2 LIMITATIONS AND FUTURE WORK

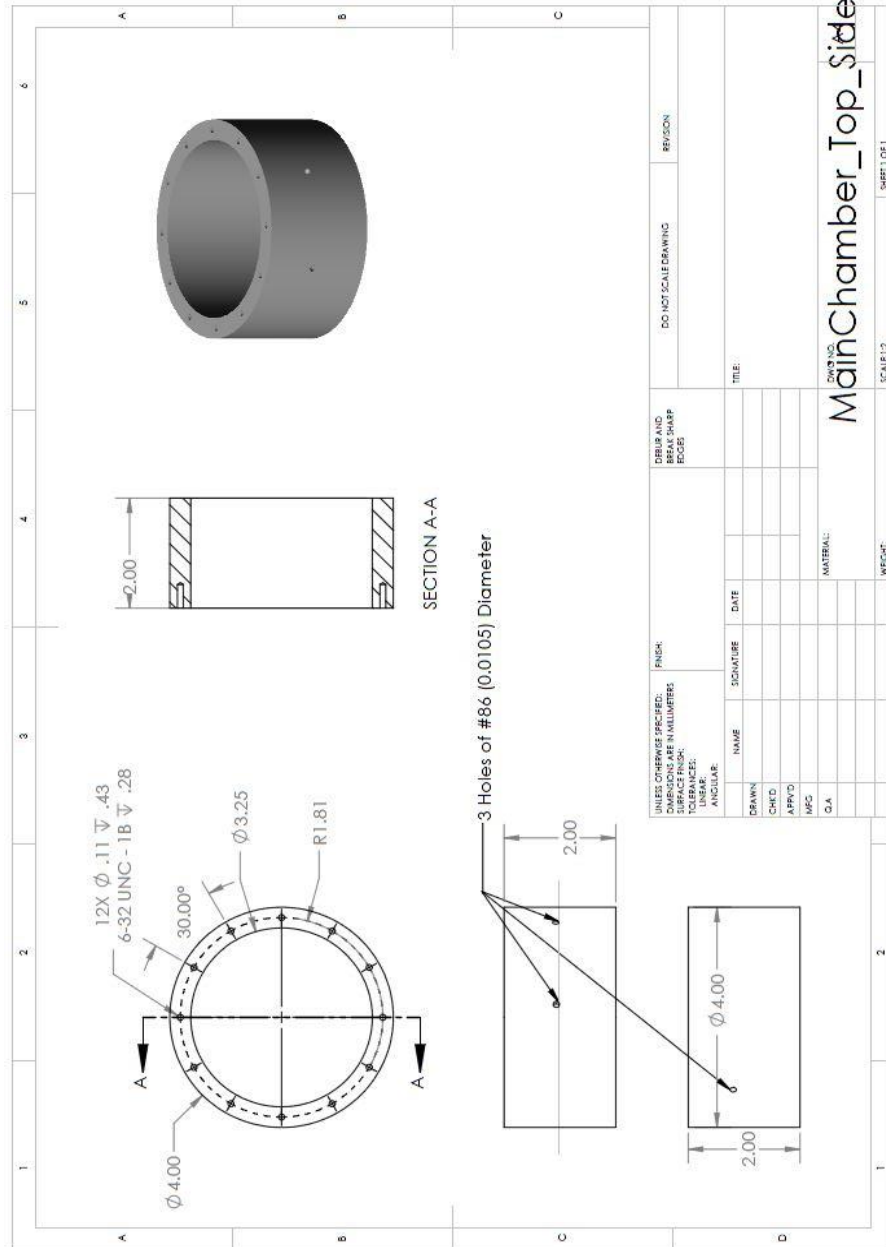
- One of the major limitations of current work is that the inflation tests were performed up to a maximum pressure of 13 kPa only, which corresponds to a maximum principal strain of up to 13% in case of porcine specimen. Even though a 2D GOH with C_{01} model parameters gives reasonable predictions for both displacements and strains, these were arrived at only by minimizing the difference in displacements at few pressure values. Further investigation is needed to find the exact material parameter values by optimizing the difference in displacements over all pressure values.
- A statistical analysis on the material parameter values obtained for different specimens could be explored.

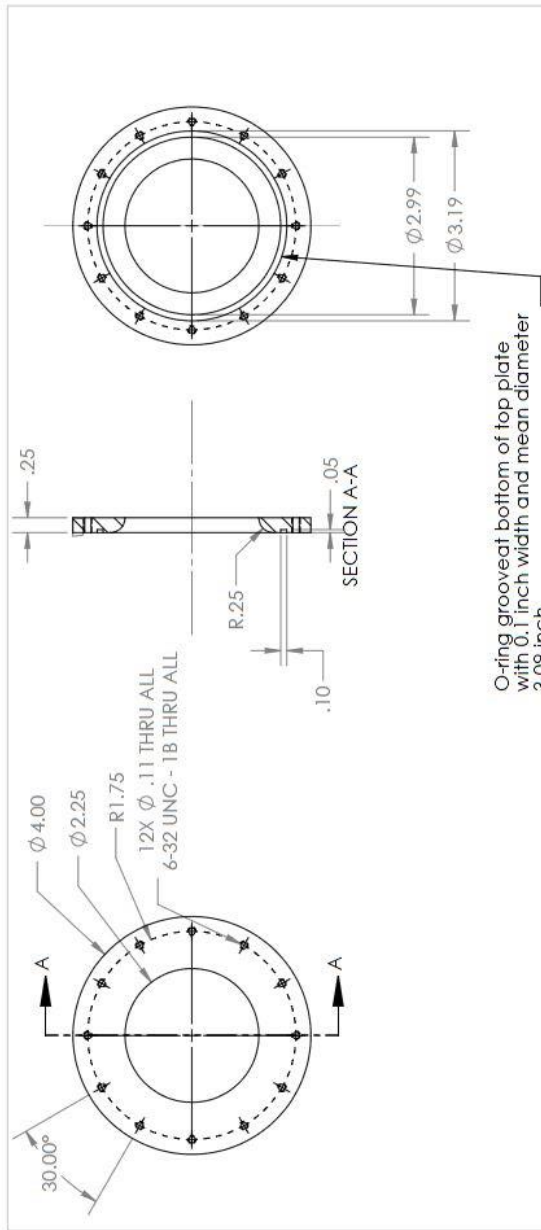
- The current work does not include any histological studies of the skin specimen. Quantification of fibers by means of histological studies could give insight into the physical meaning of the material parameters used in the model. It also will help understand the slight anisotropy observed in case of the porcine skin.
- The complete spectrum of viscoelastic effects was not explored in the current work. A cyclic testing was performed on porcine skin to understand the viscoelastic effects. However, a creep test could be performed with a constant pressure to record the deformation effects on the skin specimen. Stress-relaxation experiments on the skin specimen could also provide us details on the viscoelastic effect of the skin.
- The current work does not investigate the rate-dependent and time-dependent components of the skin tissue behavior.
- The maximum recording potential of the pressure transducer used here was up to 39 kPa and hence exploring a higher pressure might lead to a higher strain percent thus covering a broader region of the stiffening section of the stress-strain curve.
- The FE model developed here to identify the parameters does not account for the sliding effect of the specimen from the bottom of the top plate to the top of the top plate. Future FE models should account for this sliding effect in the simulations by modeling it as a contact problem. Future models of the bulge test need to account for this initial contact boundary condition.
- The residual displacements observed in our viscoelastic studies on porcine skin is not in agreement with the experimental results on human skin

conducted by Tonge et al., [Part-1, 2013], where no residual displacement is observed. The observed residual displacements in our experiments may be because of the specimen relaxation happening during the unloading cycle or due to the effect of the device design used in testing the material for viscoelastic effects or a characteristic of porcine skin in itself. Further careful experiments need to be conducted to study the viscoelastic effects.

Appendix A

Pressurized Bulge test Engineering Drawings

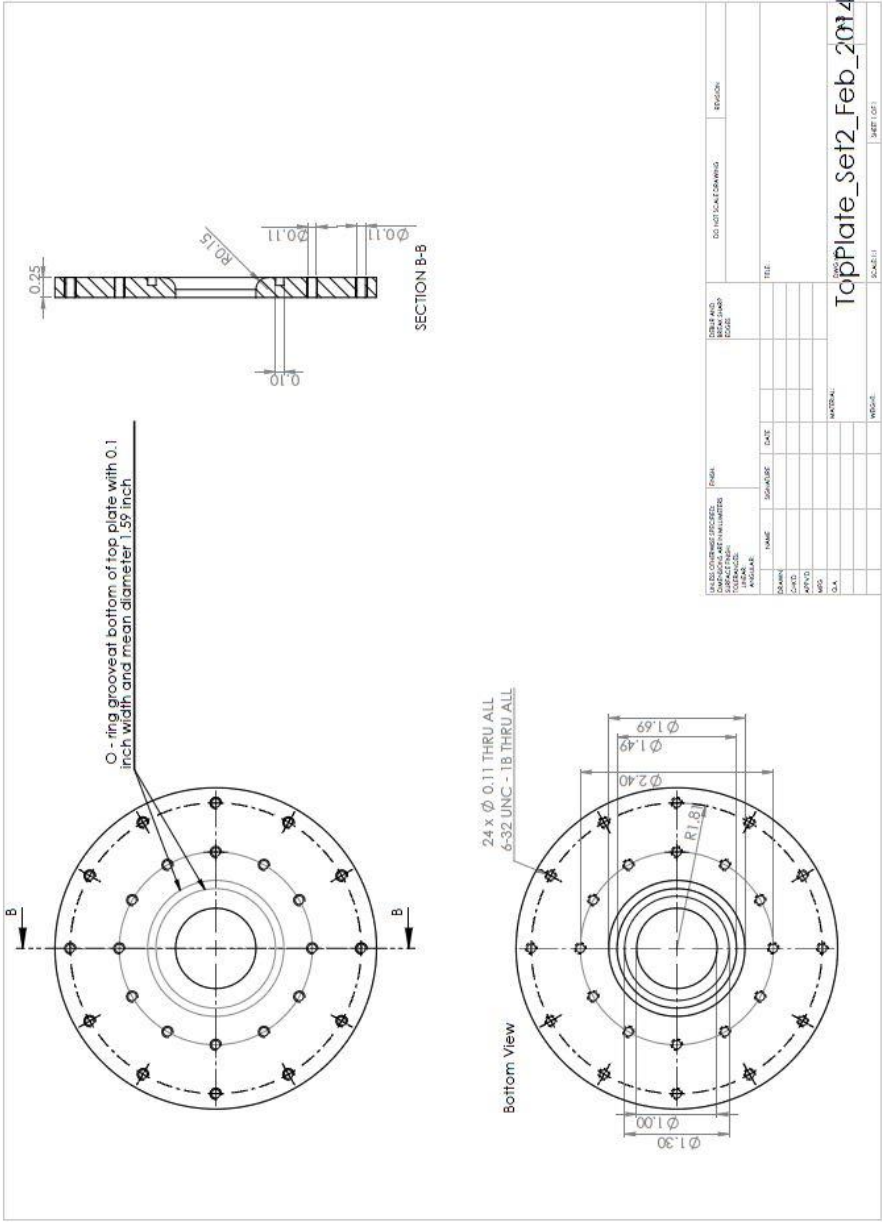


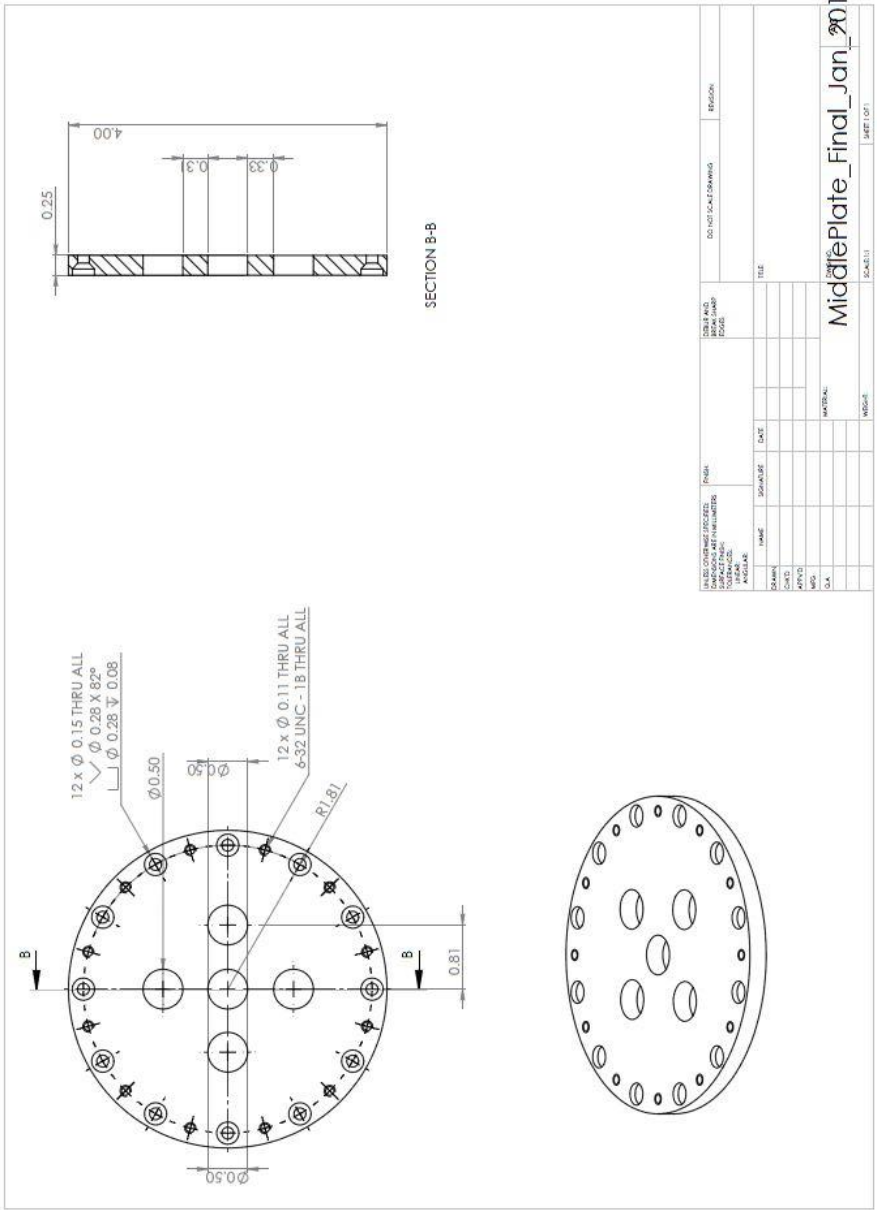


O-ring groove at bottom of top plate with 0.1 inch width and mean diameter 3.09 inch

UNLESS OTHERWISE SPECIFIED: DIMENSIONS ARE IN INCHES TOLERANCES: FRACTIONAL: ± .005 DECIMAL: ± .001 ANGULAR: MACH. ± .01 HOLE POSITION: ± .005 THREE PLACE DECIMAL: ± .001 INTERPRET GEOMETRIC TOLERANCING PER MATERIAL. FINISH:	DRAWN	NAME	DATE
	CHECKED		
	ENG. APPR.		
	MFG. APPR.		
COMMENTS:	G.A.		
DO NOT SCALE DRAWING	SIZE DWG. NO. REV Top Plate Modified May 21		
NEXT ASSY USED ON APPLICATION	SCALE: 1:2 WEIGHT: SHEET 1 OF 1		

PROPRIETARY AND CONFIDENTIAL
 THIS DRAWING IS UNCLASSIFIED
 DATE 10/15/01 BY 60322/UC/LP/STP
 4-NP&E COMPANY NAME HERE, ANY
 REPRODUCTION IN PART OR AS A WHOLE
 WITHOUT THE WRITTEN PERMISSION OF
 4-NP&E COMPANY NAME USED IS
 PROHIBITED.

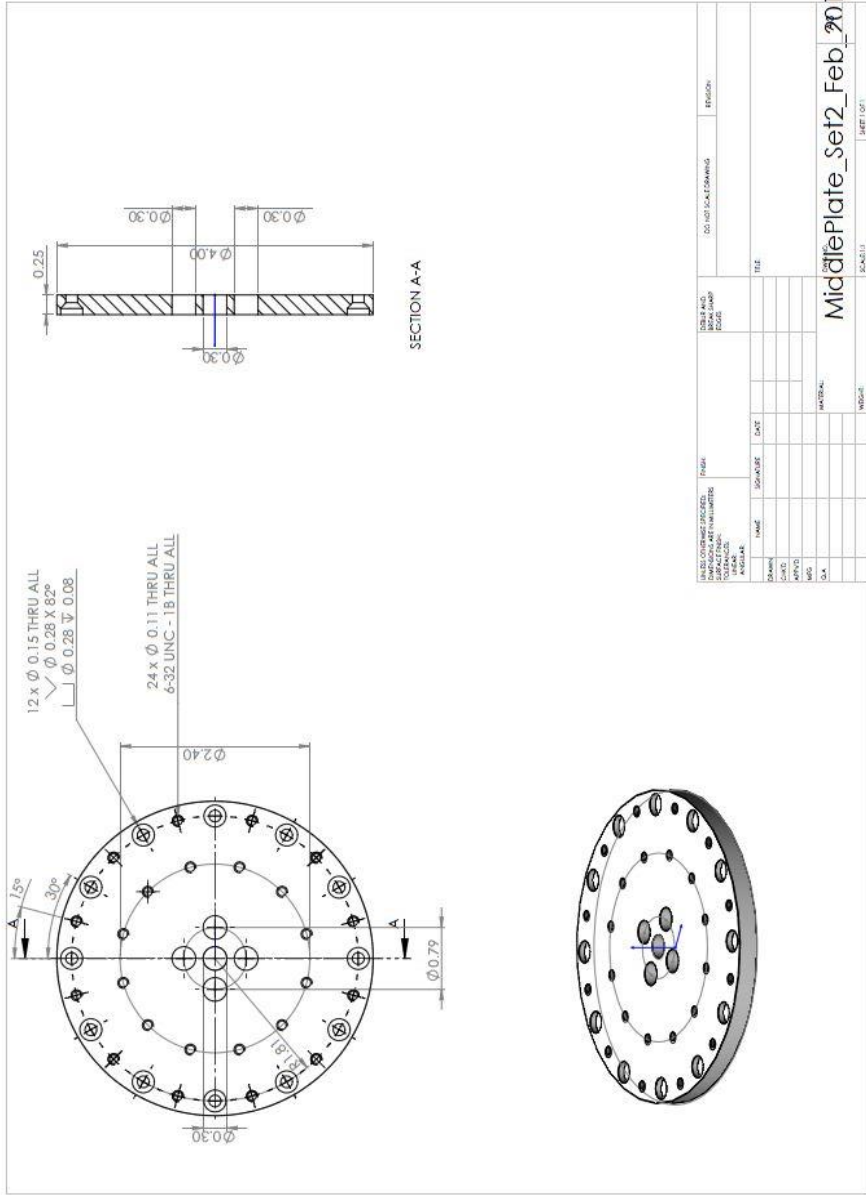




PROJECT NO.	DATE	SCALE	REVISION
DESIGN NO.	DATE	SCALE	REVISION
CHECKED	DATE	SCALE	REVISION
APPROVED	DATE	SCALE	REVISION
DRAWN	DATE	SCALE	REVISION
DATE	SCALE	REVISION	
TITLE			
MATERIAL			
REVISION			

MiddlePlate_Final_Jan_2011

SHEET 001







Appendix B

Software and Hardware used in the system

Table B-1: Software used in current work and its purpose

<i>Software used</i>	<i>Purpose</i>
LabView Version 8.5	NI VISA: Programs the syringe pump to pump or withdraw the inflating liquid into the chamber. IMAQ Vision: Programs the camera to take images at a fixed rate of 1 image/sec.
ARAMIS	Used for digital image correlation to find the displacements and strains.
ABAQUS	Used for simulation of the experimental bulge.

Table B-2: Hardware used in current work and picture of the hardware

<i>Hardware description</i>	<i>Picture</i>
<p>Pressure chamber – Liquid solution pumped into this chamber induces pressure/ load on the specimen to be tested</p>	
<p>High pressure syringe pump (NE-1010) – Used to pump/withdraw liquid in the syringe at a fixed rate (5ml/min used here).</p>	
<p>Glass-metal luer lock tip syringe and disposable plastic syringes. The syringe contains the inflating liquid solution and determines the rate of pumping that could be used.</p>	
<p>Pressure transducer (BLPR2) – Measures the pressure in the chamber with a sensitivity of $37.5 \pm 2\% \mu\text{V}/\text{V}/\text{kPa}$.</p>	

BP1 monitor – Acts as an amplifier for the signal from the pressure sensor. Provides x1, x10, x100 gain amplifications. Current work uses x100 gain for all measurements involved.



PCI-MIO-16XE DAQ board (National Instruments) – Used to collect amplified pressure sensor data from the BP1 monitor.



PCI 1409 frame grabber (National Instruments) – Two frame grabbers are used here, one for each camera. Used to interface the signals from the two camera source. The device can acquire at a rate of 60 frames/second with a double-speed progressive scan camera like Sony xc-55 used in this work. The frame grabbers are installed in two PCI slots of a Dell computer that has the custom written LabVIEW[®] code installed in it.



IMAQ-A6822 BNC connector block - This is the connector used to give user expanded functionality with National Instrument's (NI) Analog Image Acquisition cards (complete details available in NIs Knowledge Base). It is designed to connect to PCI 1409 IMAQ frame grabbers.



BNC-2090 shielded rack-mountable BNC Connector Block (NI) – Used for providing ground input to BP1 monitor that gets an analog output from BLPR2.



2 Sony xc-55 cameras with 12.5 mm focal length camera lens and pixel size 7.4 μ m. This is a progressive scan monochrome camera with a resolution of 646 \times 485 pixels.



References

- Agache, P. G., Monneur, C., Leveque, J. L., & De Rigal, J. (1980). Mechanical properties and Young's modulus of human skin in vivo. *Archives of dermatological research*, 269(3), 221-232.
- Ahlfors, J. E. W., & Billiar, K. L. (2007). Biomechanical and biochemical characteristics of a human fibroblast-produced and remodeled matrix. *Biomaterials*, 28(13), 2183-2191.
- Annaidh, A. N., Ottenio, M., Bruyère, K., Destrade, M., & Gilchrist, M. D. (2010). Mechanical Properties of Excised Human Skin. In *6th World Congress of Biomechanics (WCB 2010). August 1-6, 2010 Singapore* (pp. 1000-1003). Springer Berlin Heidelberg.
- Annaidh, A. N., Bruyère, K., Destrade, M., Gilchrist, M. D., & Otténio, M. (2012). Characterization of the anisotropic mechanical properties of excised human skin. *Journal of the Mechanical Behavior of Biomedical Materials*, 5(1), 139-148.
- Annaidh, A. N., Destrade, M., Gilchrist, M. D., & Murphy, J. G. (2012). Deficiencies in numerical models of anisotropic nonlinearly elastic materials. *Biomechanics and Modeling in Mechanobiology*, 1-11.
- Arruda, E. M., & Boyce, M. C. (1993). A three-dimensional constitutive model for the large stretch behavior of rubber elastic materials. *Journal of the Mechanics and Physics of Solids*, 41(2), 389-412.
- Azar, F. S., Metaxas, D. N., & Schnall, M. D. (2000). A finite element model of the breast for predicting mechanical deformations during biopsy procedures. In *Mathematical Methods in Biomedical Image Analysis, 2000. Proceedings. IEEE Workshop on* (pp. 38-45). IEEE.
- Billiar, K. L., & Sacks, M. S. (2000). Biaxial mechanical properties of the natural and glutaraldehyde treated aortic valve cusp—part I: experimental results. *Journal of biomechanical engineering*, 122(1), 23-30.
- Bischoff, J. E., Arruda, E. M., & Grosh, K. (2000). Finite element modeling of human skin using an isotropic, nonlinear elastic constitutive model. *Journal of biomechanics*, 33(6), 645-652.
- Bosseboeuf, A., Dupeux, M., Boutry, M., Bourouina, T., Bouchier, D., & Débarre, D. (1997). Characterization of W Films on Si and SiO₂/Si Substrates by X-Ray Diffraction, AFM and Blister Test Adhesion Measurements. *Microscopy Microanalysis Microstructures*, 8(4-5), 261-272.
- Brown, I. A. (1972). Scanning electron microscopy of human dermal fibrous tissue. *Journal of anatomy*, 113(Pt 2), 159.
- Carter, T. J. (2009). Biomechanical Modelling of the Breast for Image-Guided Surgery.

- Choi, H. S., & Vito, R. P. (1990). Two-dimensional stress-strain relationship for canine pericardium. *Journal of biomechanical engineering*, 112(2), 153.
- Chu, T. C., Ranson, W. F., & Sutton, M. A. (1985). Applications of digital-image-correlation techniques to experimental mechanics. *Experimental mechanics*, 25(3), 232-244.
- Cox, H. T. (1941). The cleavage lines of the skin. *British Journal of Surgery*, 29(114), 234-240.
- Craik, J. E., & McNeil, I. R. R. (1966). Micro-architecture of skin and its behaviour under stress.
- De Rigal, J., & Lévêque, J. L. (1985). In vivo measurement of the stratum corneum elasticity. *Bioengineering and the Skin*, 1(1), 13-23.
- Dunn, M. G., Silver, F. H., & Swann, D. A. (1985). Mechanical analysis of hypertrophic scar tissue: structural basis for apparent increased rigidity. *Journal of investigative dermatology*, 84(1), 9-13.
- Dunn, M. G., & Silver, F. H. (1983). Viscoelastic behavior of human connective tissues: relative contribution of viscous and elastic components. *Connective tissue research*, 12(1), 59-70.
- Dupuytren. G., (1834) *Traite theorique et Pratique des Blessures par Armes de Guerre*, Vol. I, p. 66, Maison, Paris.
- Dick, J. C. (1951). The tension and resistance to stretching of human skin and other membranes, with results from a series of normal and oedematous cases. *The Journal of Physiology*, 112(1-2), 102-113.
- Elden, H. R. (1971). Biophysical properties of the skin.
- Evans, S. L. (2009). On the implementation of a wrinkling, hyperelastic membrane model for skin and other materials. *Computer methods in biomechanics and biomedical engineering*, 12(3), 319-332.
- Eshel, H., & Lanir, Y. (2001). Effects of strain level and proteoglycan depletion on preconditioning and viscoelastic responses of rat dorsal skin. *Annals of Biomedical Engineering*, 29(2), 164-172.
- Finlay, B. (1969). Scanning electron microscopy of the human dermis under uni-axial strain. *Biomedical engineering*, 4(7), 322.
- Gasser, T. C., Ogden, R. W., & Holzapfel, G. A. (2006). Hyperelastic modelling of arterial layers with distributed collagen fibre orientations. *Journal of the royal society interface*, 3(6), 15-35.

- Geerligs, M. (2010). *Skin layer mechanics* (Doctoral dissertation, PhD Thesis, TU Eindhoven).
- Goodwin, C., (2011) *Anatomy and Physiology of the Skin*.
- Gray, H. (1893). *Anatomy, descriptive and surgical*. Lea Brothers & Company.
- Hendriks, F. M., Brokken, D., Van Eemeren, J. T. W. M., Oomens, C. W. J., Baaijens, F. P. T., & Horsten, J. B. A. M. (2003). A numerical-experimental method to characterize the non-linear mechanical behaviour of human skin. *Skin research and technology*, 9(3), 274-283.
- Holzapfel, G. A., Gasser, T. C., & Ogden, R. W. (2000). A new constitutive framework for arterial wall mechanics and a comparative study of material models. *Journal of elasticity and the physical science of solids*, 61(1-3), 1-48.
- Jor, J. W., Nash, M. P., Nielsen, P. M., and Hunter, P. J. (2011). “Estimating material parameters of a structurally based constitutive relation for skin mechanics.” *Biomechanics and modeling in mechanobiology*, 10(5), 767-778.
- Joseph, C. (2006) “Pocket Anatomy, A complete guide to the human body for artists and students” Barron’s, Hauppauge, New York.
- Khatam, H., Fingeret, M.C., Reece, G.P., Markey, M.K., Ravi-Chandar, K. (2013) “Measurement of skin deformation of the breast associated with position change through 3D digital image correlation”, Biomedical Engineering Society Annual Meeting, September 2013, Seattle, WA
- Khatam, H., Reece, G.P., Fingeret, M.C., Markey, M.K., Ravi-Chandar, K. (2014) “In-vivo quantification of human breast deformation associated with the position change from supine to upright”, *Medical Engineering Physics*, In Revision.
- Kim, J. H., Badel, P., Duprey, A., Favre, J. P., & Avril, S. (2011). Characterisation of failure in human aortic tissue using digital image correlation. *Computer Methods in Biomechanics and Biomedical Engineering*, 14(sup1), 73-74.
- Kvistedal, Y. A., & Nielsen, P. M. F. (2009). Estimating material parameters of human skin in vivo. *Biomechanics and modeling in mechanobiology*, 8(1), 1-8.
- Lai, W. M., Rubin, D. H., Rubin, D., & Krempl, E. (2009). *Introduction to continuum mechanics*. Butterworth-Heinemann.
- Langer, A. K. (1861) *Zur Anatomie und Physiologie der Haut. I. Uber die Spalrbarkeit der Curis. S. B. der Akad. in Wien*, Vol. 44, pp. 19-36
- Lanir, Y., & Fung, Y. C. (1974). Two-dimensional mechanical properties of rabbit skin—I. Experimental system. *Journal of biomechanics*, 7(1), 29-34.

- Lanir, Y., & Fung, Y. C. (1974). Two-dimensional mechanical properties of rabbit skin—II. Experimental results. *Journal of biomechanics*, 7(2), 171-182.
- Liu, Z., & Yeung, K. (2008). The preconditioning and stress relaxation of skin tissue. *Journal of Biomedical & Pharmaceutical Engineering*, 2(1), 22-28.
- Lim, K. H., Chew, C. M., Chen, P. C. Y., Jeyapalina, S., Ho, H. N., Rappel, J. K., & Lim, B. H. (2008). New extensometer to measure in vivo uniaxial mechanical properties of human skin. *Journal of biomechanics*, 41(5), 931-936.
- Malvern, L. (1969), *Introduction to the Mechanics of a Continuous Medium*, Prentice-Hall.
- Moore, K. L., Dalley, A. F., & Agur, A. M. (2013). *Clinically oriented anatomy*. Wolters Kluwer Health.
- Netter, F.H. (2006) “Atlas of human anatomy,” 4th edition, Saunders-Elsevier, Philadelphia, Pennsylvania, (www.netteranatomy.com).
- Nielsen, P. M., Hunter, P. J., & Smaill, B. H. (1991). Biaxial testing of membrane biomaterials: testing equipment and procedures. *Journal of biomechanical engineering*, 113(3), 295-300.
- Nielsen, P. M. F., Malcolm, D. T. K., Hunter, P. J., & Charette, P. G. (2002). Instrumentation and procedures for estimating the constitutive parameters of inhomogeneous elastic membranes. *Biomechanics and Modeling in Mechanobiology*, 1(3), 211-218.
- Oxlund, H., Manschot, J., & Viidik, A. (1988). The role of elastin in the mechanical properties of skin. *Journal of biomechanics*, 21(3), 213-218.
- Pailler-Mattei, C., Bec, S., & Zahouani, H. (2008). In vivo measurements of the elastic mechanical properties of human skin by indentation tests. *Medical engineering & physics*, 30(5), 599-606.
- Pan, B., Xie, H., Yang, L., & Wang, Z. (2009). Accurate measurement of satellite antenna surface using 3D digital image correlation technique. *Strain*, 45(2), 194-200.
- Pathmanathan, P., Gavaghan, D., Whiteley, J., Brady, M., Nash, M., Nielsen, P., & Rajagopal, V. (2004). Predicting tumour location by simulating large deformations of the breast using a 3D finite element model and nonlinear elasticity. In *Medical Image Computing and Computer-Assisted Intervention—MICCAI 2004* (pp. 217-224). Springer Berlin Heidelberg.
- Ridge, M. D., & Wright, V. (1966). The directional effects of skin. *Journal of Investigative Dermatology*, 46(4), 341-346.

- Santin, M. (2009) "Strategies in Regenerative Medicine: Integrating Biology with Materials Design." Springer Science + Business Media.
- Sasso, M., Palmieri, G., Chiappini, G., & Amodio, D. (2008). Characterization of hyperelastic rubber-like materials by biaxial and uniaxial stretching tests based on optical methods. *Polymer Testing*, 27(8), 995-1004.
- Sanders, R. (1973). Torsional elasticity of human skin in vivo. *Pflügers Archiv*, 342(3), 255-260.
- Yoneyama, S., & Murasawa, G. (2009). Digital image correlation. Experimental Mechanics. Eolss Publishers.
- Schneider, D. C., Davidson, T. M., & Nahum, A. M. (1984). In vitro biaxial stress-strain response of human skin. *Archives of Otolaryngology—Head & Neck Surgery*, 110(5), 329.
- Shoham, N., & Gefen, A. (2012). Deformations, mechanical strains and stresses across the different hierarchical scales in weight-bearing soft tissues. *Journal of Tissue Viability*, 21(2), 39-46.
- Spencer, A. (1980), Continuum Mechanics, Longman Group.
- Tanner, C. (2005). *Registration and lesion classification of contrast-enhanced magnetic resonance breast images* (Doctoral dissertation, School of Medicine, King's College London).
- Tonge, T. K., Atlan, L., Voo, L., & Nguyen, T. D. (2012). Full-field Bulge Test for Planar Anisotropic Tissues: Part I-Experimental Methods Applied to Skin Tissue. *Acta biomaterialia*.
- Treloar, L. R. G. (1944). Strains in an inflated rubber sheet, and the mechanism of bursting. *Rubber Chemistry and Technology*, 17(4), 957-967.
- Veronda, D. R., & Westmann, R. A. (1970). Mechanical characterization of skin—finite deformations. *Journal of biomechanics*, 3(1), 111-124.
- Vito, R.P. (1980). "The mechanical properties of soft tissues-i. A mechanical system for biaxial testing." *J. Biomech.* 13:947–50
- Wan Abas, W. A. B., & Barbenel, J. C. (1982). Uniaxial tension test of human skin in vivo. *Journal of biomedical engineering*, 4(1), 65-71.
- Wilkes, G. L., Brown, I. A., & Wildnauer, R. H. (1973). The biomechanical properties of skin. *CRC critical reviews in bioengineering*, 1(4), 453.

Williams, C., Kakadaris, I.A., Ravi-Chandar, K., Miller, M.J. and Patrick, C.W. (2003) "Simulation studies for predicting surgical outcomes in breast reconstructive surgery," MICCAI, LNCS 2878, 9-16.

Xu, F., & Lu, T. (2011). *Introduction to skin biothermomechanics and thermal pain*. Springer.

Zioupos, P., Barbenel, J. C., & Fisher, J. (1992). Mechanical and optical anisotropy of bovine pericardium. *Medical and Biological Engineering and Computing*, 30(1), 76-82.